NAVAL POSTGRADUATE SCHOOL

MONTEREY, CALIFORNIA

THESIS

ESTIMATING SUMMER OCEAN HEATING IN THE ARCTIC ICE PACK USING HIGH-RESOLUTION SATELLITE IMAGERY

by

Ander S. Heiles

September 2014

Thesis Advisor: Timothy P. Stanton
Second Reader: William J. Shaw

Approved for public release; distribution is unlimited

THIS PAGE INTENTIONALLY LEFT BLANK

REPORT DOCUMENTATION PAGE

Form Approved OMB No. 0704-0188

Public reporting burden for this collection of information is estimated to average 1 hour per response, including the time for reviewing instruction, searching existing data sources, gathering and maintaining the data needed, and completing and reviewing the collection of information. Send comments regarding this burden estimate or any other aspect of this collection of information, including suggestions for reducing this burden, to Washington headquarters Services, Directorate for Information Operations and Reports, 1215 Jefferson Davis Highway, Suite 1204, Arlington, VA 22202-4302, and to the Office of Management and Budget, Paperwork Reduction Project (0704-0188) Washington DC 20503.

1. AGENCY USE ONLY ***(Leave blank)***	**2. REPORT DATE** September 2014	**3. REPORT TYPE AND DATES COVERED** Master's Thesis

4. TITLE AND SUBTITLE
ESTIMATING SUMMER OCEAN HEATING IN THE ARCTIC ICE PACK USING HIGH-RESOLUTION SATELLITE IMAGERY

5. FUNDING NUMBERS
N/A

6. AUTHOR(S) Ander S. Heiles

7. PERFORMING ORGANIZATION NAME(S) AND ADDRESS(ES)
Naval Postgraduate School
Monterey, CA 93943-5000

8. PERFORMING ORGANIZATION REPORT NUMBER
N/A

9. SPONSORING /MONITORING AGENCY NAME(S) AND ADDRESS(ES)
N/A

10. SPONSORING/MONITORING AGENCY REPORT NUMBER
N/A

11. SUPPLEMENTARY NOTES The views expressed in this thesis are those of the author and do not reflect the official policy or position of the Department of Defense or the U.S. Government. IRB Protocol number ____N/A____.

12a. DISTRIBUTION / AVAILABILITY STATEMENT
Approved for public release; distribution is unlimited

12b. DISTRIBUTION CODE
A

13. ABSTRACT (maximum 200 words)

Recent observations have shown that the sea ice coverage and thickness in the Arctic Ocean is significantly decreasing. Areas of the Arctic that have traditionally been covered year-round with thick multiyear ice are being replaced by thinner first-year ice and open water. This results in increased amounts of solar radiation being absorbed and stored as heat in the upper ocean, where it is available for enhanced basal melting of sea ice. Measurements from Autonomous Ocean Flux Buoys (AOFBs) and Ice-Tethered Profilers (ITPs) were correlated to determine the ocean properties of the ice-ocean boundary layer (IOBL). High-resolution satellite imagery was processed to determine sensor positions within the image. Heat content of the IOBL was calculated by vertically integrating the departure from freezing for the time series along the AOFB drift track. This study represents one of the first attempts to quantify local open water fraction and upper ocean heat content using 1-meter pixel resolution imagery. Results indicate that the use of high-resolution satellite imagery can be used to accurately quantify local open water fraction. Approach was evaluated and validated against open water fraction, heat content, and heat flux measurements with promising results.

14. SUBJECT TERMS Arctic Ocean, Autonomous Ocean Flux Buoy, Beaufort Sea, Departure From Freezing, Heat Content, Heat Flux, High Resolution Satellite Imagery, Ice Concentration, Ice-Ocean Boundary Layer, Ice Tethered Profiler Meltpond, Meltpond Fraction, Open Water Fraction

15. NUMBER OF PAGES
113

16. PRICE CODE

17. SECURITY CLASSIFICATION OF REPORT	**18. SECURITY CLASSIFICATION OF THIS PAGE**	**19. SECURITY CLASSIFICATION OF ABSTRACT**	**20. LIMITATION OF ABSTRACT**
Unclassified	Unclassified	Unclassified	UU

NSN 7540-01-280-5500

Standard Form 298 (Rev. 2-89)
Prescribed by ANSI Std. 239-18

THIS PAGE INTENTIONALLY LEFT BLANK

Approved for public release; distribution is unlimited

ESTIMATING SUMMER OCEAN HEATING IN THE ARCTIC ICE PACK USING-HIGH RESOLUTION SATELLITE IMAGERY

Ander S. Heiles
Lieutenant, United States Navy
B.S., United States Naval Academy, 2008

Submitted in partial fulfillment of the
requirements for the degree of

MASTER OF SCIENCE IN PHYSICAL OCEANOGRAPHY

from the

NAVAL POSTGRADUATE SCHOOL
September 2014

Author: Ander S. Heiles

Approved by: Timothy P. Stanton
Thesis Advisor

William J. Shaw
Second Reader

Peter C. Chu
Chair, Department of Oceanography

THIS PAGE INTENTIONALLY LEFT BLANK

ABSTRACT

Recent observations have shown that the sea ice coverage and thickness in the Arctic Ocean is significantly decreasing. Areas of the Arctic that have traditionally been covered year-round with thick multiyear ice are being replaced by thinner first-year ice and open water. This results in increased amounts of solar radiation being absorbed and stored as heat in the upper ocean, where it is available for enhanced basal melting of sea ice. Measurements from Autonomous Ocean Flux Buoys (AOFBs) and Ice-Tethered Profilers (ITPs) were correlated to determine the ocean properties of the ice-ocean boundary layer (IOBL). High-resolution satellite imagery was processed to determine sensor positions within the image. Heat content of the IOBL was calculated by vertically integrating the departure from freezing for the time series along the AOFB drift track. This study represents one of the first attempts to quantify local open water fraction and upper ocean heat content using 1-meter pixel resolution imagery. Results indicate that the use of high-resolution satellite imagery can be used to accurately quantify local open water fraction. Approach was evaluated and validated against open water fraction, heat content, and heat flux measurements with promising results.

THIS PAGE INTENTIONALLY LEFT BLANK

TABLE OF CONTENTS

I. INTRODUCTION....1
A. MOTIVATION....1
1. Arctic Ocean Sea Ice Changes....1
2. Arctic Modeling Limitations....3
B. STUDY OBJECTIVES....5
C. NAVAL RELEVANCE....5
1. U.S. Navy Arctic Roadmap....5
2. Undersea Warfare Application....7
a. Undersea Operations in the Arctic....7
3. ONR Marginal Ice Zone (MIZ) Program....8
D. THE BEAUFORT SEA ICE MARGINAL ICE ZONE....9
1. Sea Ice-Albedo Feedback....13
2. Ocean-to-Ice Heat Flux....15
3. Surface Heat Budget of the Arctic Experiment (SHEBA)....16

II. DATA COLLECTION AND DATA PROCESSING....19
A. DATA COLLECTION....19
1. Satellite Imagery....19
2. Autonomous Ocean Flux Buoys (AOFBs)....20
3. Ice-Tethered Profilers (ITPs)....23
a. AOFB – ITP Correlation....25
B. INITIAL IMAGE PROCESSING METHOD....25
1. Selecting Initial Images for Processing....26
2. Processing Usable Images....27
a. Determining Closest Buoy Position....28
3. Determining AOFB Track and Region Breakdown....31
C. PIXEL PROCESSING METHOD....36
1. Threshold Determination....37
2. Meltpond Discrimination....41
3. Open Water Fraction Determination....45
D. BUOY DATA CORRECTION....45

III. DATA ANALYSIS AND RESULTS....47
A. CHOOSING A REFERENCE LAYER....49
B. CALCULATING HEAT CONTENT....50
C. DATA RESULTS AND DISCUSSION....52
1. Group One....53
2. Group Two....59
3. Group Three....63
4. Group Four....67

IV. DISCUSSION AND CONCLUSION....75
A. OPEN WATER FRACTION EFFECTS....80
B. SURFACE MIXED LAYER MELT HEAT CONTENT EFFECTS....80

C. HEAT FLUX EFFECTS 81
D. CONCLUSION 82
1. Recommendations for Future Work 84
2. Future Navy Impacts 85
LIST OF REFERENCES 87
INITIAL DISTRIBUTION LIST 91

LIST OF FIGURES

Figure 1. September minimum sea ice extent. The black line indicates the median extent since the advent of satellite records in the late 1970s to 2000. The yellow line indicates the previous minimum observed in 2007. The white shading shows the lowest record observed from September 2012 (from NOAA Climate 2014). 2

Figure 2. Sea ice age in May and September from 1983 to 2010. The oldest of the MYI (white shading) has decreased significantly in both May and September and has been increasingly replaced with FYI (blue shading). Insert shows the regions of ice ages used (from Maslanik et al. 2011). 3

Figure 3. Observations (solid red line) and model predictions of September sea ice cover. The model average is shown by the solid black line. Inset shows the range of model estimates from IPCC AR5, AR4 and observations (from Stroeve et al. 2012). 4

Figure 4. Navigation routes through the Arctic Ocean from the Atlantic to Pacific Oceans. This is just one of the many consequences of the increase in open water in the Arctic, and why the Navy must be focused on the observed drastic changes in the region (from U.S. Navy 2014)..... 6

Figure 5. Photograph from ICEX-2014 of CNO Admiral Jonathan W. Greenert (center right) with other distinguished visitors and crew on the *USS New Mexico (SSN-779*) (from Davies 2014)..... 8

Figure 6. Map of the marginal seas of the Western Arctic Ocean, including the Beaufort Sea, which is located to the north of Alaska (from University of Alaska, Fairbanks 2013). 9

Figure 7. Diagram illustrating the complex atmosphere-ice-ocean coupled system of a Marginal Ice Zone (MIZ) (from Lee et al. 2012). 10

Figure 8. Satellite observations of sea ice cover for 1990 (left) and 2012 (right) for April, June, and August, top to bottom. Since 1990, sea ice cover has decreased extensively, particularly in the summer months (from Lee et al. 2012). 12

Figure 9. Illustration of the albedo differences of MYI and FYI (seasonal) on total solar heat input over a season. Plot (a) is the incident solar radiation. Plot (b) is the seasonal evolution of sea ice albedo for MYI (blue) and FYI (red). Plot (c) is the daily solar heat input. Plot (d) is the time averaged solar heat input (from Perovich and Polashenski 2012). 14

Figure 10. SHEBA measurements of a) friction velocity, b) ocean-to-ice heat flux, c) heat flux at 8 meters depth, and d) heat flux at the bottom of the IOBL. While the average heat flux was , be 7.6 W m^{-2} over the entire experiment, large heat fluxes were observed during the summer melt season (from Shaw et al. 2009)..... 17

Figure 11. Example of a declassified high-resolution satellite image, approved for public release, of sea ice in the Beaufort Sea available on the USGS GFP GFL (from USGS 2014). 20

Figure 12. Overview of NPS AOFB deployments for buoys (24, 25, 26, 27) used in this study (from NPS AOFB 2014).....22
Figure 13. Schematic diagram of the NPS AOFB (from NPS AOFB 2014). 23
Figure 14. WHOI ITP schematic (from Krishfield et al. 2006). 24
Figure 15. Example azimuth, zenith, and time of day calculations from a known satellite image center position and time of day. In this example, the minimum value indicates the time of day of the image is 2330 on 02 June 2012.....28
Figure 16. Example of a "miss" image. In this image, the closest AOFB position to the image capture time does not fall within the image boundaries. No further processing is done. 29
Figure 17. Example of a "hit" image. In this image, the closest AOFB position to the image capture time falls within the image boundaries. This image is retained for further processing. 30
Figure 18. Zoomed in view of an AOFB position for the "hit" image from Figure 17. ...31
Figure 19. Example of a 24 hour AOFB trajectory. The red represents the record position of the closest AOFB to the time of the image. Green is the previous 12 hour position records. Blue is the ensuing 12 hour positions records.....32
Figure 20. 500m x 500m sub-regions established around AOFB positions at a 500m interval. 33
Figure 21. Zoomed view of a 500m by 500m sub-region from Image Two, Sub-region Four (Figure 20) Note the open water, ice floe, and meltpond features that are clearly visible. 34
Figure 22. Example of an image rejected for further analysis due to heavy cloud cover. The closest AOFB position is plotted in red. 35
Figure 23. Pixel intensity histogram for Image Two, Sub-region Four. Note the presence of a bimodal distribution pattern (the "u" shaped pattern on the left portion of the histogram). 38
Figure 24. The original grayscale matrix for Image Two, Sub-region Four is seen on the left. On the right is the converted binary black and white matrix plotted with a threshold value of 25.....38
Figure 25. The original grayscale matrix for Image Two, Sub-region Four is seen on the left. On the right is the converted binary black and white matrix plotted with a threshold value of 125.....39
Figure 26. The original grayscale matrix for Image Two, Sub-region Four is seen on the left. On the right is the converted binary black and white matrix plotted with a threshold value of 60.....39
Figure 27. The original grayscale matrix for Image 22, Sub-region Four is seen on the left. On the right is the converted binary black and white matrix plotted with a determined threshold value of 190. This value is much larger than would have been selected using the discussed methodology; however, it was chosen to capture the large open water features of the image. 40
Figure 28. The original grayscale matrix for Image Two, Sub-region Four is seen on the left. On the right is the converted binary black and white matrix

plotted with an automatically determined threshold value of zero. The total white color indicates the thresholding program determined the entire image is comprised of sea ice. 40
Figure 29. Image Two, Sub-region Four converted with an applied threshold of 60. Overlaid in green are the default meltponds. There are many large meltponds which based on a visual of the original satellite image are actually areas of open water which need to be discriminated. These areas are highlighted by the red circles. 42
Figure 30. Histogram for the major and minor axis lengths for Image Two, Sub-region Four. Areas of open water incorrectly identified as meltponds are filtered out based on the values of their major and minor axes. 43
Figure 31. Image Two, Sub-region Four meltponds with an applied threshold of 60, major axis criteria of 120, and minor axis criteria of 60 applied. The regions originally identified in Figure 29 as meltponds are correctly identified as open water (red circles). Additionally, some of the larger meltponds (blue circles) are also identified as open water. 44
Figure 32. Example of raw AOFB and ITP temperature and conductivity time series. The temperature measurements match well, but the calculated conductivity measurements differ slightly. Also, the "up-profile" and "down-profile" nature of the CTD data from the ITP which needed to be corrected can be seen. 46
Figure 33. Schematic illustrating the conceptual approach used in this thesis. Top Image: heat enters the IOBL via open water leads (red circle). Wind forcing induces ice movement over an assumed static ocean, storing the heat under the ice in the path ahead of the ice-supported sensors (shaded red area). Bottom Image: stored heat is transported vertically due to ice-induced shear turbulence. This heat is then available to cause basal ice melt. 48
Figure 34. Example of the vertical profiles of temperature, salinity, and density. The vertical gradient associated with the Arctic halocline is indicated by the red arrows. The lower reference layer chosen to be used for analysis throughout this thesis is illustrated by the thick blue line....50
Figure 35. Vertical heat content profile from the surface to 200 meters in the Arctic Ocean. A strong halocline and warm Atlantic water can be seen, both of which are decoupled from the surface mixed layer. 52
Figure 36. Zoomed in view of Image One in Group One. The sub-region the AOFB was located in at the time of image capture is shaded in yellow. Blue sub-regions show the ice pack trajectory +/-12 hours from the image capture time, as indicated by the red arrows....54
Figure 37. Zoomed in view of Image Two in Group One. The sub-region the AOFB was located in at the time of image capture is shaded in yellow. Blue sub-regions show the ice pack trajectory +/-12 hours from the image capture time, as indicated by the red arrows....55
Figure 38. Image One (Group One) open water fraction, departure from freezing, and vertically integrated heat content time series. 56

Figure 39. Image Two (Group One) open water fraction, departure from freezing, and vertically integrated heat content time series. 57
Figure 40. Vertical profiles of temperature, salinity, density and calculated departure from freezing values for Group One. Yeardays corresponding to available satellite imagery are marked by the blue arrows along the x-axis. 58
Figure 41. Vertical profile of melt heat content for Group One. Yeardays corresponding to available satellite imagery are marked by the blue arrows along the x-axis. 58
Figure 42. Zoomed in view of Image 22 in Group Two. The sub-region the AOFB was located in at the time of image capture is shaded in yellow. Blue sub-regions show the ice pack trajectory +/-12 hours from the image capture time, as indicated by the red arrows. 60
Figure 43. Image 22 (Group Two) open water fraction, departure from freezing, and vertically integrated heat content time series. 61
Figure 44. Vertical profiles of temperature, salinity, density and calculated departure from freezing values for Group Two. Yeardays corresponding to available satellite imagery are marked by the blue arrows along the x-axis. 62
Figure 45. Vertical profile of melt heat content for Group Two. Yeardays corresponding to available satellite imagery are marked by the blue arrows along the x-axis. 63
Figure 46. Zoomed in view of Image 26 in Group Three. The sub-region the AOFB was located in at the time of image capture is shaded in yellow. Blue sub-regions show the ice pack trajectory +/-12 hours from the image capture time, as indicated by the red arrows. 64
Figure 47. Image 26 (Group Three) open water fraction, departure from freezing, and heat content. 65
Figure 48. Vertical profiles of temperature, salinity, density and calculated departure from freezing values for Group Three. Yeardays corresponding to available satellite imagery are marked by the blue arrows along the x-axis. 66
Figure 49. Vertical profile of melt heat content for Group Three. Yeardays corresponding to available satellite imagery are marked by the blue arrows along the x-axis. 67
Figure 50. Zoomed in view of Image 13 in Group Four. The sub-region the AOFB was located in at the time of image capture is shaded in yellow. Blue sub-regions show the ice pack trajectory +/-12 hours from the image capture time, as indicated by the red arrows. 68
Figure 51. Zoomed in view of Image 15 in Group Four. The sub-region the AOFB was located in at the time of image capture is shaded in yellow. Blue sub-regions show the ice pack trajectory +/-12 hours from the image capture time, as indicated by the red arrows. 69
Figure 52. Zoomed in view of Image 17 in Group Four. The sub-region the AOFB was located in at the time of image capture is shaded in yellow. Blue sub-regions show the ice pack trajectory +/-12 hours from the image capture time, as indicated by the red arrows. 70

Figure 53. Image 13 (Group Four) open water fraction, departure from freezing, and heat content time series. 71
Figure 54. Image 15 (Group Four) open water fraction, departure from freezing, and heat content time series. 72
Figure 55. Image 17 (Group Four) open water fraction, departure from freezing, and vertically integrated heat content time series. 72
Figure 56. Vertical profiles of temperature, salinity, density and calculated departure from freezing values for Group Four. Yeardays corresponding to available satellite imagery are marked by the blue arrows along the x-axis. ..73
Figure 57. Vertical profile of melt heat content for Group Four. Yeardays corresponding to available satellite imagery are marked by the blue arrows along the x-axis. 74
Figure 58. Heat transfer time series for Image Group One. 76
Figure 59. Heat transfer time series for Image Group Two. 77
Figure 60. Heat transfer time series for Image Group Three. 78
Figure 61. Heat transfer time series for Image Group Four. 79
Figure 62. Photographs of AOFB 29 deployed in the Arctic in August 2014. Left Image: small domed solar sensor on the left-most arm of the meteorology tree collects shortwave (visible) surface solar intensity time series which can be used to understand the effects of varying solar intensity in the open water fraction/heat content relationship. Right Image: close up image of the solar sensor used to collect shortwave solar information (images courtesy Mr. Jim Stockel 2014). 85

THIS PAGE INTENTIONALLY LEFT BLANK

LIST OF TABLES

Table 1. AOFB-ITP mission correlation summary. 25
Table 2. List of variables extracted from image metadata files. 26
Table 3. Summary of AOFB "hit" information. Yellow shading indicates an AOFB was located within the available image. 26
Table 4. Summary of the image quality screen. Yellow shading indicates the seven images used in this study for further analysis. 36
Table 5. Results group summary. Results groups were determined by correlating satellite imagery, AOFB, and ITP data sets. Groups One through Three are data and observations from the Beaufort Sea; Group Four is data and observations from the Transpolar Drift 53

THIS PAGE INTENTIONALLY LEFT BLANK

LIST OF ACRONYMS AND ABBREVIATIONS

AOFB	Autonomous Ocean Flux Buoy
AR4	Fourth Assessment Report
AR5	Fifth Assessment Report
ASL	Arctic Submarine Lab
CNO	Chief of Naval Operations
EEZ	Exclusive Economic Zone
FYI	first-year ice
GFL	Global Fiducials Library
GFP	Global Fiducials Program
GMT	Greenwich Mean Time
ICEX	Ice Exercise
IMU	Inertial Measurement Unit
IOBL	Ice-Ocean Boundary layer
IPCC	Intergovernmental Panel on Climate Change
ITP	Ice-Tethered Profiler
MIZ	Marginal Ice Zone
MIZ - DRI	Marginal Ice Zone – Departmental Research Initiative
MIZEX	Marginal Ice Zone Exercise
MYI	multi-year ice
NOAA	National Oceanic and Atmospheric Administration
NSF	National Science Foundation
NSIDC	National Snow and Ice Data Center
NPS	Naval Postgraduate School
ONR	Office of Naval Research
SAR	Synthetic Aperture Radar
SHEBA	Surface Heat Budget of the Arctic
USGS	United States Geological Survey
UUV	unmanned undersea vehicle
WHOI	Woods Hole Oceanographic Institute
UTM	Universal Transverse Mercator

THIS PAGE INTENTIONALLY LEFT BLANK

ACKNOWLEDGMENTS

I would like to acknowledge all those at in the Naval Postgraduate School Oceanography Department who helped and guided me through both this thesis and my course of studies. First and foremost, thank you to my thesis advisor, Prof. Tim Stanton, for giving me the opportunity to pursue my goal of relevant research in the Arctic. I would also like to thank Prof. Bill Shaw for his input and assistance while guiding me through some of the tough scientific questions I faced. A BIG thank you is owed to Mr. Jim Stockel and Mr. Mike Cook for their seemingly endless hours of MATLAB guidance. A special thank you also goes to CDR Shawn Gallaher for his patience and guidance throughout the thesis process.

I would also like to thank those in the Undersea Warfare Department who helped contribute to my research efforts and studies. I also thank RADM Jerry Ellis and RDML Rick Williams for their mentorship and support in pursuit of my master's degree at NPS. Additionally, I am grateful to Professor Daphne Kapolka for her endless help in the classroom and with my thesis. Finally, I would like to thank CDR William Sommer for his professional guidance.

Finally, I would like to thank my loving wife, Shawna, and my amazing son, Logan, who certainly sacrificed the most while I was working on campus. Last but certainly not least, I would like to thank my mother and father, Nancy and Sigfried Heiles, as well as my sister, Sonja Heiles, for being there for me whenever I called.

THIS PAGE INTENTIONALLY LEFT BLANK

I. INTRODUCTION

A. MOTIVATION

Covering an area of over 5.4 million square miles (nearly 1.5 times the size of the United States), the Arctic Ocean is the smallest of the world's oceans and is characterized by the unique presence of seasonal and perennial sea ice over the ocean (U.S. Navy 2014). Historically, the region was unnavigable due to year-round sea ice cover, which prevented transit by commercial ships. The world was amazed in 2009, when two German cargo ships made the journey through the infamous Northeast Passage from Korea to the Netherlands (*Reuters* 2014). Only four years later, during the summer of 2013, 71 commercial vessels successfully navigated the Northern Sea Route from the Bering Strait to the Barents Sea (Pettersen 2013). Due to the harsh operating conditions associated with the environment which impede year-round access, little is understood about the atmosphere, ice, and ocean properties that govern the physical processes in the region. However, it has long been accepted that the Arctic is critical in moderating global climate, and is thus most likely to show the first signs of global climate change (Smith and Grebmeier 1995). The observed rapid changes throughout the Arctic region have prompted renewed interest in scientific and naval research with the goal understanding the physical processes driving these changes.

1. Arctic Ocean Sea Ice Changes

According to the Arctic Report Card 2012 (National Oceanic and Atmospheric Administration (NOAA) Climate 2014), since the advent of satellite-based passive microwave monitoring of sea ice extent in the Arctic Ocean in 1979, it has been observed that the summer sea ice cover extent has been declining (Figure 1). In 2011, Stroeve et al. found that the decreasing trend was approximately 12.4% per decade, accelerated by some of the lowest extends on record from 2003-2010. It was generally accepted that the 2007 record low-minimum summer ice extent was the result of extreme atmospheric forcing, and the Arctic would begin to recover afterwards (National Snow and Ice Data Center [NSIDC] 2014). However, the NSIDC (2014) also observed that in September 2012, when a new minimum 18% below the 2007 minimum extent was reached,

atmospheric conditions were not a contributing factor. Not only are observations showing a decrease in the summer sea ice extent, but the type of ice present in the Arctic is changing as well. Maslanik et al. (2011) used passive microwave data to show that the amount of thick, multi-year ice (MYI) in the Arctic decreased from 75% to 45% from the 1980s to 2011, as seen in Figure 2. They concluded that the MYI was being replaced by much thinner first-year ice (FYI) and open water. Changes in the summer sea ice cover and ice type can result in significant changes to the physical processes and interactions throughout the Arctic region.

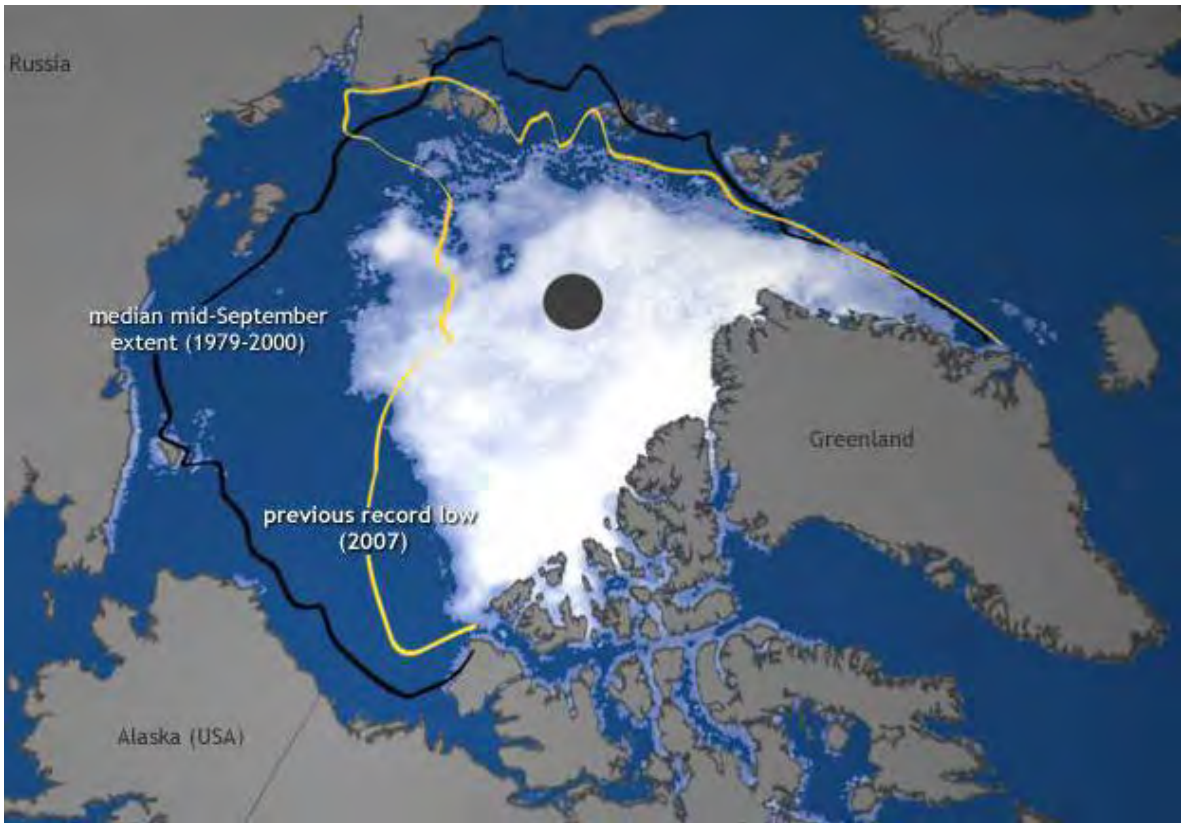

Figure 1. September minimum sea ice extent. The black line indicates the median extent since the advent of satellite records in the late 1970s to 2000. The yellow line indicates the previous minimum observed in 2007. The white shading shows the lowest record observed from September 2012 (from NOAA Climate 2014).

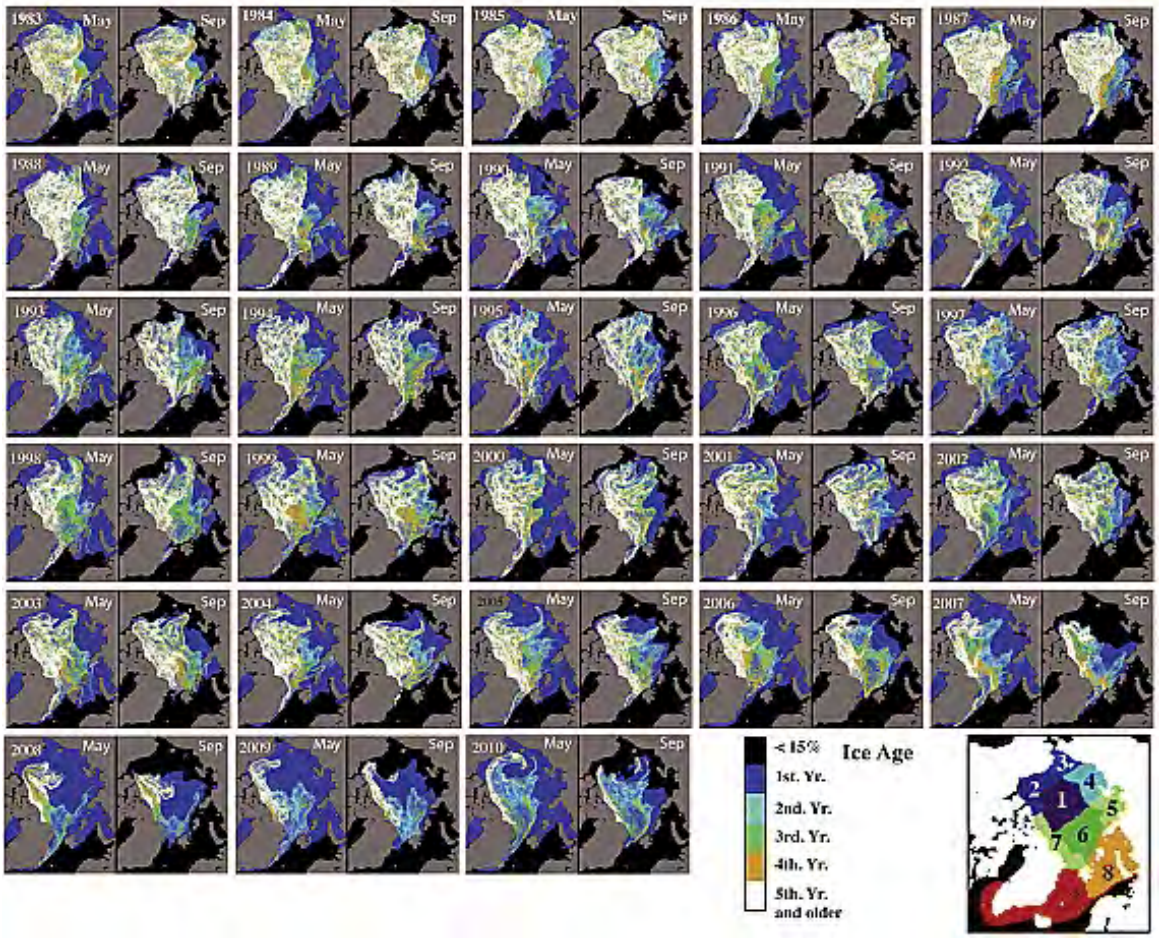

Figure 2. Sea ice age in May and September from 1983 to 2010. The oldest of the MYI (white shading) has decreased significantly in both May and September and has been increasingly replaced with FYI (blue shading). Insert shows the regions of ice ages used (from Maslanik et al. 2011).

2. Arctic Modeling Limitations

In 2007, the Intergovernmental Panel on Climate Change (IPCC) *Fourth Assessment Report* (AR4) first concluded that the September sea ice cover was decreasing at rates much faster than coupled global models could predict (Stroeve et al. 2012). In response to new evidence of global climate change from various observations, the IPCC conducted a *Fifth Assessment Report* (AR5) and released its "Summary For Policy Maker's" in 2013 (IPCC 2013). The AR5 suggested that the retreat of summer sea ice extent will continue, and models suggest it is likely the Arctic Ocean will be nearly

ice-free during the Arctic summer before the end of the century, as seen in Figure 3. While the models show a conservative decline in sea ice extent, observations (the thick red line) show significantly higher magnitude and rates of change. As DiMaggio (2014) discusses, global climate models often do not include unresolved and under-represented physical processes in the region, nor do they account for the changes in ice thickness. Whether the tipping point for the recovery of sea ice extent and MYI has been reached is yet to be conclusively proven. Simply put, the complex and dynamic physical properties and feedbacks of the region are not well understood, making modelling efforts difficult.

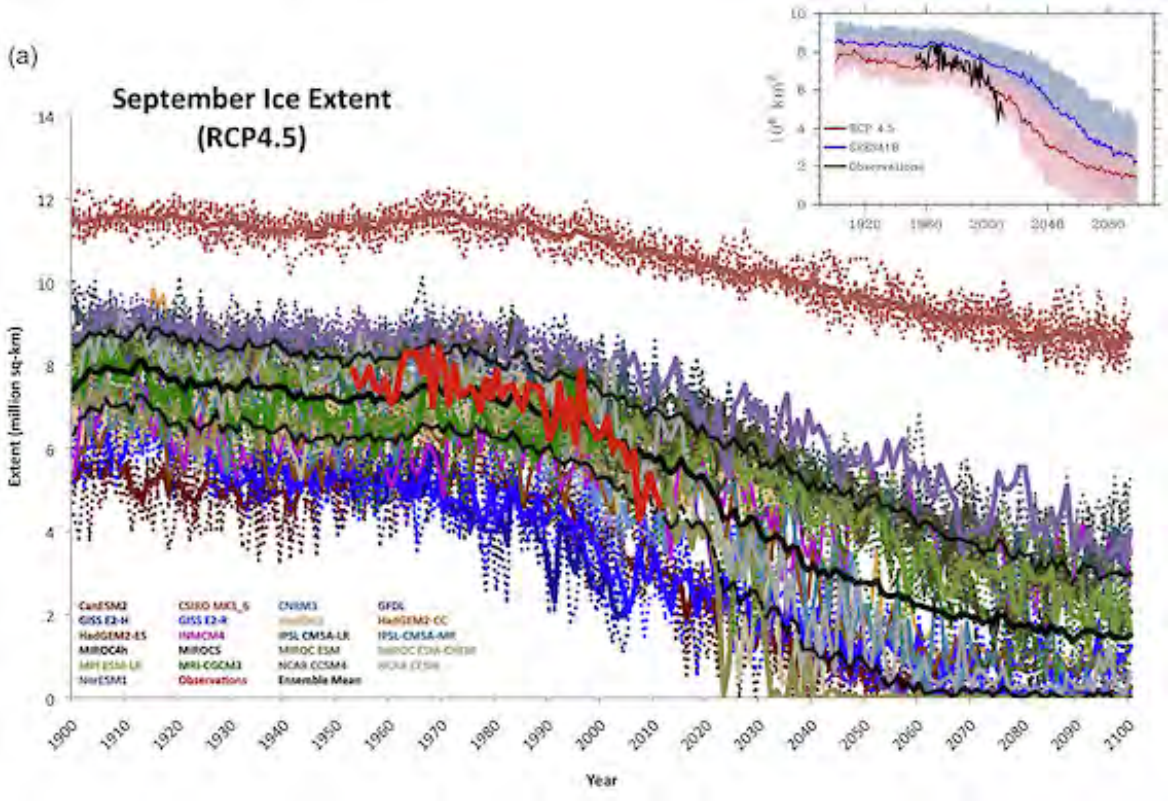

Figure 3. Observations (solid red line) and model predictions of September sea ice cover. The model average is shown by the solid black line. Inset shows the range of model estimates from IPCC AR5, AR4 and observations (from Stroeve et al. 2012).

B. STUDY OBJECTIVES

Improving the sea ice cover and thickness prediction capability for the U.S. Navy during these drastic ice regime changes in the Arctic has become a critical requirement (Lee et al. 2012). As Suh (2011) discussed, Arctic sea ice is affected from both surface melting due to atmospheric conditions, as well as basal melting due to oceanic conditions. In the Beaufort Sea, the development of an expanding widespread seasonal Marginal Ice Zone (MIZ) earlier in the summer season is changing the governing processes of the regional atmosphere-ice-ocean system (Lee et al. 2012). In order to accurately predict and understand changes to ice cover and thickness, the surface energy fluxes of the ocean must be well understood (Stanton et al. 2012, Shaw et al. 2009).

The objectives of this thesis are to 1) use high-resolution satellite imagery to quantify local open water fraction of the ice pack around previously deployed buoys in the Arctic; and 2) examine the relationship between upper ocean heat content to local open water fraction derived from high-resolution satellite imagery. While this study will focus on the observations collected in the Beaufort Sea, the approach used will also be applied to the central Arctic.

C. NAVAL RELEVANCE

1. U.S. Navy Arctic Roadmap

In 2009, the U.S. Navy renewed its interest in the Arctic when the Chief of Naval Operations (CNO) declared the Arctic as a critical focus region for the Navy in the first published Arctic Roadmap (U.S. Navy 2014). In 2014, the CNO signed an updated Arctic Roadmap which addressed current operational limitations and identified the way forward (Metzger 2014). The U.S. is an Arctic nation that has resource rich Exclusive Economic Zone (EEZ) off the coast of Alaska (U.S. Navy 2014). As perennial sea ice extent continues to decline, the area of navigable waters of the Arctic Ocean will likely continue to increase, allowing for an increase in military, commercial, and tourist traffic (Figure 4). Promoting and maintaining a stable and secure Arctic region is a national objective of the U.S. and a strategic objective for the Navy (U.S. Navy 2014). Besides providing the framework for military contingencies and planning operations, the Arctic

Roadmap also outlines and allocates resources for scientific expeditions aimed at improving our understanding of the physical properties and processes of the coupled atmosphere-ice-ocean system.

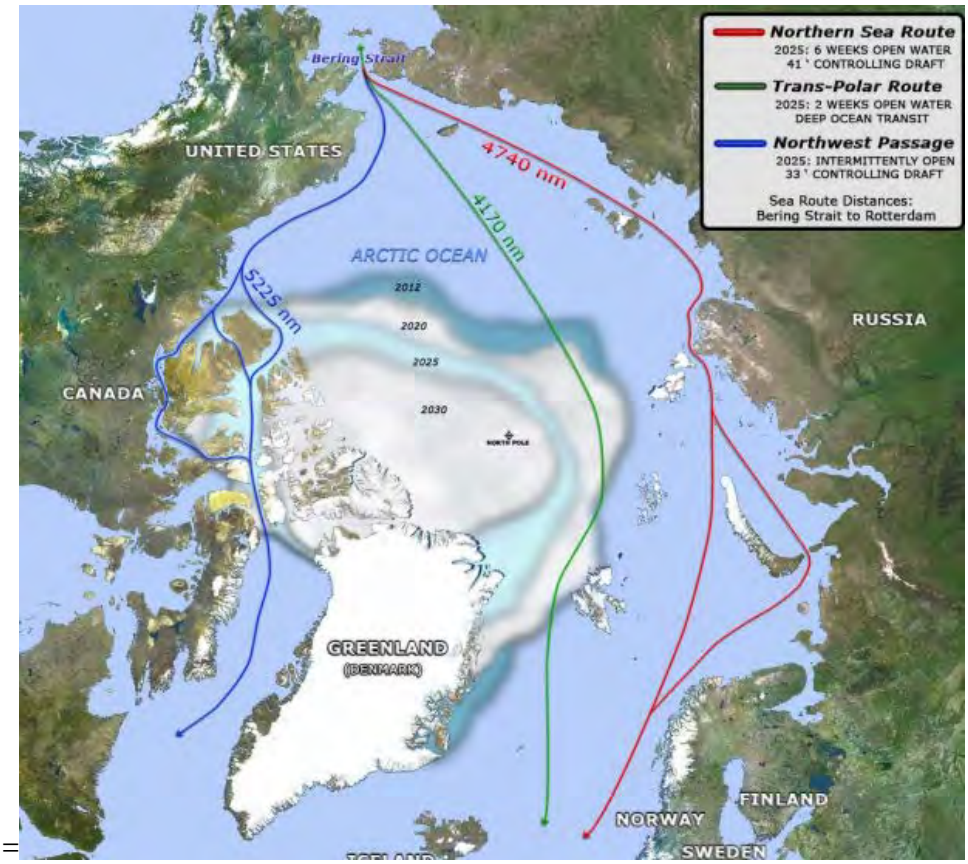

Figure 4. Navigation routes through the Arctic Ocean from the Atlantic to Pacific Oceans. This is just one of the many consequences of the increase in open water in the Arctic, and why the Navy must be focused on the observed drastic changes in the region (from U.S. Navy 2014).

The U.S. Navy Arctic Roadmap acknowledges that U.S. national security is tied to changing climate and dictates the Navy's role and responsibilities. Sections 2.2 and 2.3 of Appendix 3 in the Arctic Roadmap specifically assert the science and observation milestones the Navy must work to achieve. The work in this thesis meets the actions defined in in Appendix 3, Section 2.2.6 to "Increase [the] Office of Naval Research (ONR) Arctic efforts…to improve the Navy's ability to understand and predict the Arctic

physical environment at a variety of time and space scales." By improving our understanding of the changes in the Beaufort Sea seasonal MIZ, the physical properties of the region can be used to update global and regional sea ice models.

2. Undersea Warfare Application

The research done for this thesis directly supports undersea warfare operations. Submarines and other undersea platforms are currently the primary means for the U.S. to show a presence in the region (U.S. Navy 2014). The ability to operate efficiently and safely in the harsh Arctic environment requires that a commander have as much information as possible prior to deployment. Arguably, the greatest danger to submarines operating in the area is not from below, but rather the changing ice canopy above. It is critical that the forecast models that the commander receives be as detailed as possible, which underscores the need for accurate and current observations. The research done in this thesis will help improve the information that is provided to the Fleet. Additionally, the satellite imagery processing techniques can be integrated to aid submarine pilots in determining safe areas to conduct surfacing operations.

a. Undersea Operations in the Arctic

Naval undersea operations in the Arctic go back to 1941, when the Arctic Submarine Lab (ASL) was established to counter the threat of Soviet submarine dominance under the polar ice (ASL 2014). According to the ASL historical timeline, a historical milestone was reached by the Navy in 1958, when the *USS Nautilus (SSN-571)* became the first submarine to transit under the Arctic ice cap submerged. This was followed by the first breaching of the North Pole by the *USS Skate (SSN-578*) in 1962 (ASL 2014). Since then, over 120 Arctic exercises and operations have been conducted by the Navy (U.S. Navy 2014). Most recently, in March of 2014, the *USS New Mexico (SSN-779)* (Figure 5) and the *USS Hampton (SSN-767)* participated in Ice Exercise (ICEX) 2014 (Metzger 2014). According to the U.S. Navy press release, ICEX 2014 was designed to test and develop cold-weather operational procedures and collect vital in-situ data for scientific study.

Figure 5. Photograph from ICEX-2014 of CNO Admiral Jonathan W. Greenert (center right) with other distinguished visitors and crew on the *USS New Mexico (SSN-779*) (from Davies 2014).

3. ONR Marginal Ice Zone (MIZ) Program

In direct support of the Navy's efforts to improve understanding of the physical conditions and dynamics of the Arctic Ocean is the ONR MIZ Department Research Initiative (DRI). According to Lee et al. (2012), the focal area for the ONR MIZ DRI is the Beaufort Sea, the location within the U.S. EEZ where the observed changes in sea ice cover in the Arctic are most apparent. The objectives of the five-year experiment (2012–2017) include 1) collect data over multiple seasons and conditions; 2) identify the physical processes that cause the development of the seasonal MIZ in the Beaufort Sea; 3) understand how anticipated sea ice levels will affect the future development of the seasonal Beaufort Sea MIZ; and 4) evaluate and improve current Beaufort Sea MIZ modelling efforts to increase sea ice forecasting capability for the U.S. Navy. A cooperative effort between the Navy and over a dozen research organizations, such as the Naval Postgraduate School (NPS) (Lee et al. 2012), the work done for this study directly contribute to the stated goals of the ONR MIZ DRI.

D. THE BEAUFORT SEA ICE MARGINAL ICE ZONE

Located just north of Alaska in the U.S. Arctic EEZ (Lee et al. 2012), the Beaufort Sea is one of the numerous marginal seas located around the periphery of the Arctic Ocean, as seen in Figure 6. The Beaufort Sea has historically been considered an indicator of the overall "health" of the Arctic ice pack (Lee et al. 2012). A study conducted by Maslanik et al. (2011) found that from 1981–2005, 93% of the ice in the Beaufort Sea was MYI, indicating that the thick ice pack in the region was capable of surviving multiple summer melt and winter freeze seasonal cycles with little variability. Krishfield et al. (2014) reported that MYI generated in the Beaufort Sea is transported throughout the Arctic Basin by the Beaufort Gyre, thus the MYI generated and stored within this sea contributes to the entire the Arctic ice pack.

Figure 6. Map of the marginal seas of the Western Arctic Ocean, including the Beaufort Sea, which is located to the north of Alaska (from University of Alaska, Fairbanks 2013).

For the purposes of this thesis, the MIZ (Figure 7) will be considered the region between the open ocean and the compact ice pack, where thermodynamic and wave influences arising from open water between ice floes is strong. Conventionally, a MIZ is a narrow region (25km to 100km) of atmosphere-ice-ocean interaction that is significantly altered by the presence of sea ice (McPhee 1983). From Lee et al. (2012), seasonal MIZ's that develop early in the summer and cover large areas are common in the western marginal seas of the Arctic Ocean, such as the Bering Sea and Chukchi Sea

(Figure 6). They suggest that while a seasonal MIZ developing the Beaufort Sea is common, observations show it is evolving much earlier in the summer and is covering an increased areal extent.

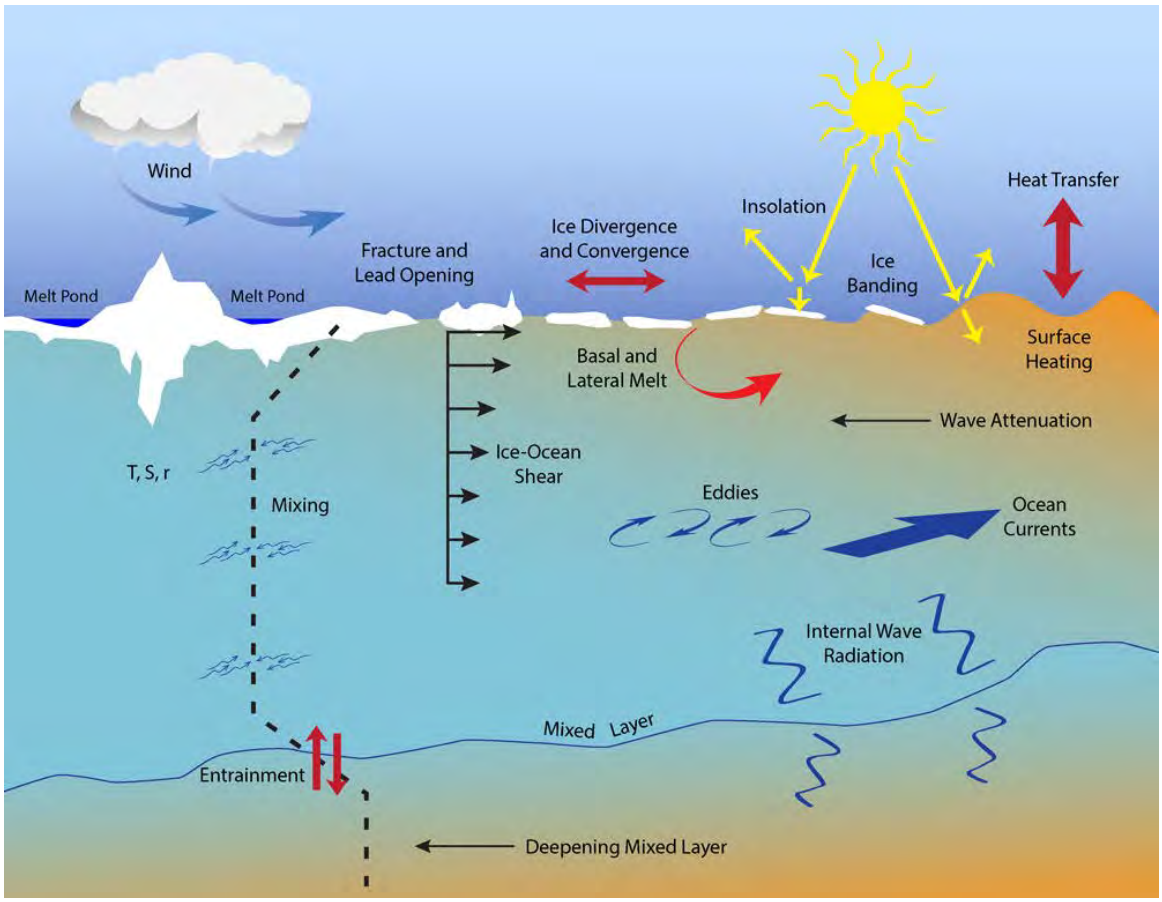

Figure 7. Diagram illustrating the complex atmosphere-ice-ocean coupled system of a Marginal Ice Zone (MIZ) (from Lee et al. 2012).

Satellite-based observations, published in Lee et al. (2012), show that the Beaufort Sea is experiencing not only the greatest loss in sea ice, but at the fastest rates of increasing ice loss as well (Figure 8). They also show that before the observed changes, sea ice cover did not retreat far from the Alaskan coast, even during the summer. However, during the September 2012 record minimum, the MYI cover retreated deep into the Beaufort Sea, leaving thin FYI and open water in its wake (Lee et al. 2012). Maslanik (2011) found that MYI declined by an astonishing 73% from 2006-2010; a

strong indicator of the shift of Arctic sea ice cover from a permanent cap to a seasonal presence (Stroeve et al. 2011). The evidence suggests that the observations are a direct result of the expansion of the seasonal MIZ in the Beaufort Sea. Perhaps even more alarming, Maslanik et al. (2011) also observed that the Beaufort Sea was the location of the remaining MYI left in the Arctic following the 2007 minimum, which is now disappearing. Decreases in the presence of MYI and the shift towards an increase in the amount of FYI and open water can significantly alter thermodynamic and mechanical dynamics of the atmosphere-ice-ocean coupled system both locally and across the entire Arctic Basin (Lee et al. 2012). Sea ice is a critical parameter in a MIZ that moderates the atmosphere-ice-ocean system in the ice-ocean-boundary layer (IOBL), the layer of water below the ice and above the permanent Arctic pycnocline (McPhee 1983).

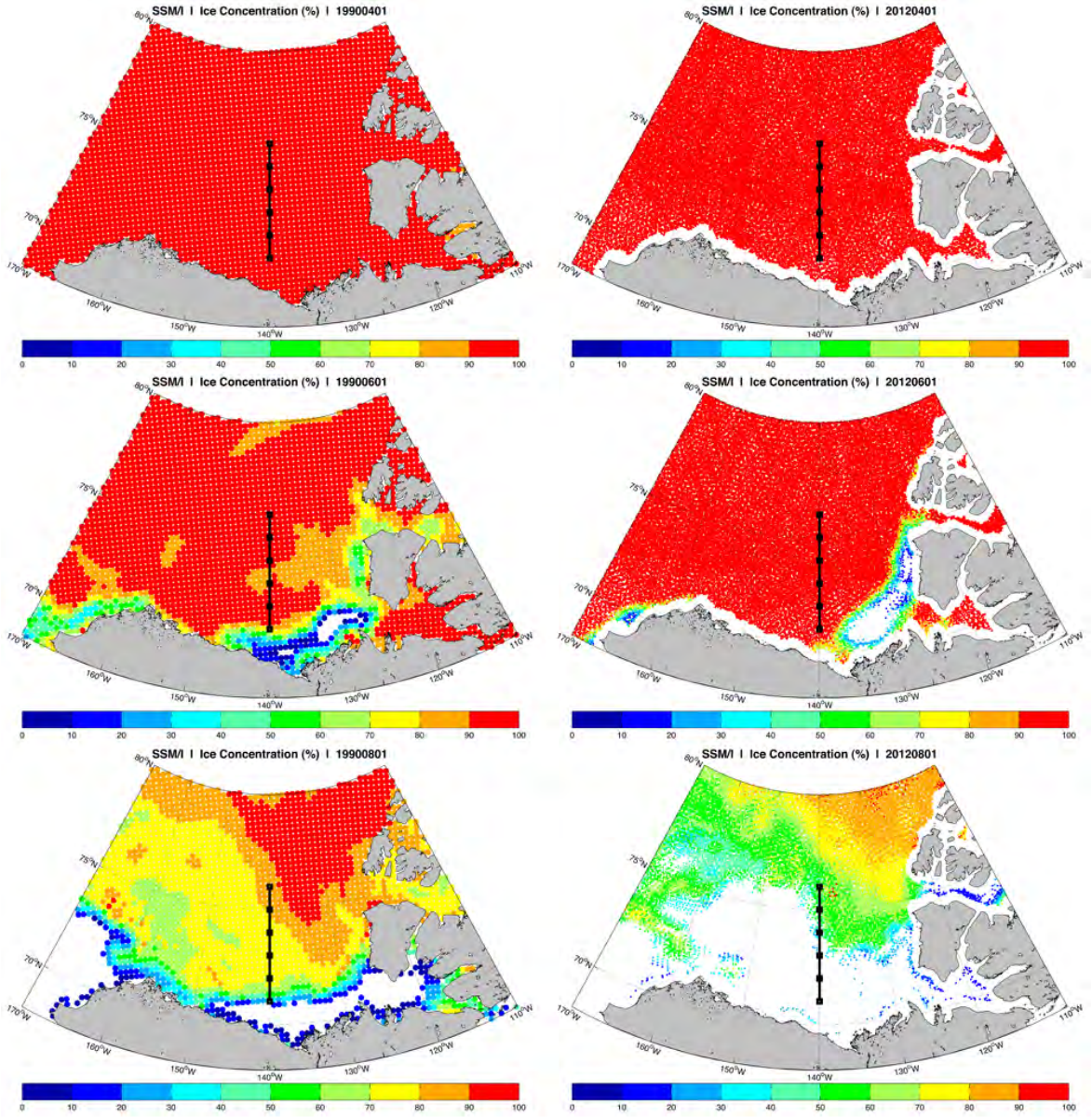

Figure 8. Satellite observations of sea ice cover for 1990 (left) and 2012 (right) for April, June, and August, top to bottom. Since 1990, sea ice cover has decreased extensively, particularly in the summer months (from Lee et al. 2012).

1. Sea Ice-Albedo Feedback

Albedo is a measure of the reflection of incoming solar radiation back to the atmosphere (Perovich and Polashenski 2012). As outlined by Col (2010), solar radiation enters the IOBL, either absorbed by open water or transmitted through deep meltponds and ice, where it is stored as heat. For a given area, if the regional albedo is low, more heat from solar input will be stored in the IOBL (Col 2010). He summarizes that the additional heat can become available through ice-generated turbulence to enhance the basal melt of ice, in addition to the surface melt from solar radiation. The result is an increase in thin ice and open water available to accept solar input, completing (and enhancing) this positive feedback loop, a key parameter that links sea ice to regional and global climatology (Perovich 2005).

Perovich (2005) divides incoming solar radiation into three categories: 1) albedo $\left(\overline{\alpha}\right)$, 2) absorption $\left(\overline{B}\right)$, and 3) transmission $\left(\overline{T}\right)$. He finds that on the aggregate scale, these factors must equal one, as seen in Equation (1). Perovich and Polashenski (2012) show that MYI has a high albedo and low absorption and transmission; therefore small amounts of solar energy will enter the IOBL and stored as heat. Consequently, they found FYI has a low albedo, which results in higher absorption and transmittance. The nominal differences in albedo magnitude between MYI and FYI over a seasonal freeze and melt cycle, and the resulting differences in solar and heat input is seen in Figure 9.

$$\overline{\alpha} + \overline{B} + \overline{T} = 1 \tag{1}$$

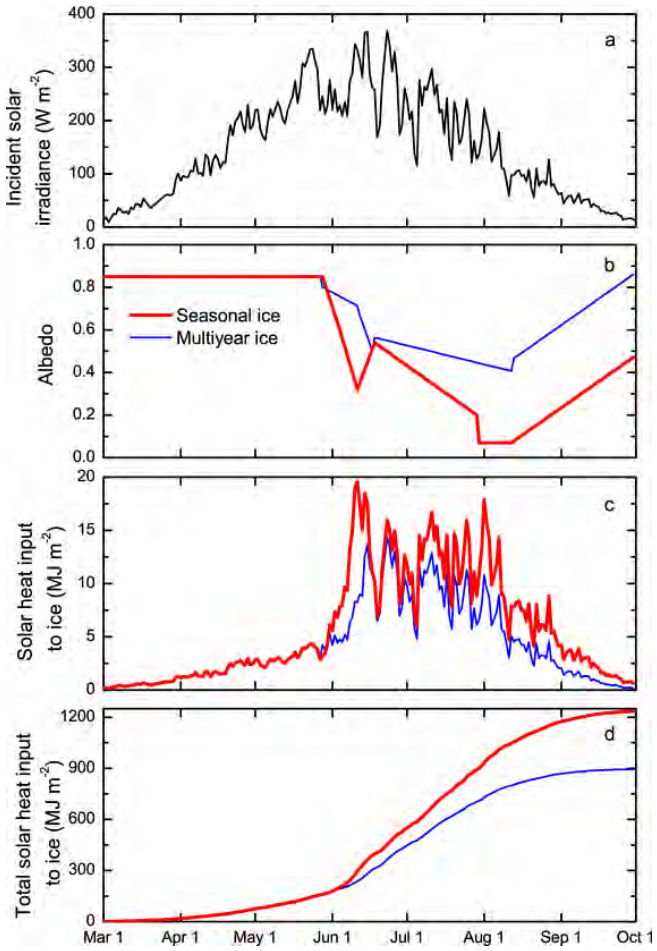

Figure 9. Illustration of the albedo differences of MYI and FYI (seasonal) on total solar heat input over a season. Plot (a) is the incident solar radiation. Plot (b) is the seasonal evolution of sea ice albedo for MYI (blue) and FYI (red). Plot (c) is the daily solar heat input. Plot (d) is the time averaged solar heat input (from Perovich and Polashenski 2012).

Evidence suggests that the sea ice albedo feedback loop in the Beaufort Sea is being enhanced by the early onset and increased areal expansion of the seasonal MIZ. As sea ice retreats deep in the Beaufort Sea, it results in large area of open water available to absorb solar input and store it has heat in the IOBL (Lee et al. 2012). The replacement of MYI by FYI in the region also enhances this positive feedback loop. Hudson et al. (2013) suggest that the increase in the coverage of meltponds characteristic of FYI, compared to MYI, further contributes to increasing the heat content of the IOBL. They

find that meltponds, collections of melted water sitting atop ice, have dynamic and low albedo values which contribute to the absorption and transmittance of solar radiation.

2. Ocean-to-Ice Heat Flux

Stanton et al. (2012) found that heat stored from solar radiation in the IOBL can be transferred from the ocean to the base of the ice and become available for the basal melt of ice. They suggest that this transfer process, ocean-to-ice heat flux, can be enhanced from increased absorption and transmission of solar radiation in the IOBL. The ocean-ice-heat flux is determined by the heat content in the IOBL, turbulence in the IOBL, and the stratification of the pycnocline below the IOBL (Shaw et al. 2009). The heat stored in the relatively warm layers below the IOBL is not available for vertical mixing under normal conditions due to the presence of the strong permanent thermocline which acts to thermodynamically decouple the two layers (Shaw et al. 2009). Stanton et al. (2012) observed that enhanced solar input results in larger ocean-to-ice heat fluxes and basal ice melt. Additionally, they concluded that thinner FYI responds easier to wind forcing, thereby enhancing shear induced turbulence necessary to vertically mix the heat upward and become available for the basal melt of ice.

Ocean-to-ice heat flux (referred to as heat flux for the remainder of this study) values in the IOBL are controlled by numerous conditions. Shaw et al. (2009) found that two important conditions are the depth of the IOBL and the departure from freezing of the IOBL. For this study, departure from freezing will be taken as a measure of how far the local temperature of a layer is from the freezing temperature of seawater, and represents the heat available for basal melt of the ice cover (Shaw et al. 2009). Heat fluxes resulting from ice-generated turbulence can be calculated from the eddy correlation technique and Equation (2). The eddy correlation technique is a statistical heat flux calculation method where the vertical transfer of heat is the result of eddy motion in the IOBL (McPhee 2008).

$$Q = \rho_0 c_p \overline{w'T'} \tag{2}$$

where ρ_0 is the density of seawater and c_p is the specific heat of seawater (McPhee 2008). The vertical transfer of temperature, $\overline{w'T'}$, is measured directly by in-situ instrumentation and is averaged over time to estimate the covariance.

3. Surface Heat Budget of the Arctic Experiment (SHEBA)

One of the most extensive experiments undergone in the Arctic region, the Surface Heat Budget of the Arctic Experiment (SHEBA) was a nearly yearlong experiment to study the heat exchange processes of the polar regions (Shaw et al. 2009). Supported by the Canadian Coast Guard icebreaker *Des Groseilliers*, observations were collected simultaneously across the atmosphere-ice-ocean interface (Shaw et al. 2009), a substantial data set that is still being analyzed to this day. According to Perovich (2005), theoretical work from the 1990s estimated that 69% percent of the incoming solar radiation would be reflected, 27% absorbed, and 4% would be transmitted. He showed that SHEBA data matched closely with the calculations, where observations showed 68% of the incoming solar radiation was reflected, 24% was absorbed, and 8% was transmitted. The study attributed the doubling of transmission as a result of thinner ice observed during the SHEBA experiment compared to historical observations.

Using SHEBA observations, Shaw et al. (2009) conclude that basal melting of ice during the collection period was largely reflective of the amount of solar radiation input into the IOBL. Observations from this study also show the varying IOBL temperature and salinity conditions with varying locations in the Beaufort Sea. The time series of summer heat fluxes observed is provided in Figure 10. Large heat fluxes during the summer measurements converted stored heat to latent heat via ice melting, resulting in 28-35% reduction in ice growth and contributing to a nearly 15% decrease in ice the ensuing winter season (Shaw et al. 2009). They conclude that data collected during this experiment suggests that decreasing ice extent and thinning plays a large role in controlling the heat distribution of the IOBL. By reducing the ice extent and thickness at the end of a nominal summer, the ice pack and IOBL is subsequently preconditioned to absorb and store more solar heat the following melt cycle.

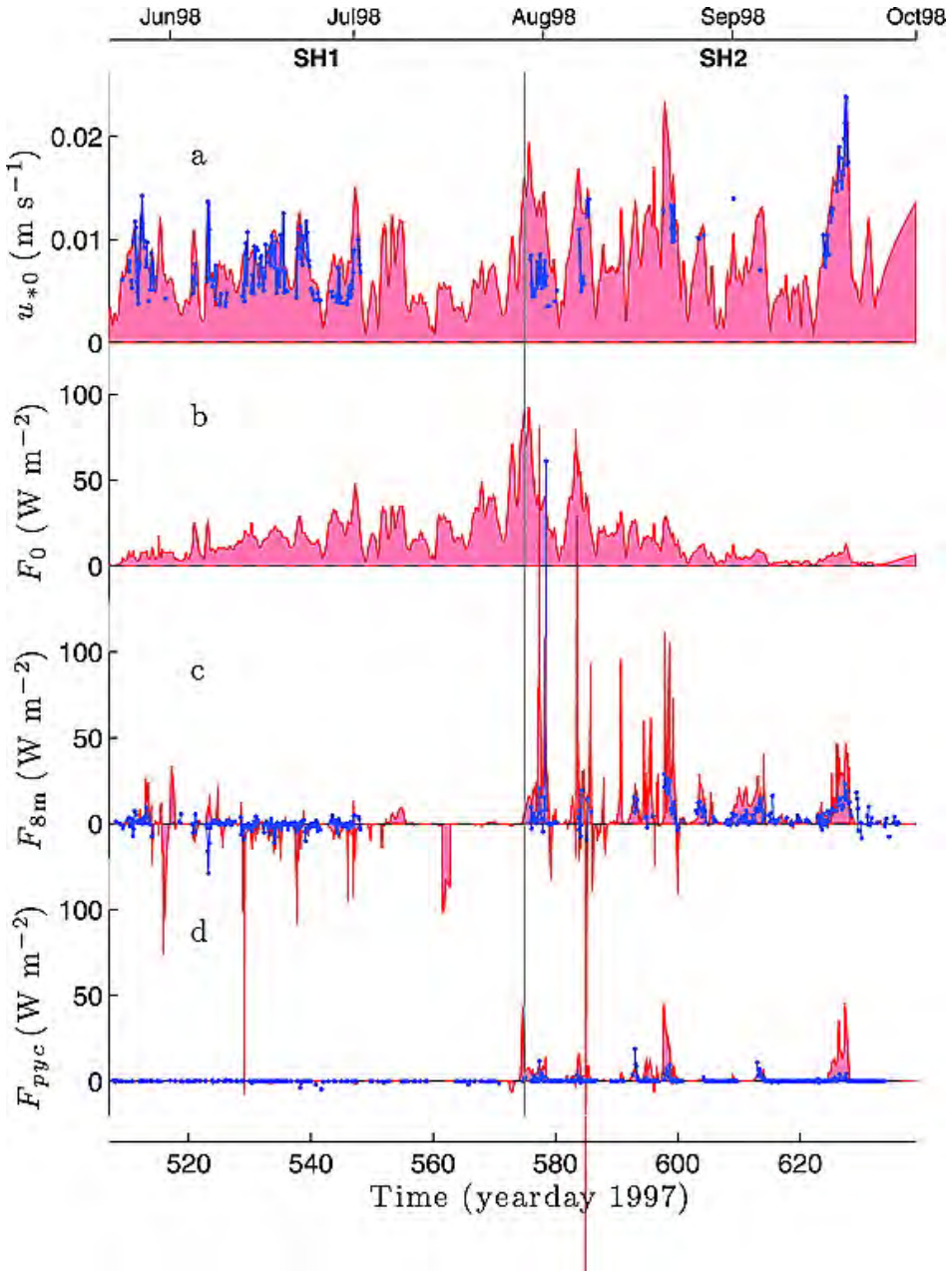

Figure 10. SHEBA measurements of a) friction velocity, b) ocean-to-ice heat flux, c) heat flux at 8 meters depth, and d) heat flux at the bottom of the IOBL. While the average heat flux was , be 7.6 W m^{-2} over the entire experiment, large heat fluxes were observed during the summer melt season (from Shaw et al. 2009).

THIS PAGE INTENTIONALLY LEFT BLANK

II. DATA COLLECTION AND DATA PROCESSING

This thesis will utilize data collected from NPS Autonomous Ocean Flux Buoys (AOFBs), Woods Hole Oceanographic Institute (WHOI) Ice-Tethered Profiles (ITPs), and high-resolution (1-10 meter) visible satellite imagery. All satellite imagery collected is unclassified and approved for public release (United States Geological Service (USGS) 2014). Various data processing techniques will be used to identify usable images and quantify open water, meltpond, and ice floe fraction. All satellite images will be presented in the Universal Transverse Mercator (UTM) coordinate system. AOFB and ITP data processing techniques are used to correct data and apply data offsets to compare measurements from the two different sensors.

In this study, open water fraction will be taken as the amount of open water available to absorb incoming solar radiation for a given image. It will be comprised of open ocean fraction, a measure of the image area comprised of open ocean, and meltpond fraction, a measure of the image area comprised of meltpond coverage.

A. DATA COLLECTION

1. Satellite Imagery

All of the satellite imagery processed in this thesis is provided on the USGS public access website. Established in the 1990s, the USGS Global Fiducials Program (GFP) is a joint effort between academia, the intelligence community, and federal civil services to support research into understanding the Earth Science System (USGS 2014). Archived declassified high resolution satellite images from intelligence assets approved for public release are stored in the GFP Global Fiducials Library (GFL) for various global regions, including the Arctic (USGS 2014). Each image contains geo-referenced image data files containing the image metadata. The images are from the visible portion of the EM spectrum (USGS FAQ 2014) and are thus highly affected by cloud cover. An example high resolution image can be seen in Figure 11. This image shows a 22km by 21km view of sea ice from the Beaufort Sea.

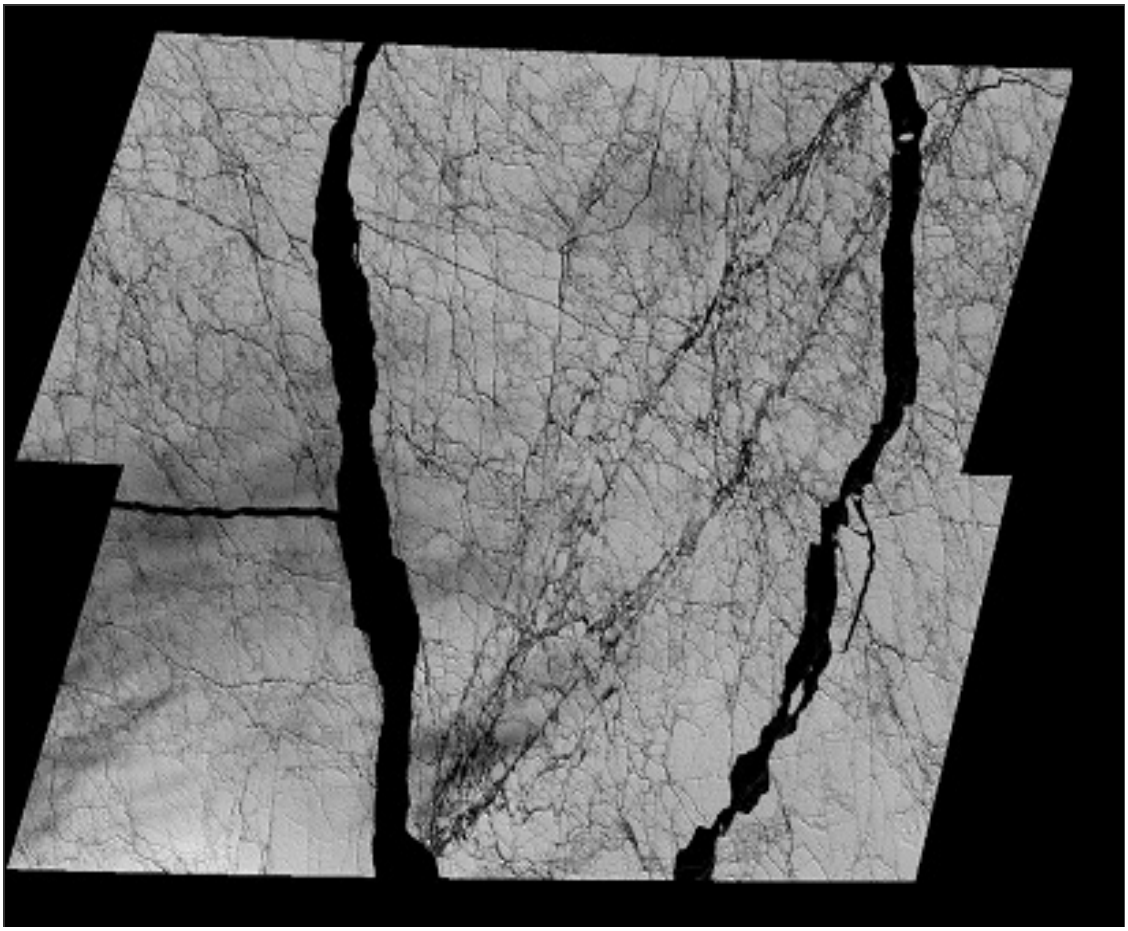

Figure 11. Example of a declassified high-resolution satellite image, approved for public release, of sea ice in the Beaufort Sea available on the USGS GFP GFL (from USGS 2014).

2. Autonomous Ocean Flux Buoys (AOFBs)

Funded by the National Science Foundation (NSF) Office of Polar Programs, Research Professor Timothy Stanton and the Turbulence Research Group at NPS developed AOFBs to make long term, unattended observations of ocean-ice coupling processes in the Arctic (NPS AOFB 2014). According to the NPS AOFB website, the AOFB is an autonomous platform designed to directly measure vertical turbulent heat and salt fluxes, current profiles, and other ocean properties in the ocean mixed layer below the ice. The NPS AOFB program deploys these buoys on ice floes to make long term observations in the ocean-ice system over periods of 1 to multiple years. From the program website, 28 AOFBs have been deployed by NPS personnel in both the

Transpolar Drift and the Beaufort Sea between 2002 and 2013. In 2014, one AOFB was deployed in the Transpolar Drift and 3 AOFBs were deployed in the Beaufort Sea (NPS AOFB 2014). A map of the AOFBs deployment positions and their drift trajectories for the AOFBs used in this study is provided in Figure 12.

An AOFB consists of two main components: 1) surface buoy; and 2) upper ocean instrument package (NPS AOFB 2014). A schematic of the AOFB with the flux sensor package, located about 4m below the ice, is provided in Figure 13. The surface buoy contains a main processor / power / data storage board, a GPS receiver, iridium modem, large lithium battery bank, and a solar power system used during the summer months. (NPS AOFB 2014). According to the AOFB Program website, two-way communication with the NPS network occurs four times per day to allow for near real time data updates, and allows sampling intervals to be remotely controlled for each instrument to conserve power while addressing specific science questions. The surface buoy supports the upper ocean instrument package that houses the downward looking Acoustic Doppler Current Profiler (ADCP) and a flux package (NPS AOFB 2014). The custom-built flux package includes co-located low noise acoustic travel time current meter and temperature and conductivity sensors (NPS AOFB 2014). The in-situ sensors used by the NPS AOFB Program measure momentum, heat, and salt fluxes through the water column using the direct eddy correlation technique described earlier. A high-resolution thermistor string provides vertical thermal structure between the flux package depth and the ice to study summer heating conditions (NPS AOFB 2014). Data are updated every four hours to the NPS AOFB program website: http://www.oc.nps.edu/~stanton/fluxbuoy/index.html) (NPS AOFB 2014).

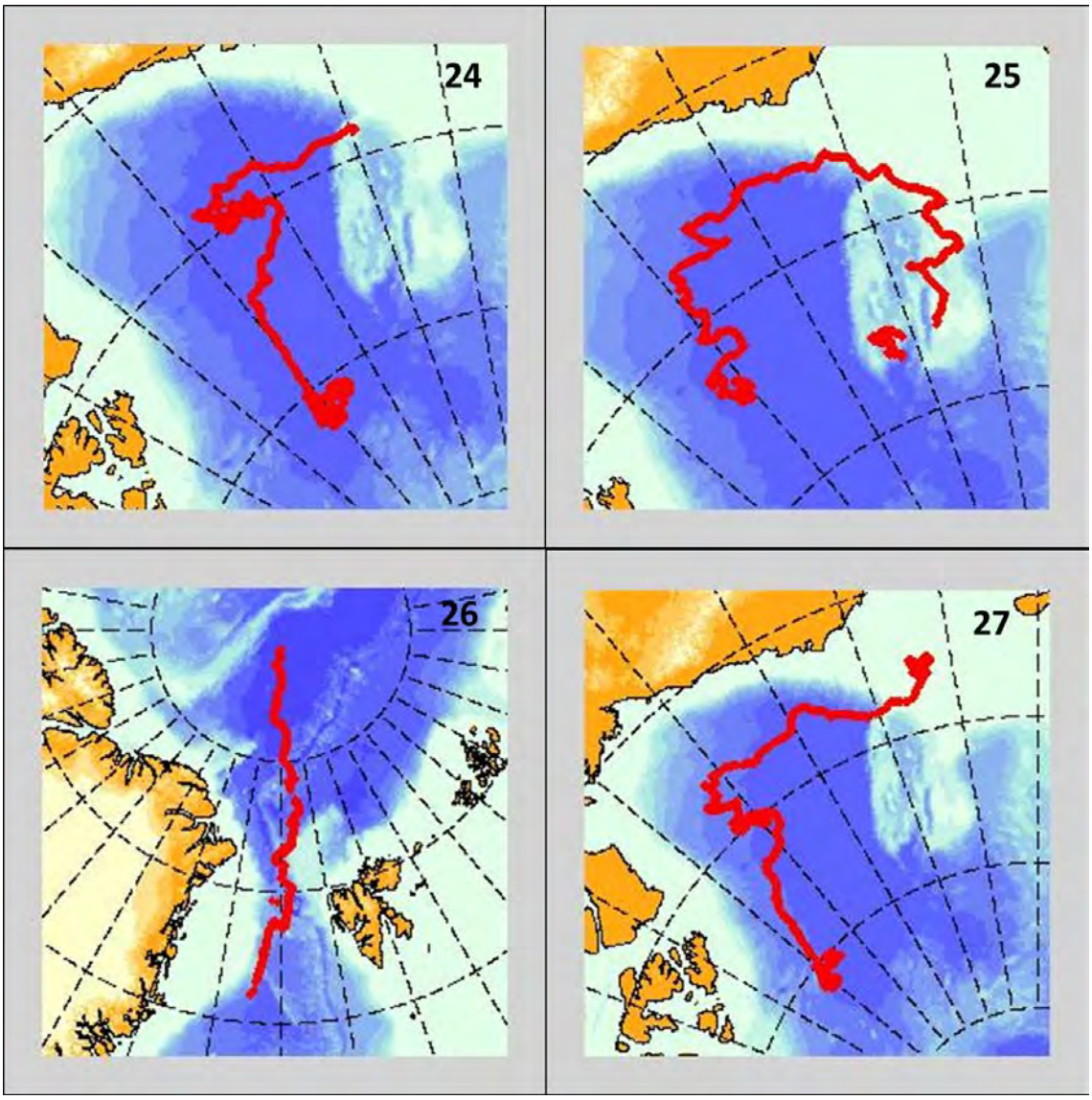

Figure 12. Overview of NPS AOFB deployments for buoys (24, 25, 26, 27) used in this study (from NPS AOFB 2014).

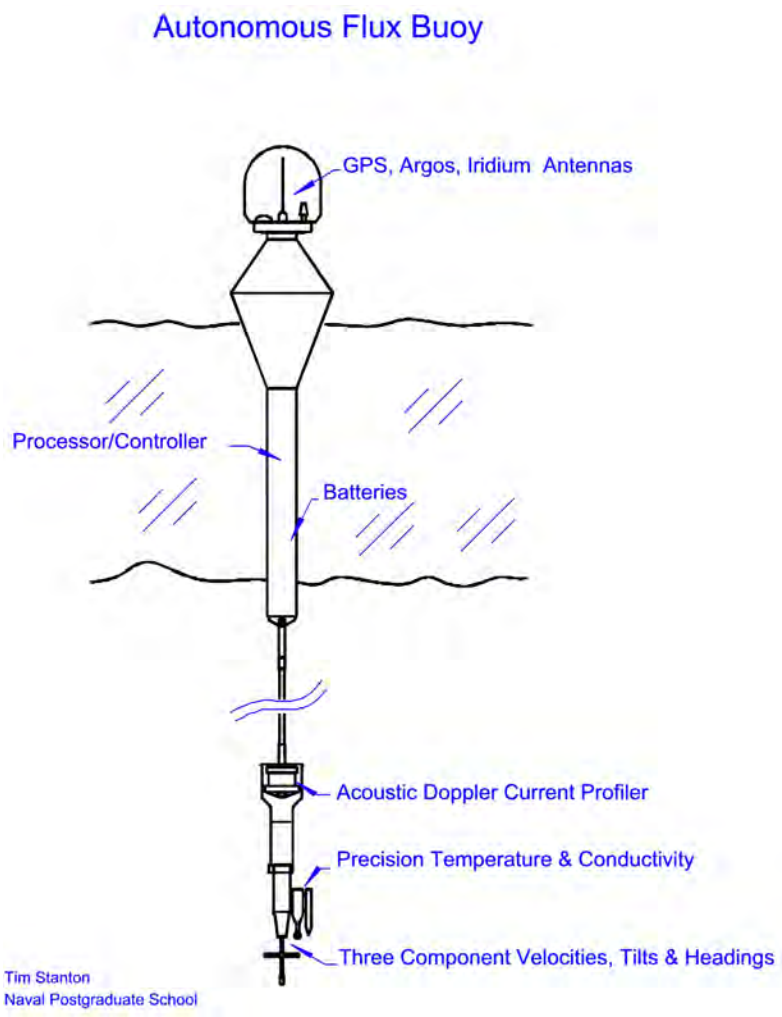

Figure 13. Schematic diagram of the NPS AOFB (from NPS AOFB 2014).

3. Ice-Tethered Profilers (ITPs)

Typically deployed on the same ice floes as the NPS AOFBs are ITPs developed by the WHOI. ITPs are an autonomous system designed for deployment on sea ice for periods up to three years in order to measure upper ocean temperature and salinity profiles (WHOI ITP 2014). Krishfield et al. (2006) provide a technical description of the profiler, consisting of a surface buoy, a tether, and an underwater package (Figure 14). The surface instrument contains a power supply pack, GPS unit, iridium satellite and antennae for real time data transmission to WHOI (Krishfield et al. 2006). From the technical report, the tether is a weighted plastic jacketed wire rope and provides both mechanical and electrical connection between the surface instruments and the profiler for

depths up to 800m. According to the ITP Program website, the underwater package houses a low power CTD as well as mechanical wire crawler mechanism to traverse the profiler up and down the tether.

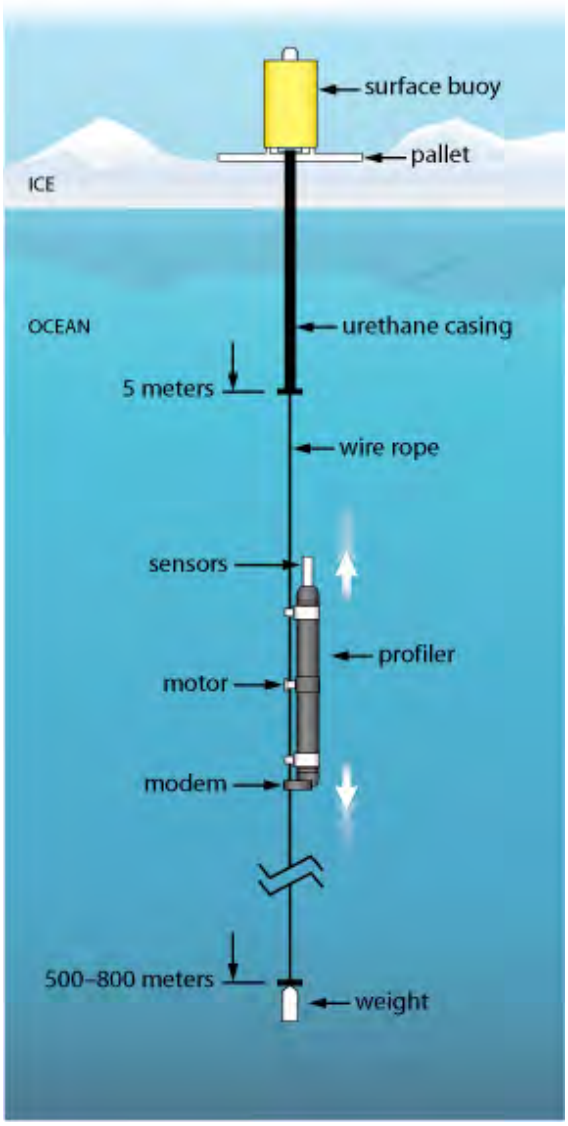

Figure 14. WHOI ITP schematic (from Krishfield et al. 2006).

a. AOFB – ITP Correlation

The incorporation of ITP data in this study has allowed the surface mixed layer melt heat content to be estimated. In order to determine which ITP data sets would be utilized, the AOFB deployments had to be matched to the correct ITP mission. This was accomplished by reviewing the ITP mission overviews for each deployment from the WHOI ITP website, which recorded the deployment of AOFBs as well. Table 1 provides a summary of the findings.

ITP Number	AOFB Number	ITP Mission Status	ITP Mission Dates
6	10	Complete	9/4/2006-10/11/2009
7	11	Complete	4/28/2007-2/7/2008
12	14	Complete	9/14/2007-9/22/2009
13	12	Complete	8/13/2007-9/7/2008
18	13	Complete	8/16/2007-10/21/2008
19	15	Complete	4/7/2008-11/22/2008
20	16	Complete	8/8/2008-2/18/2009
23	17	Complete	8/5/2008-9/3/2011
38	20	Complete	4/19/2010-9/12/2011
42	22	Complete	10/7/2010-2/10/2011
43	21	Complete	10/7/2010-2/10/2011
47	23	Complete	4/11/2011-10/4/2012
56	26	Complete	4/15/2012-5/3/2013
65	24	Complete	8/27/2012-9/10/2013
54	25	Active	8/6/2011
61	28	Active	4/10/2013
66	27	Active	8/27/2012
70	30	Active	8/25/2013
76	31	Active	4/11/2014
77	33	Active	3/9/2014
78	32	Active	3/11/2014

Table 1. AOFB-ITP mission correlation summary.

B. INITIAL IMAGE PROCESSING METHOD

MATLAB scripts were written to perform image analysis of high-resolution satellite images used in this study to assess meltpond coverage and open water fraction

around the AOFB trajectory. When possible, functions and scripts available from the MATLAB Image Processing Toolbox, MATLAB website, or from the NPS Turbulence Group processing toolbox were utilized.

1. Selecting Initial Images for Processing

In order to select images that captured AOFB locations across the Arctic, metadata files for each Arctic image on the USGS GFL were scanned. Relevant image data (Table 2) was extracted. The metadata was used to determine if an AOFB position was located inside the image bounding box within 24 hours of the image day. This procedure determined that 102 satellite images, deemed "hit" images, were potentially available for further analysis. A summary of the AOFB hits can be seen in Table 3. From over 1100 images available, less than 1% met these initial criteria.

Variable	Description
XML File Name	.xml file of image being scanned
Time Zone	UTM time zone
Image Year	4 digit *YYYY* format
Image Month	2 digit *MM* format
Image Day	2 digit *DD* format
Bounding Coordinates	North, South, East, and West box bounding coordinates in decimal degrees and UTM coordinates
Solar Angle Information	Azimuth and Zenith information

Table 2. List of variables extracted from image metadata files.

AOFB Number	Number of "Hits"	AOFB Number	Number of "Hits"	AOFB Number	Number of "Hits"	AOFB Number	Number of "Hits"
10	0	16	0	22	0	28	0
11	0	17	2	23	0	29	0
12	0	18	12	24	22	30	0
13	0	19	0	25	23	31	0
14	0	20	0	26	16	32	0
15	0	21	0	27	27	33	0

Table 3. Summary of AOFB "hit" information. Yellow shading indicates an AOFB was located within the available image.

2. Processing Usable Images

For each initial "hit" image, cartographic information was extracted from the metadata. This provides the bounding box coordinates of the image in both latitude-longitude (decimal degrees) and the UTM projection (northing and easting). Using Equation (3) and (4), the center coordinates of the bounding box are calculated. Although the equations are presented in latitude and longitude, the same relationship is valid UTM northing and easting coordinate calculations as well.

$$\frac{Lat_{NWcorner} + Lat_{NEcorner} + Lat_{SWcorner} + Lat_{SEcorner}}{4} = Lat_{Center} \tag{3}$$

$$\frac{Lon_{NWcorner} + Lon_{NEcorner} + Lon_{SWcorner} + Lon_{SEcorner}}{4} = Lon_{Center} \tag{4}$$

While the time of the image is not given explicitly in the image metadata, it can be calculated using the provided solar angle information. The solar zenith angle is the angle measured from directly over the buoy position toward the sun; solar azimuth angle defines the direction of the sun from the buoy (U.S. Naval Observatory 2005). Azimuth and zenith angles for a 24-hour period were calculated based on the center coordinates for each image. The least absolute deviation optimization technique (Equation [5]), was applied to determine to be the time of the image. An illustration of this technique can be seen in Figure 15.

$$Difference_{min} = (zenith_{image} - zenith_{calculated})^2 + (azimuth_{image} - azimuth_{calculated})^2 \tag{5}$$

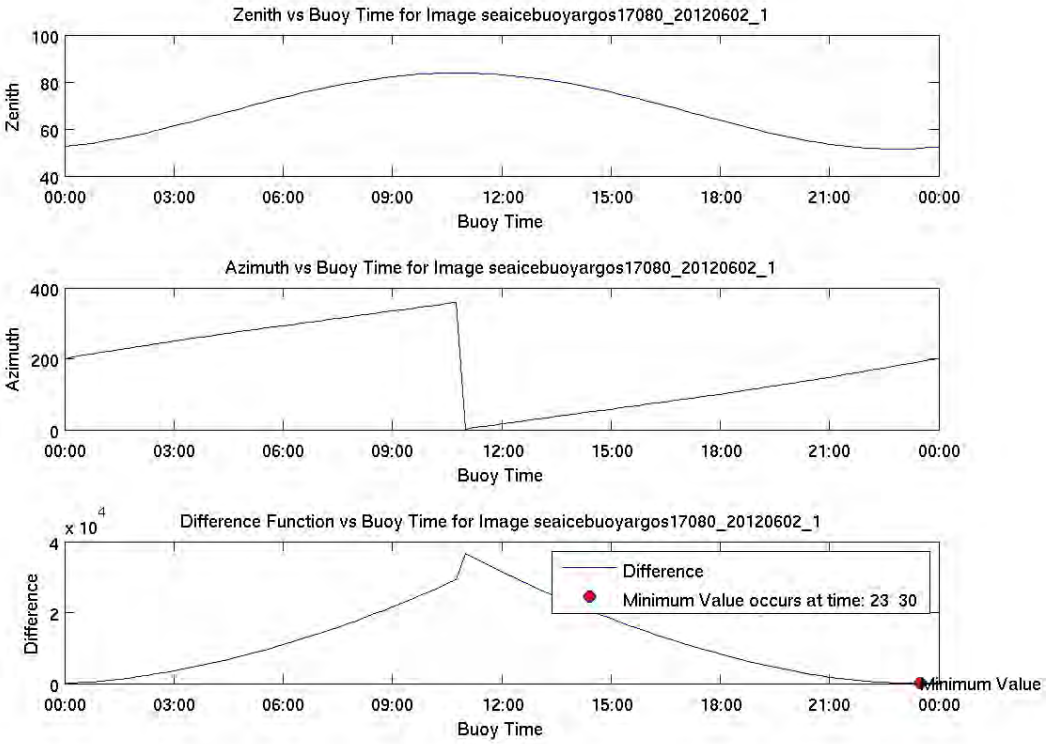

Figure 15. Example azimuth, zenith, and time of day calculations from a known satellite image center position and time of day. In this example, the minimum value indicates the time of day of the image is 2330 on 02 June 2012.

a. Determining Closest Buoy Position

Once the time of the image was calculated, the appropriate AOFB yearday data is scanned to determine the closest AOFB record number to the image time. The corresponding coordinate position was extracted and used to determine if the AOFB position at the time closest to the image capture time lied within the image bounding box. If the closest AOFB positon was outside of the image, the image is classified as a "miss" and no further processing was done (Figure 16). If the closest AOFB position was within the image, the image is retained as a "hit", as seen in Figure 17. For all "hit" images, a subset image was generated with image zoomed on the AOFB position was zoomed around, as seen in Figure 18. From the 102 initial "hit" images, only 29 images (less than 2.5%) contained the AOFB within the boundaries at the time of the image.

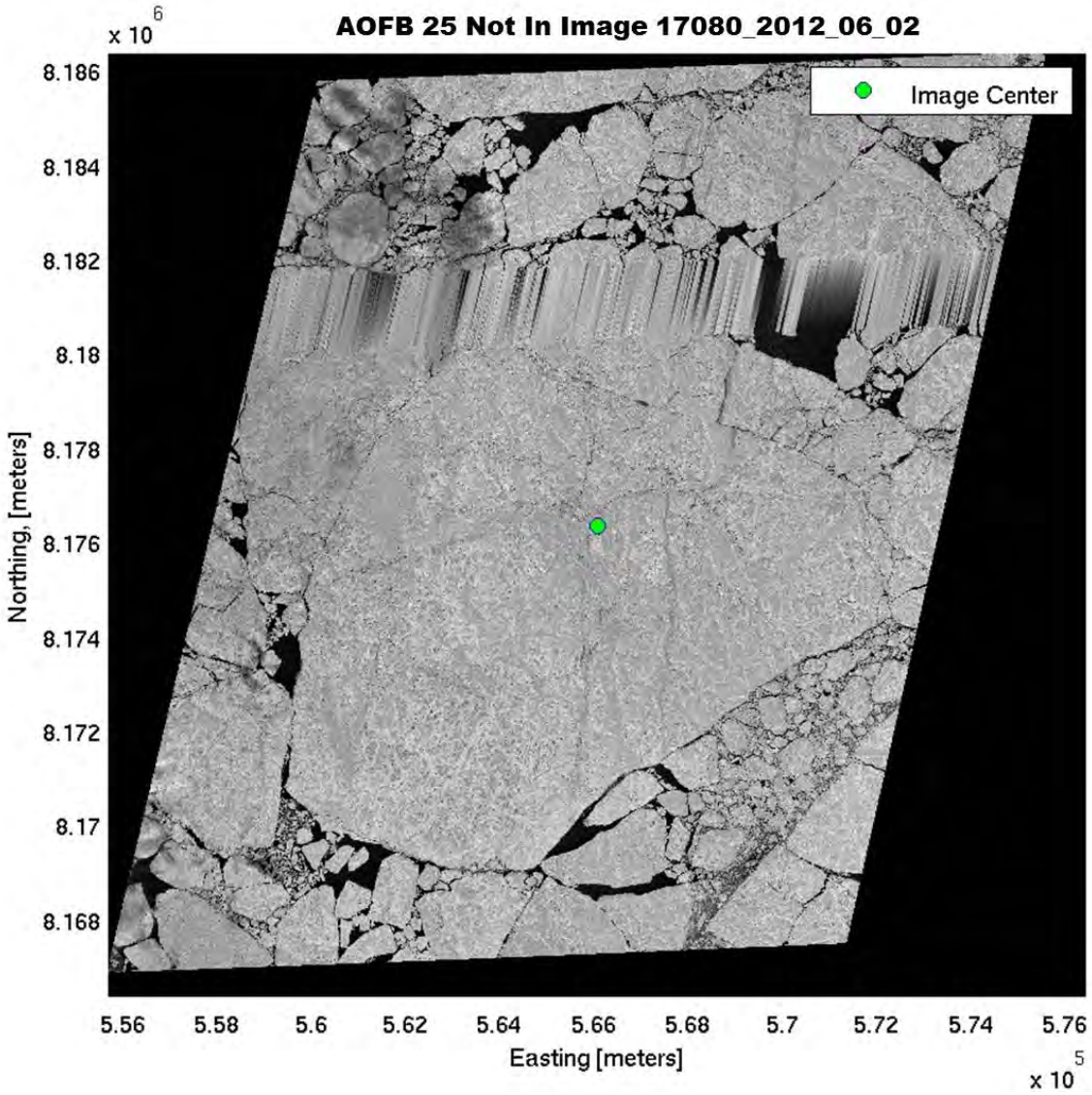

Figure 16. Example of a “miss” image. In this image, the closest AOFB position to the image capture time does not fall within the image boundaries. No further processing is done.

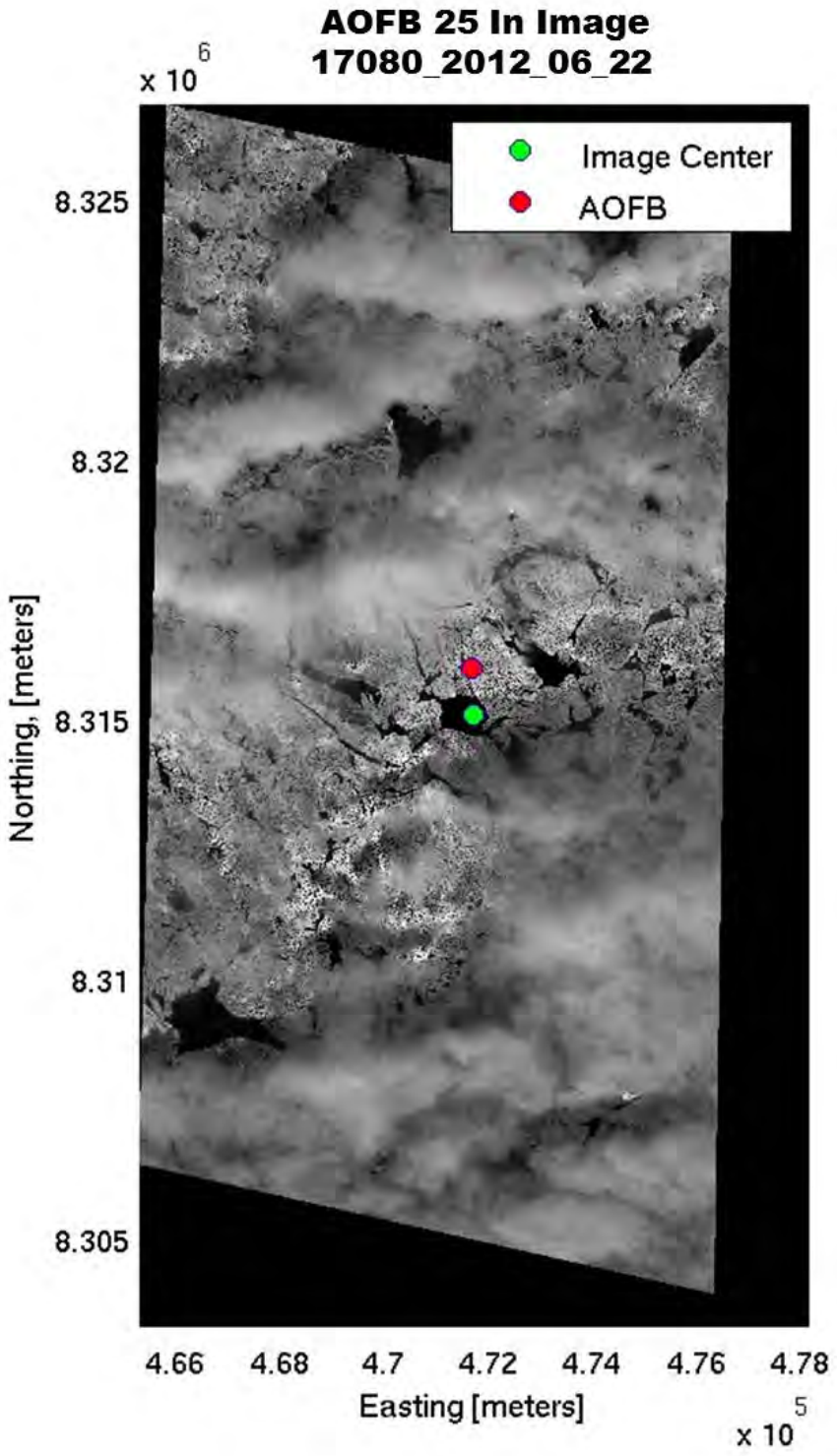

Figure 17. Example of a "hit" image. In this image, the closest AOFB position to the image capture time falls within the image boundaries. This image is retained for further processing.

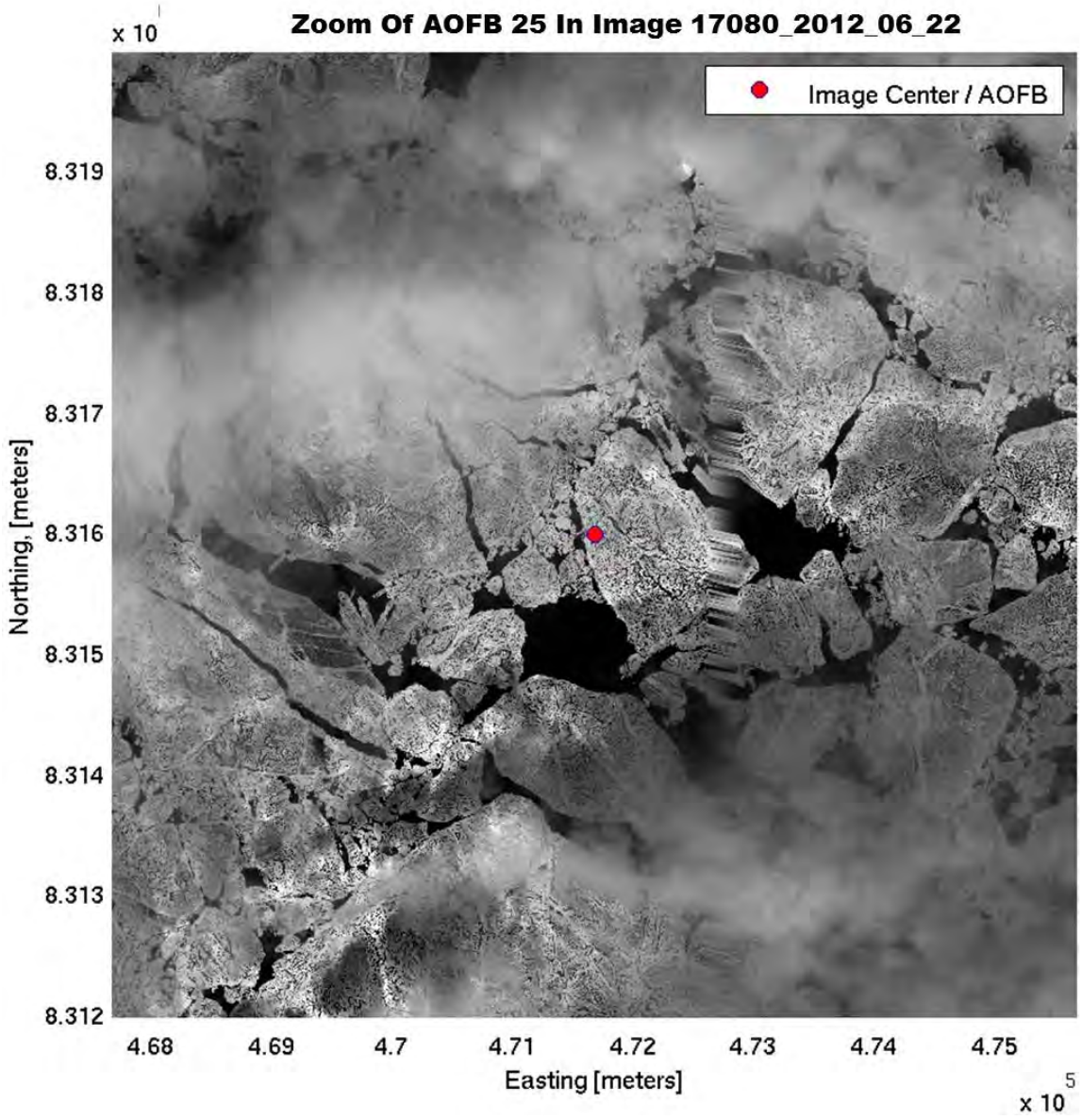

Figure 18. Zoomed in view of an AOFB position for the "hit" image from Figure 17.

3. Determining AOFB Track and Region Breakdown

For the "hit" images, the AOFB positions were plotted 12 hours ahead and 12 hours behind the AOFB position at the image capture time (Figure 19). With the AOFB track progression known, the ice properties in the ocean mixed layer that the ice-supported AOFB advects over were determined in order to estimate the amount of solar radiation entering the ocean mixed layer ahead. As the objective is to identify the ice and

ocean properties in the vicinity of the buoy, it is useful to evaluate these properties over a focused area smaller than the default image. To accomplish this, a series of 500m by 500m boxes were established along the buoy trajectory at 500m intervals (Figure 20). For each sub-region, the 500m by 500m box centered on the AOFB position was zoomed on (Figure 21). In each case, the matrix containing the pixel intensity values was saved for further processing.

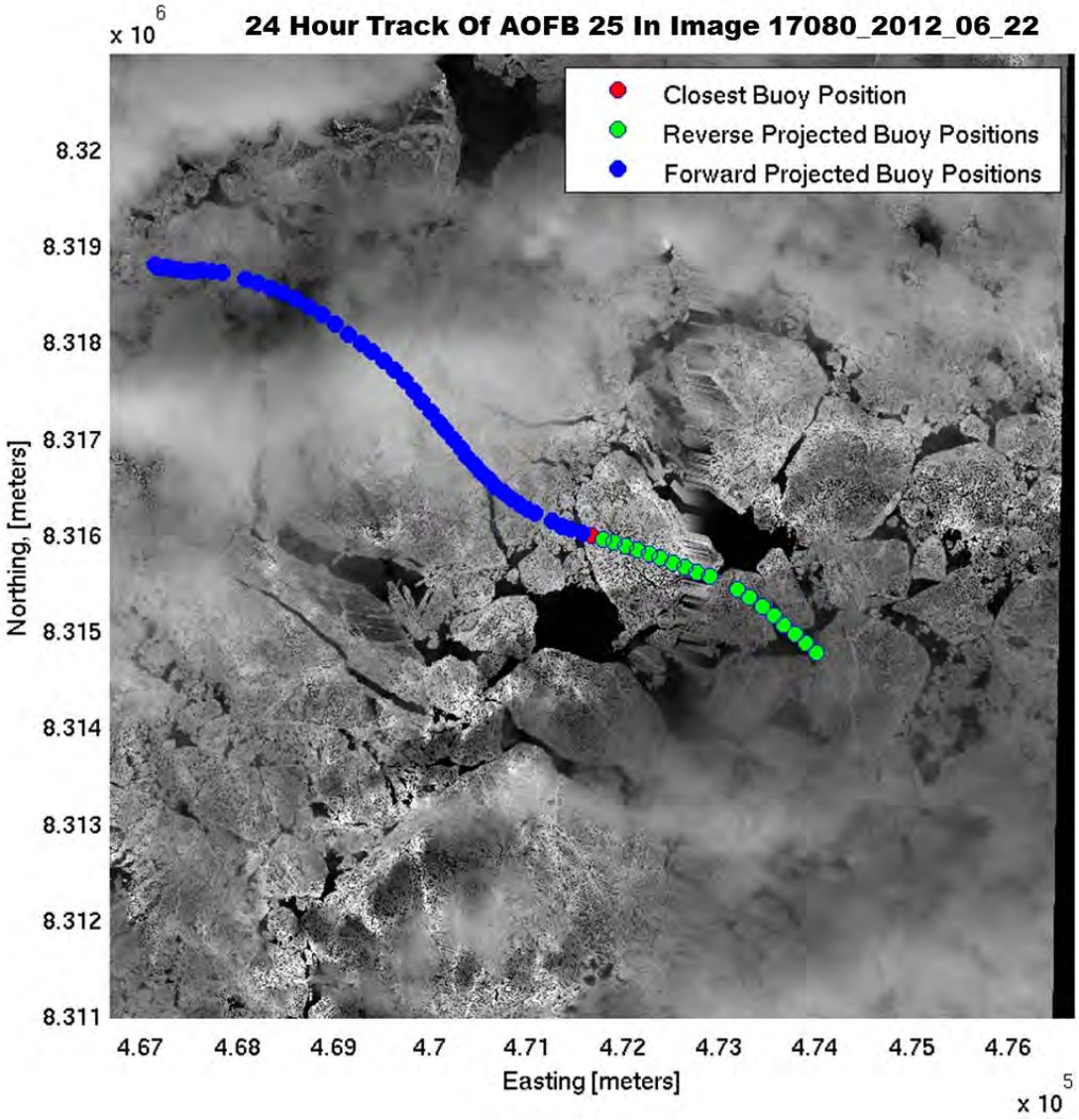

Figure 19. Example of a 24 hour AOFB trajectory. The red represents the record position of the closest AOFB to the time of the image. Green is the previous 12 hour position records. Blue is the ensuing 12 hour positions records.

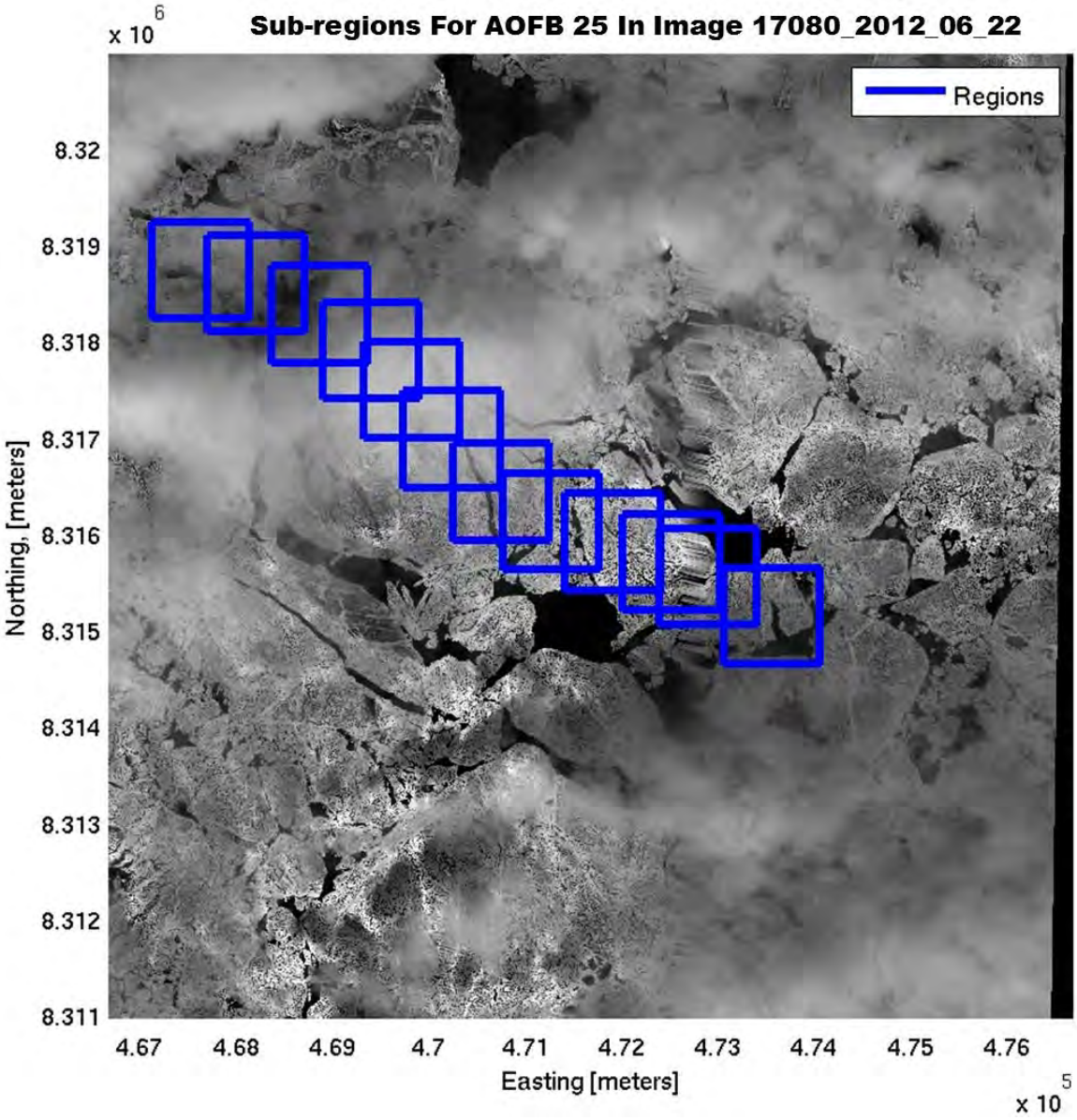

Figure 20. 500m x 500m sub-regions established around AOFB positions at a 500m interval.

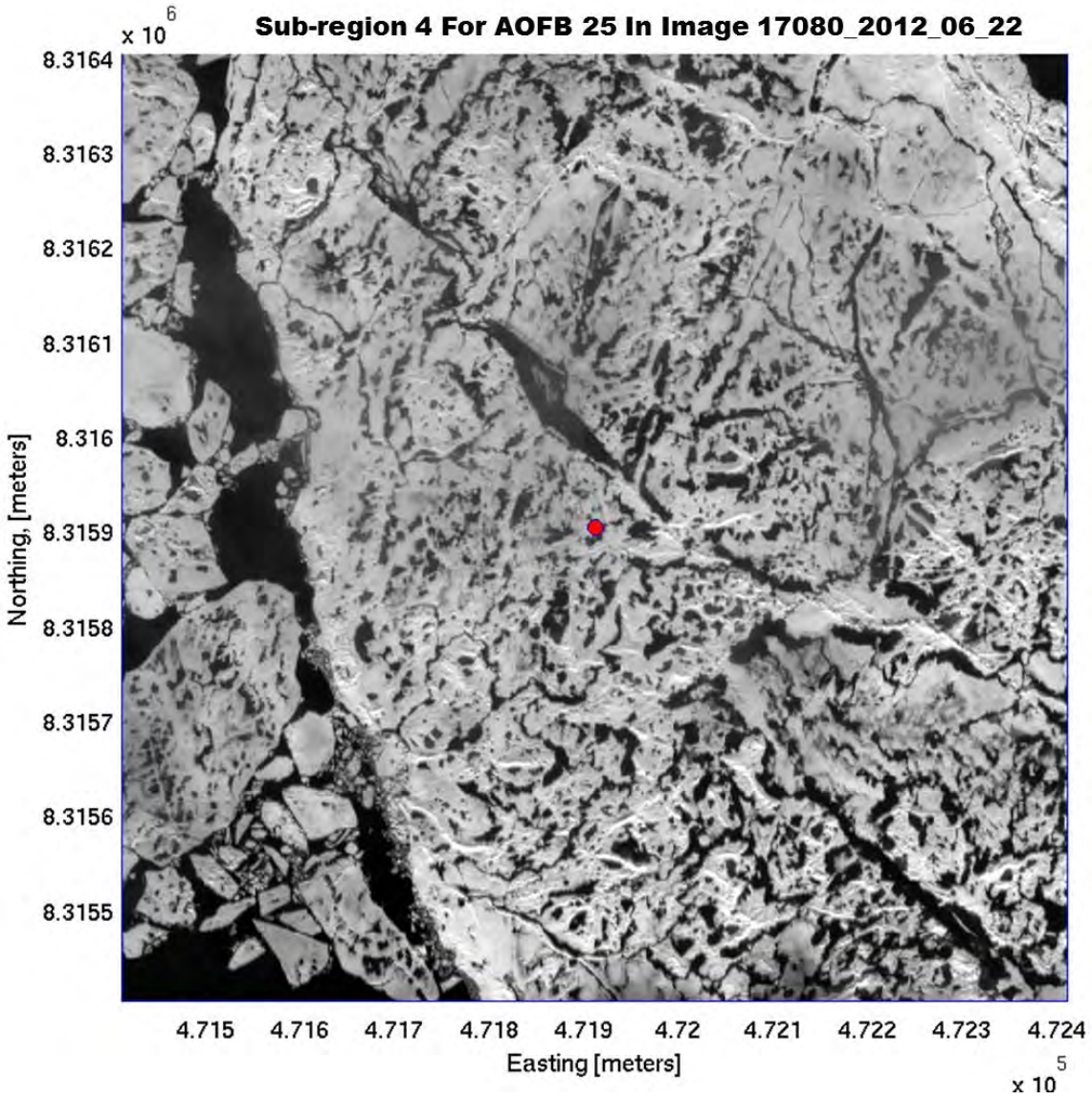

Figure 21. Zoomed view of a 500m by 500m sub-region from Image Two, Sub-region Four (Figure 20) Note the open water, ice floe, and meltpond features that are clearly visible.

From the 29 "hit" images, over 300 square sub-regions were available for further analysis. Up until this point in the methodology, no effort was made to determine the quality of the image to see if it would be useful for further analysis. For this study, the criteria for a quality image was: 1) cloud cover was not significant enough to prevent the identification of ice features; 2) cloud cover did not prevent the open water, meltpond, and ice floe fraction from being calculated; and 3) the majority of the AOFB trajectory

was outside of image black-space. Images with heavy cloud cover were rejected, such as the example provided in Figure 22. A summary of the image quality screening is provided in Table 4. Of the 29 "hit" images, seven were chosen for further analysis.

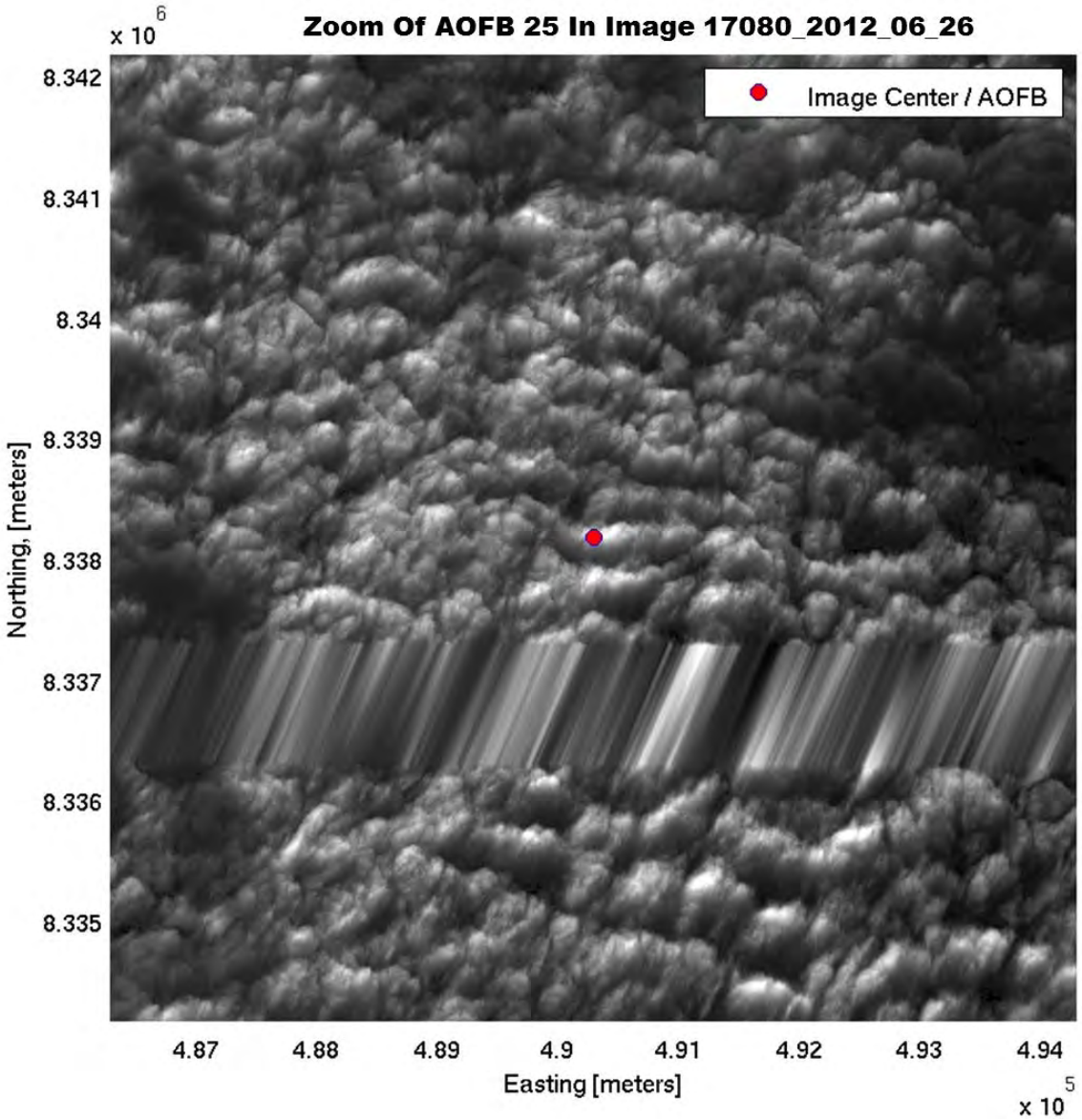

Figure 22. Example of an image rejected for further analysis due to heavy cloud cover. The closest AOFB position is plotted in red.

Image Number	Ok For Further Processing?	Supplemental Information
1	Yes	Processed for further analysis
2	Yes	Processed for further analysis
3	No	Heavy cloud cover
4	No	Heavy cloud cover and proximity to region black-space
5	No	Heavy cloud cover and proximity to region black-space
6	No	Heavy cloud cover
7	No	Heavy cloud cover
8	No	Heavy cloud cover and proximity to region black-space
9	No	Heavy cloud cover
10	No	Heavy cloud cover
11	No	Heavy cloud cover
12	No	Heavy cloud cover
13	Yes	Processed for further analysis
14	No	Heavy cloud cover
15	Yes	Processed for further analysis
16	No	Heavy cloud cover
17	Yes	Processed for further analysis
18	No	Heavy cloud cover
19	No	Heavy cloud cover
20	No	Heavy cloud cover
21	No	Heavy cloud cover and proximity to region black-space
22	Yes	Processed for further analysis
23	No	Heavy cloud cover and proximity to region black-space
24	No	Heavy cloud cover and proximity to region black-space
25	No	Heavy cloud cover
26	Yes	Processed for further analysis
27	No	Heavy cloud cover and proximity to region black-space
28	No	Heavy cloud cover and proximity to region black-space
29	No	Heavy cloud cover and proximity to region black-space

Table 4. Summary of the image quality screen. Yellow shading indicates the seven images used in this study for further analysis.

C. PIXEL PROCESSING METHOD

For the remainder of this chapter Image Two (Figure 20), Sub-region Four (Figure 21) will be used an example image to demonstrate the pixel processing techniques applied to the remaining seven "hit" images unless otherwise noted. This image was chosen due to its wide range of features, including the presence of cloud cover, open water, meltponds, and bare ice.

1. Threshold Determination

Each sub-region's pixel intensity matrix was individually loaded into MATLAB. To look at the distribution of pixel values within the image, a histogram of the 256-bit gray-scale pixel intensity values was generated for each sub-region. In gray-scale, the pixel intensity values range from a minimum value of zero (white) to a maximum value of black (255). To complete the pixel processing, a threshold value had to be determined for each image sub-region to distinguish open water, deep meltponds, and ice. Using this chosen value, the gray-scale pixel intensity was converted to binary one and zero; any pixel intensity values lower than the selected threshold are assigned zero and any pixel intensity values greater are assigned a value of one. The goal in selecting a threshold value is to discriminate between sea ice and water.

A robust method was developed to identify the appropriate pixel threshold value to be chosen. An example of a pixel intensity is presented in Figure 23. In this example, a bimodal distribution of the pixel intensity can be easily identified. Picking the threshold value is important. If selected too low, the resulting binary image loses too many open water and meltpond features. This is illustrated in Figure 24, where a threshold of 25 was applied. If the chosen threshold is too high, floe integrity is lost and too many meltpond features are identified, as seen in Figure 25, where a threshold of 125 was applied. This process determined that a threshold slightly greater than the median of the threshold allows for the boundaries between ice floes to be distinguished, while at the same time providing an acceptable level of meltpond discrimination. A threshold value that is slightly greater than the median of the bimodal distribution (60) is presented in Figure 26.

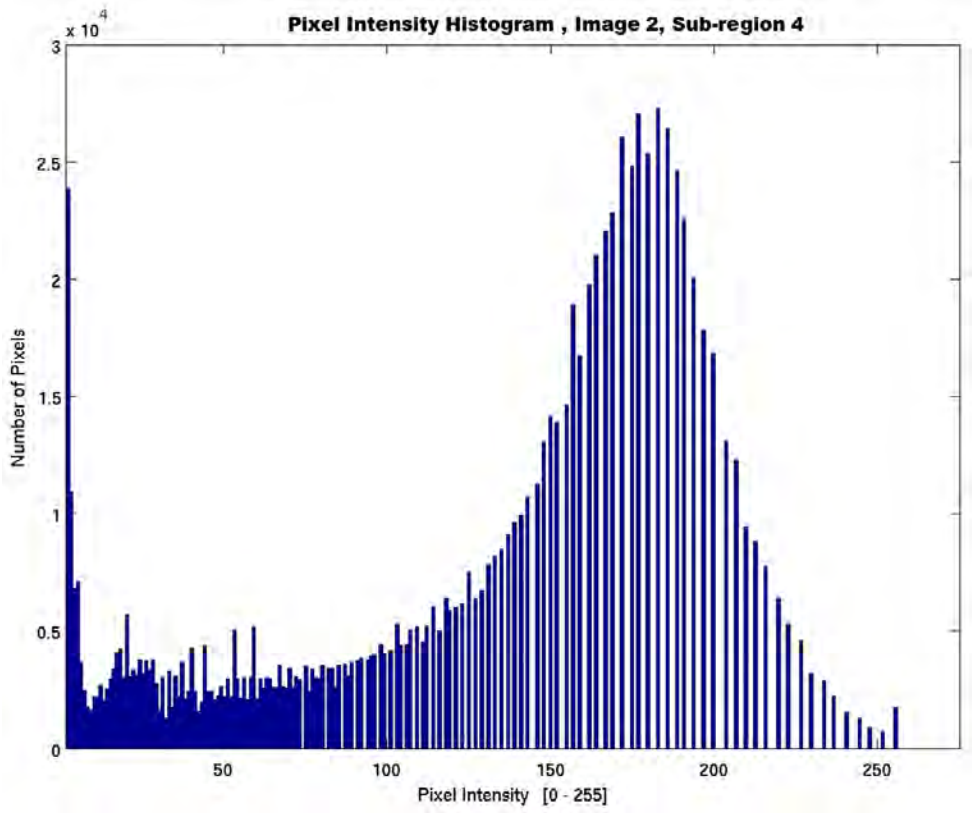

Figure 23. Pixel intensity histogram for Image Two, Sub-region Four. Note the presence of a bimodal distribution pattern (the "u" shaped pattern on the left portion of the histogram).

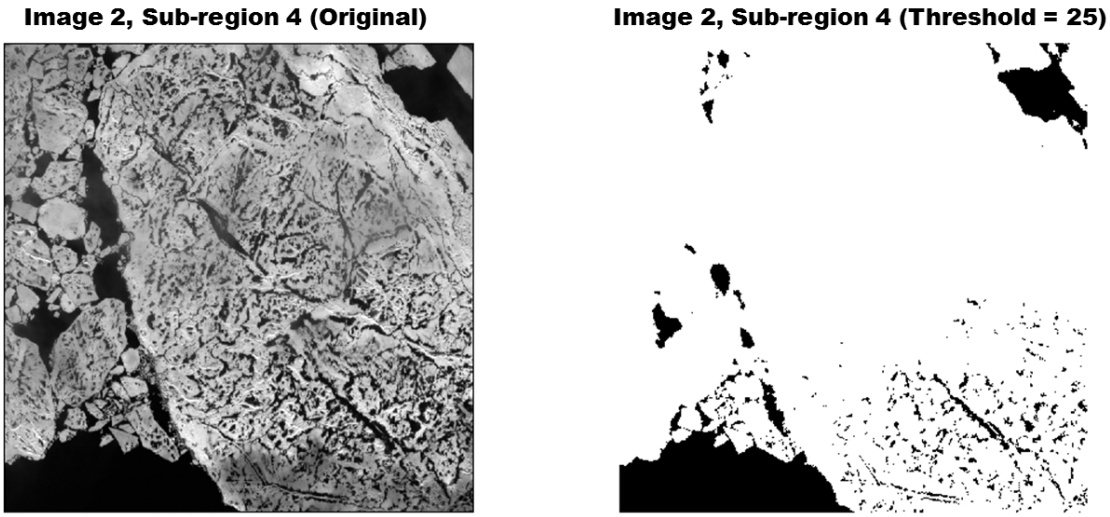

Figure 24. The original grayscale matrix for Image Two, Sub-region Four is seen on the left. On the right is the converted binary black and white matrix plotted with a threshold value of 25.

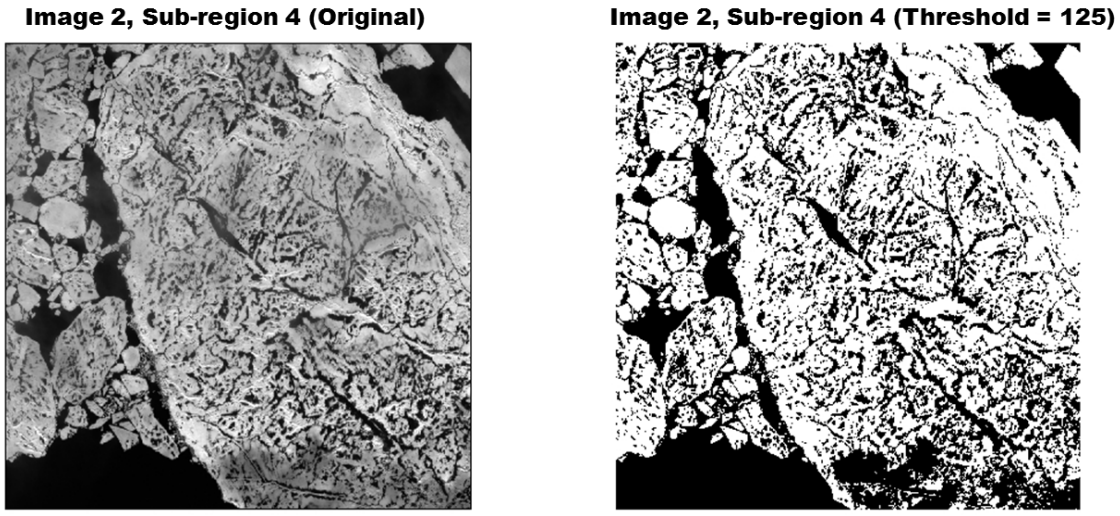

Figure 25. The original grayscale matrix for Image Two, Sub-region Four is seen on the left. On the right is the converted binary black and white matrix plotted with a threshold value of 125.

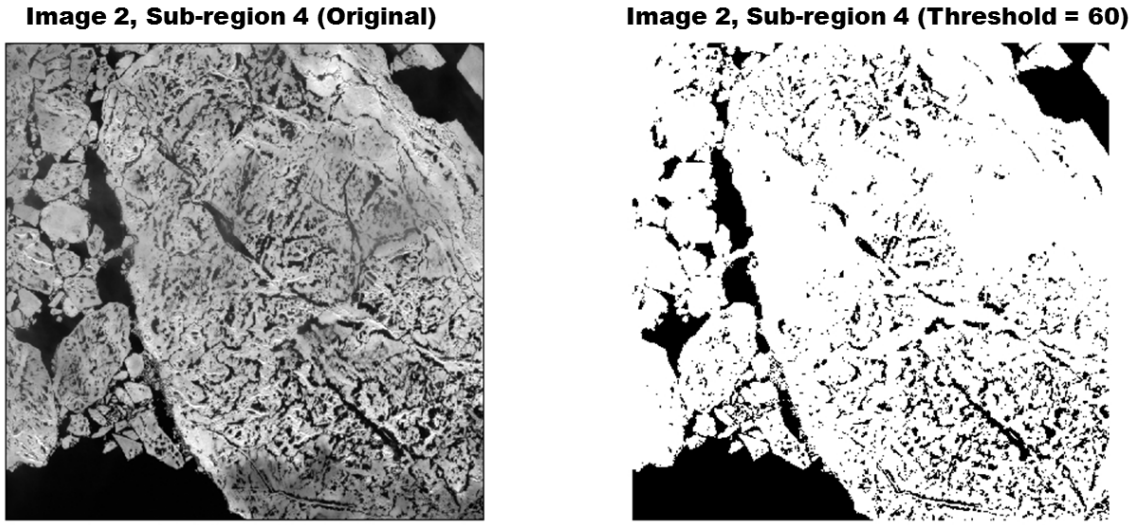

Figure 26. The original grayscale matrix for Image Two, Sub-region Four is seen on the left. On the right is the converted binary black and white matrix plotted with a threshold value of 60.

In sub-regions where the presence of cloud cover slightly degraded the quality of image, a threshold higher than would have normally been chosen was selected. This allowed the algorithm to filter out the open water from the cloud cover, however, meltpond features were not captured well. An example of open water being discerned through cloud cover is provided in Figure 27. Additionally, the option to allow

MATLAB to automatically determine the threshold was also explored. However, since values of zero were returned each time, this option was determined to be un-usable since it treated the entire region as a uniform sheet of ice with no open water or meltponds distinguishable (Figure 28).

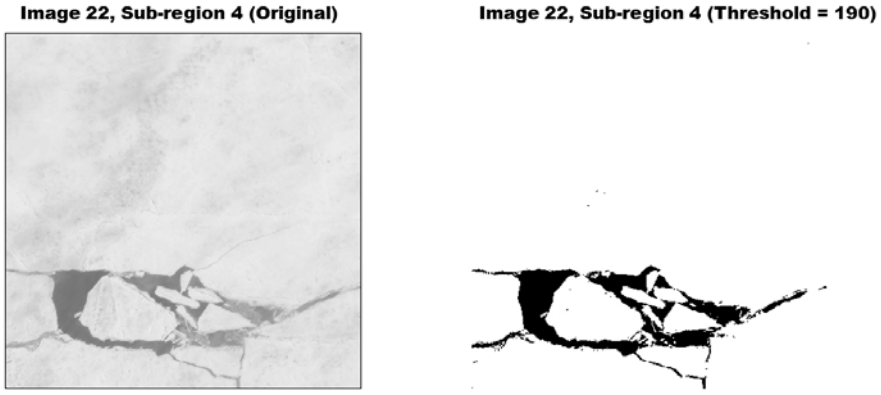

Figure 27. The original grayscale matrix for Image 22, Sub-region Four is seen on the left. On the right is the converted binary black and white matrix plotted with a determined threshold value of 190. This value is much larger than would have been selected using the discussed methodology; however, it was chosen to capture the large open water features of the image.

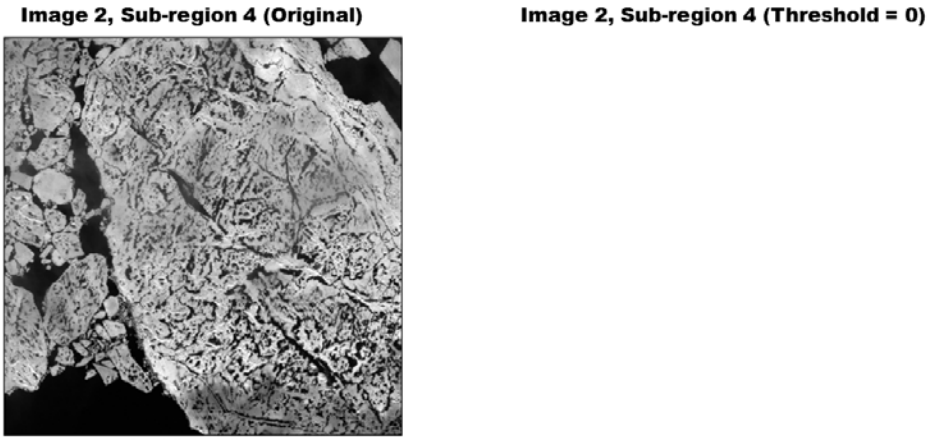

Figure 28. The original grayscale matrix for Image Two, Sub-region Four is seen on the left. On the right is the converted binary black and white matrix plotted with an automatically determined threshold value of zero. The total white color indicates the thresholding program determined the entire image is comprised of sea ice.

2. Meltpond Discrimination

For each thresholded image, an algorithm was written to determine the boundaries for open water, meltponds, and ice floes (Figure 29). While the majority of meltponds in the original thresholded image are visible, there are some areas identified as meltponds which visually are determined to be areas of open water, such as the three areas denoted by the red circles in Figure 29. Areas of open water are distinct features identifiable by their long lengths and larger closed surface areas when compared to the majority of the other meltpond features identified by the algorithm. To distinguish areas of open water from meltponds, histograms of the length of the major and minor axes were generated (Figure 30). For each sub-region, the outlying major and minor axes areas were filtered out. In this example, a major axis limit of 120 and a minor axis limit of 60 were applied, resulting in the meltpond identification seen in Figure 31. While this process may result in some larger meltponds being identified as open water, it is valid based on Hudson et al. (2013), were they found larger meltponds share similar albedo, absorption, and transmittance characteristics to open water.

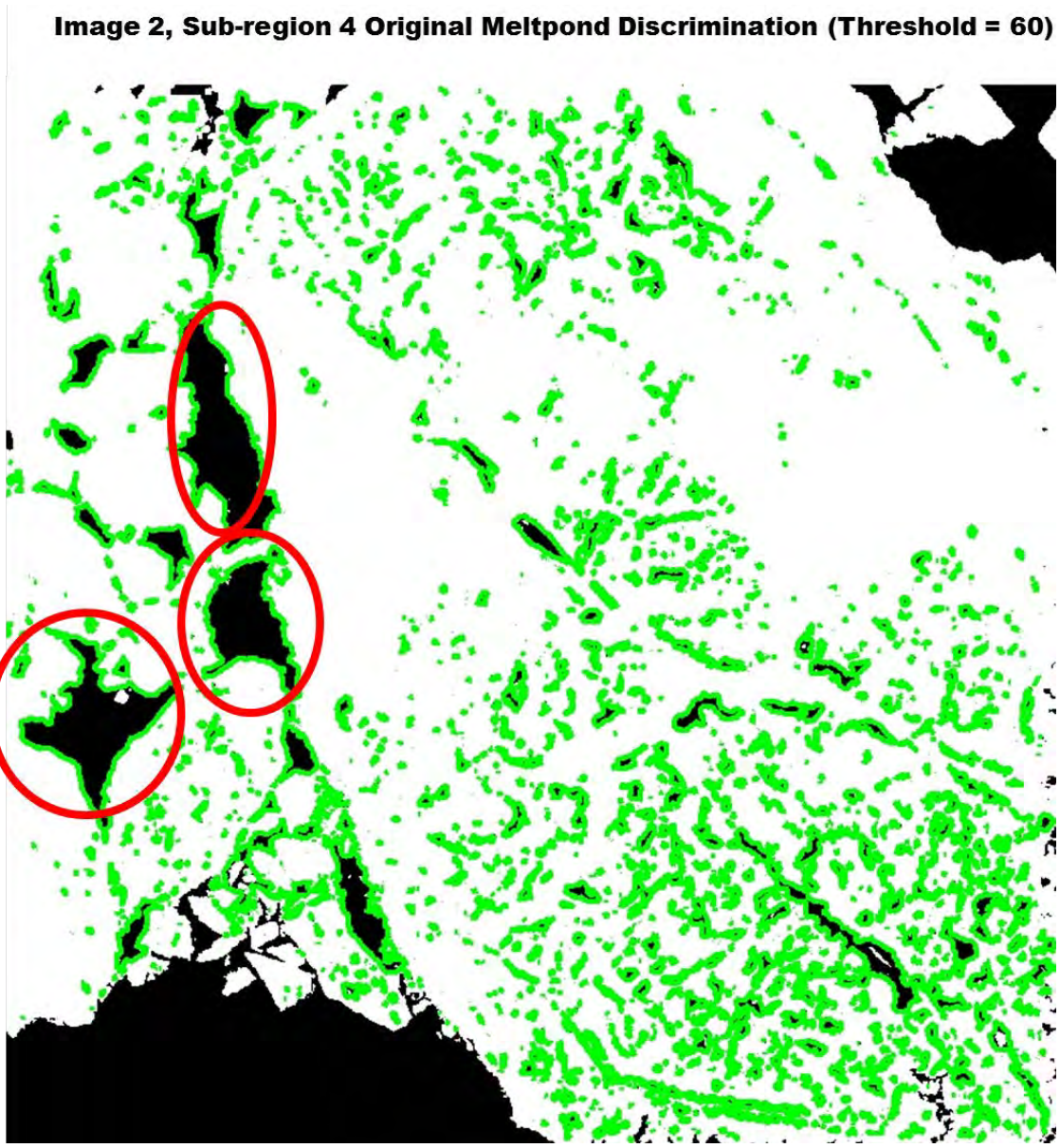

Figure 29. Image Two, Sub-region Four converted with an applied threshold of 60. Overlaid in green are the default meltponds. There are many large meltponds which based on a visual of the original satellite image are actually areas of open water which need to be discriminated. These areas are highlighted by the red circles.

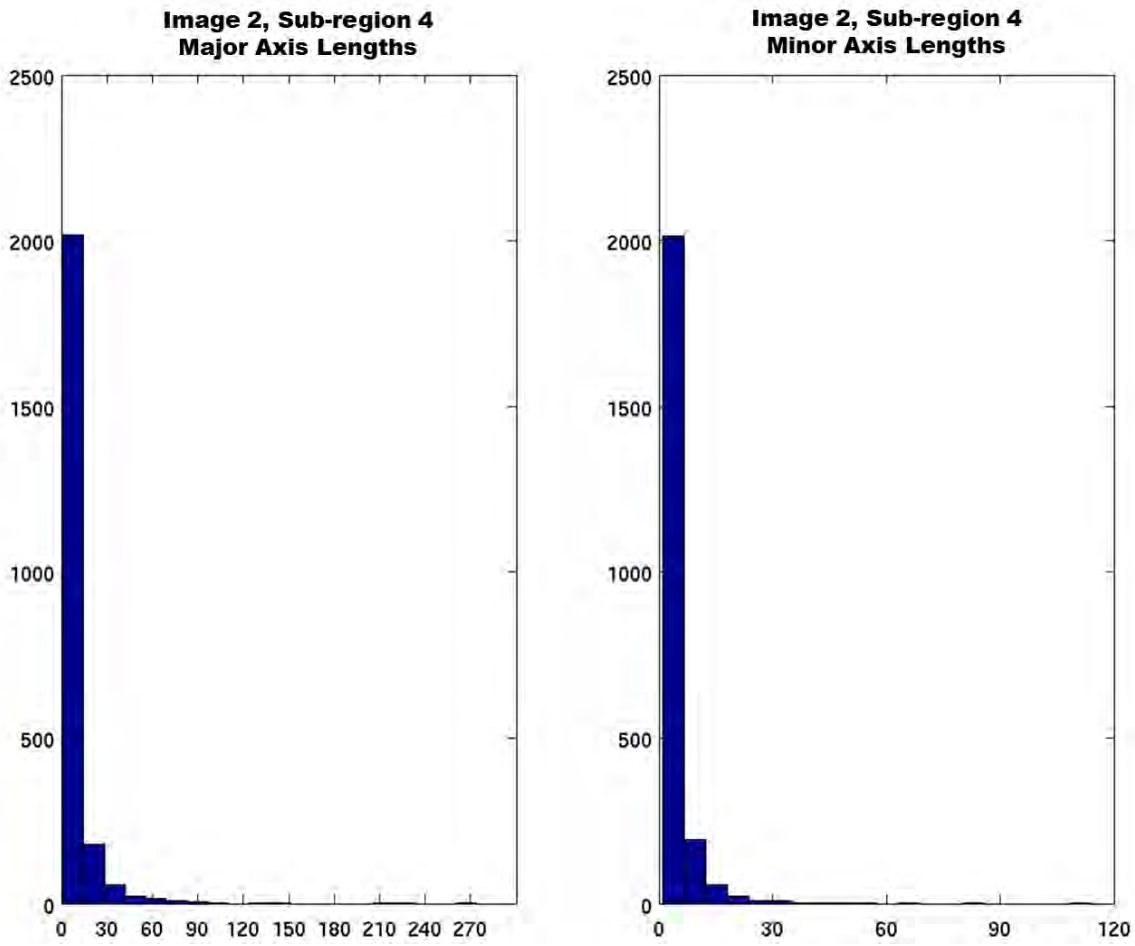

Figure 30. Histogram for the major and minor axis lengths for Image Two, Sub-region Four. Areas of open water incorrectly identified as meltponds are filtered out based on the values of their major and minor axes.

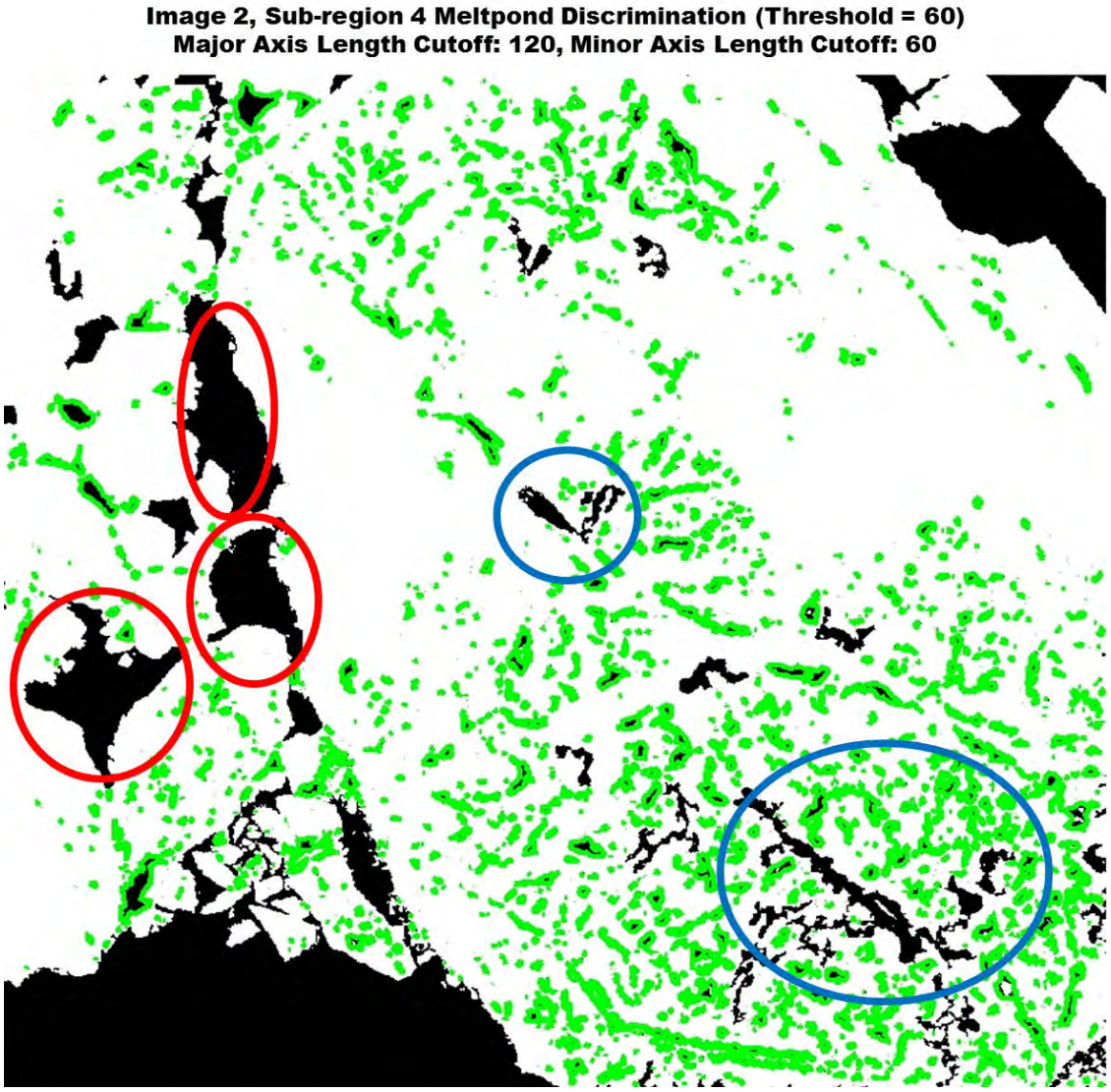

Figure 31. Image Two, Sub-region Four meltponds with an applied threshold of 60, major axis criteria of 120, and minor axis criteria of 60 applied. The regions originally identified in Figure 29 as meltponds are correctly identified as open water (red circles). Additionally, some of the larger meltponds (blue circles) are also identified as open water.

3. Open Water Fraction Determination

The final step in the image processing is to determine the open water, meltpond, and ice floe fraction for each sub-region. This was done in a pixel reference system vice an area reference. Since open water fraction is a ratio, this is an acceptable simplification. Each feature is defined by the total number of pixels contained in its closed loop. The total number of open water pixels was calculated using Equation (6). This value was then used in Equation (7) to determine the total open water fraction. This value was then converted to area by applying ratio provided in the image metadata.

$$\text{Open Water Pixels} = \sum \text{total pixels} - \sum \text{floe + meltpond pixels} \tag{6}$$

$$\text{Open Water Fraction} = \frac{\text{Open Water Pixels}}{\text{Total Pixels}} \tag{7}$$

D. BUOY DATA CORRECTION

Prior to determining and analyzing heat content data in context with satellite imagery, the AOFB and ITP data from correlating deployments must be corrected in order to make comparative analysis from the two different sensors. The raw temperature and salinity measurements from the AOFB and the top bin level of the matching ITP data were loaded into MATLAB. ITP measurements from both down-profiles and up-profiles are included in the data set. Conductivity was calculated from salinity using a custom MATLAB routine. Since both instruments are measuring conductivity in the water column and using this property to determine salinity, it was chosen as a true measurement of data correction. For each group time series, an isothermal event was chosen, i.e. the minimal difference between the AOFB and ITP temperature measurement for a profile. The corresponding difference between the conductivity measurements at the same time was then identified. In every case, the AOFB conductivity was lower than the ITP conductivity, thus the determined temperature and conductivity offsets were added to the AOFB data sets. For both the AOFB and ITP data, salinity was then recalculated. The corrected data was then used for further analysis. An illustration of the data offset correction process is presented in Figure 32.

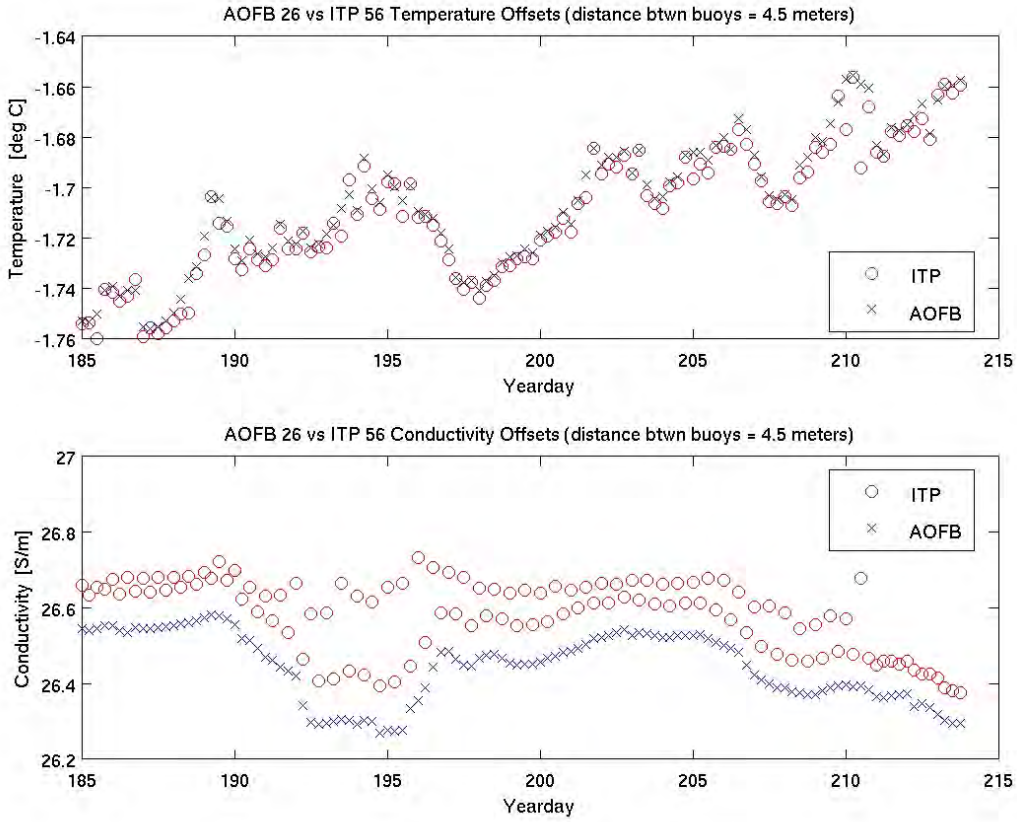

Figure 32. Example of raw AOFB and ITP temperature and conductivity time series. The temperature measurements match well, but the calculated conductivity measurements differ slightly. Also, the "up-profile" and "down-profile" nature of the CTD data from the ITP which needed to be corrected can be seen.

III. DATA ANALYSIS AND RESULTS

This data analysis focuses on studying the effects of solar heating through local open water regions near the AOFB sensors as the ice drifts over the ocean in response to wind forcing. Four groups of data are presented, three processed from observations collected in the Beaufort Sea and the final group of data from the Transpolar Drift. The mean temperature and heat content of the ocean mixed layer just below the ice are calculated from the ice-deployed sensors to quantify the solar heating of the upper ocean. For each image, the total open water fraction, departure from freezing, and surface mixed layer melting heat content was calculated for a 24 hour period centered on the previously determined image capture time. Temperature, salinity, and density plots are auto-scaled to reflect changes in the local upper water column; all other plots presented are scaled the same to allow for trend comparison between the four groups. Yearday values greater than 365 indicate the data set is from buoy deployments spanning multiple years.

The conceptual approach of this method is depicted in Figure 33. For this analysis of solar heat entering open water areas, we assume the ocean to be at rest for a period of 12 hours before and after the image capture time. Areas of open ocean or deep meltponds allow solar radiation to enter the ocean and be absorbed and stored in the upper part of the IOBL. As the ice-supported sensors drift over the ocean in response to wind forcing, the IOBL develops shear-induced turbulence down from the ice interface, mixing the stored heat up to the ocean-ice interface, potentially resulting in significant ice melt.

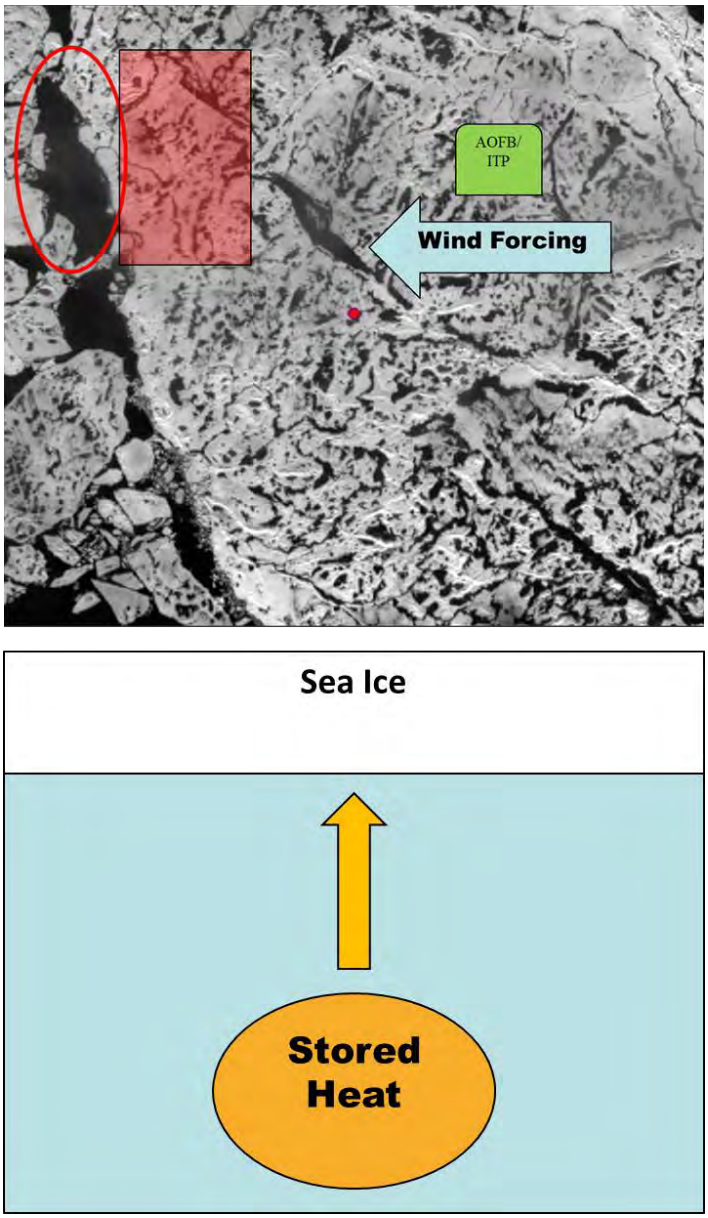

Figure 33. Schematic illustrating the conceptual approach used in this thesis. Top Image: heat enters the IOBL via open water leads (red circle). Wind forcing induces ice movement over an assumed static ocean, storing the heat under the ice in the path ahead of the ice-supported sensors (shaded red area). Bottom Image: stored heat is transported vertically due to ice-induced shear turbulence. This heat is then available to cause basal ice melt.

A. CHOOSING A REFERENCE LAYER

In order to compare IOBL heat content from each of the image groups, a lower reference depth for the surface mixed layer had to be identified. The strong seasonal halocline effectively decouples the IOBL thermodynamically from the rest of the water column (Shaw et al. 2009, McPhee 2008), so we seek a consistent IOBL slab depth for heat content calculations. The depth of the reference layer was determined by plotting the upper 200 meter vertical profiles of temperature, salinity, and density from the ITP deployed next to the AOFB for each of the images (Figure 34). The strong vertical gradient associated with the Arctic halocline that primarily determines the density is clearly identifiable. For each of the time intervals (see Chapter III.C) the mean depth of the observed vertical gradient was at 22.3 meters to 45.7 meters. A conservative estimate of the highest mixed layer base depth was taken as 20 meters, and is used throughout the following analysis to provide a consistent lower depth limit for the heat content calculations. The upper limit reference depth, the bottom of the sea ice, was chosen to be two meters.

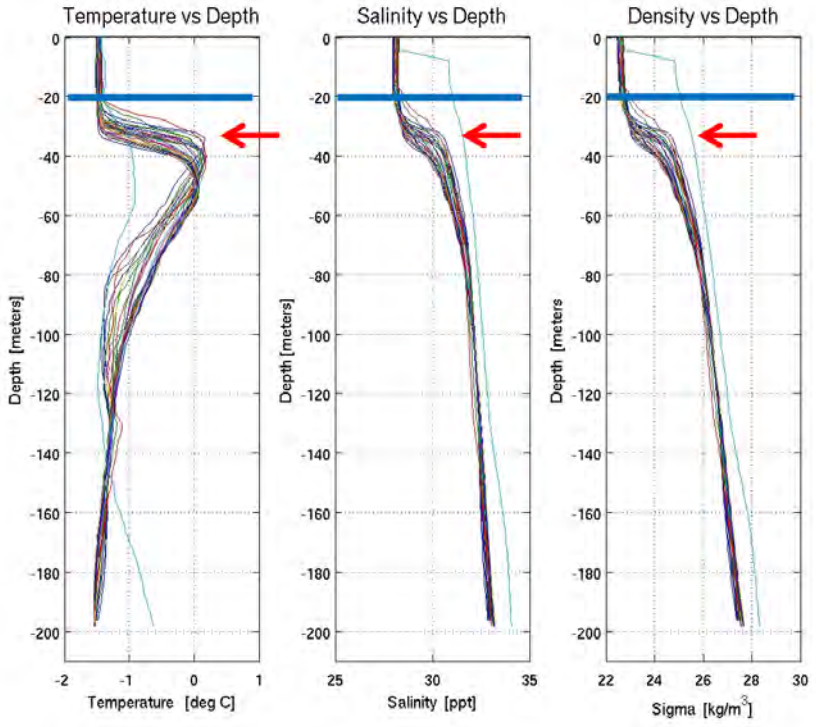

Figure 34. Example of the vertical profiles of temperature, salinity, and density. The vertical gradient associated with the Arctic halocline is indicated by the red arrows. The lower reference layer chosen to be used for analysis throughout this thesis is illustrated by the thick blue line.

B. CALCULATING HEAT CONTENT

In order to estimate the amount of heat in the IOBL available for melting ice, the heat content relative to the in-situ freezing point was calculated for the surface layer. For each ITP CTD profile, the in-situ freezing point of seawater as a function of salinity and pressure was calculated. This value was then used to calculate the departure of freezing at each depth for the profile using Equation (8) (Shaw et al. 2009). This difference from in-situ temperature to in-situ freezing point is the thermodynamically relevant temperature when considering ice melting or ice formation at the ocean-ice interface (Stanton et al. 2012). Positive values indicate that the in-situ temperature is warmer than the ice freezing point and will cause melting, while negative values indicate super-cooled conditions, were water is present in its liquid form below what the freezing point is for a given salinity and depth and will result in ice formation at the ocean-ice interface. The

departure from freezing was then used to calculate the surface mixed layer melt heat content of the water column using Equation (9) (Stanton et al. 2012). Vertical heat content profiles are calculated similarly without integrating over the entire vertical water column. The specific heat capacity of water, c_p, and the water density, ρ, were taken as $4000\ J\ kg^{-1}\ C^{-1}$ (McPhee 2008) and $1024\ kg\ m^{-3}$ (based on the in-situ density from the CTD), respectively. The ITP data were binned to two meters (Δz).

$$Departure\ From\ Freezing\ =\ Temperature_{In-Situ} - Temperature_{Freeze\ Point} \tag{8}$$

$$Surface\ Mixed\ Layer\ Melting\ Heat\ Content\ =\ \int_{Ref\ Layer}^{Ice\ Depth} (Temperature_{DFF}) * c_p \rho\ \Delta z \tag{9}$$

To illustrate the importance and effect of the strong stratification between the IOBL and the rest of the vertical water column in the Arctic Ocean, the heat content from 0 – 200 meters was calculated (Figure 35). The surface mixed layer (0 ~ 30 meters) is much cooler than the rest of the water column, as it is in contact with the ice cover. At this location, the upper pycnocline, between 30 ~ 60 meters, contains most of the heat, while the rest of the depth of the water column is cooler than the stronger density gradient slab, but still warmer than the IOBL, which remains thermodynamically coupled to the ice cover. This calculated heat content matches well to typical water column layers associated with the Beaufort Sea calculated by Shaw et al. (2009). In the study, they summarized that while there are high levels of heat in the halocline and the warm Atlantic and Pacific layers below, the heat contained in these layers is typically unavailable to contribute to basal ice melting due to the strong stratification and very low turbulent diffusivities of the upper pycnocline in the Beaufort Sea.

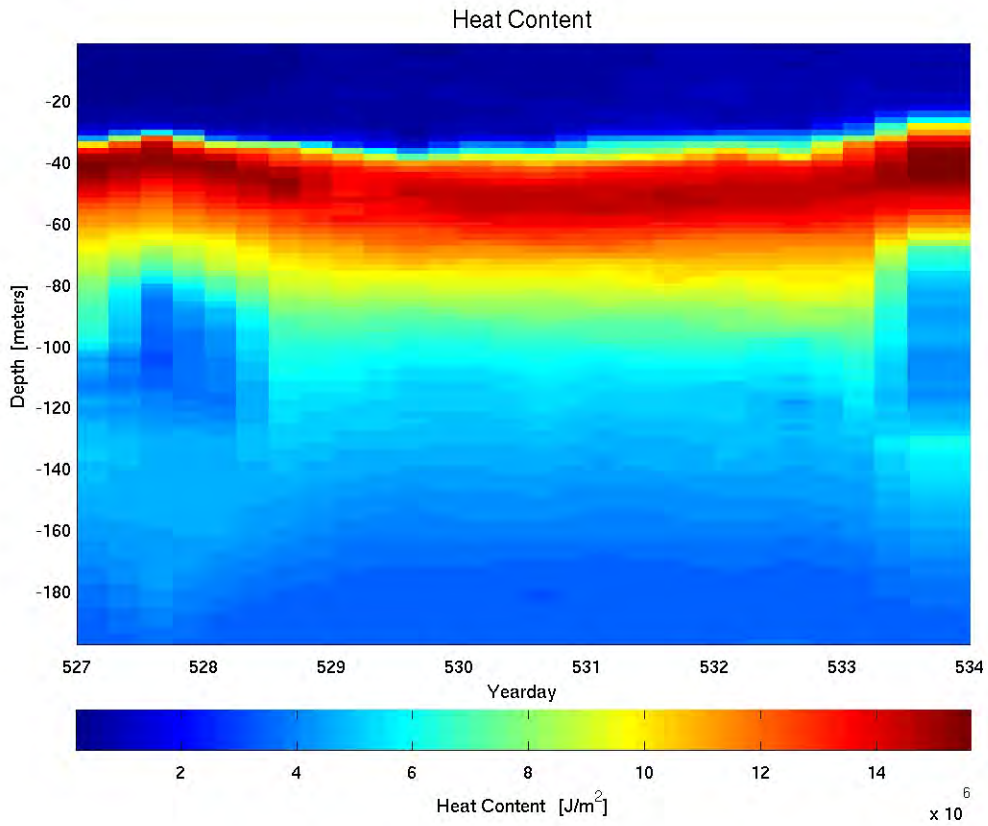

Figure 35. Vertical heat content profile from the surface to 200 meters in the Arctic Ocean. A strong halocline and warm Atlantic water can be seen, both of which are decoupled from the surface mixed layer.

C. DATA RESULTS AND DISCUSSION

Table 5 summarizes the seven images selected for further analysis. Groups One and Two utilize binned, calibrated CTD profiles from the ITPs, vs. single depth conductivity/temperature time series used to analyze Groups Three and Four, as the full profile data is not yet available. Groups One through Three utilize observations from the Beaufort Sea. Group Four results are from a series of images and sensor measurements from the Transpolar Drift. For the satellite imagery provided in this section, it is important to remember that the blue sub-regions described in Chapter II do not represent AOFB movement independent of the ice pack, rather, the entire ice pack moves along the trajectories indicated. The sub-regions highlight the surface ice features that determine the pre-conditioning of the IOBL that the ice-supported sensors measure.

Group Number	Image Hit Index	Corresponding AOFB	Corresponding ITP	Image Date	Calculated Image Time
1	1	25	54	6-Jun-12	0500
1	2	25	54	21-Jun-12	2300
2	22	24	65	6-Jun-13	2330
3	26	27	66	7-Aug-13	2330
4	13	26	56	11-Jul-12	1145
4	15	26	56	20-Jul-12	0115
4	27	26	56	28-Jul-12	1530

Table 5. Results group summary. Results groups were determined by correlating satellite imagery, AOFB, and ITP data sets. Groups One through Three are data and observations from the Beaufort Sea; Group Four is data and observations from the Transpolar Drift.

1. Group One

Group One contains two satellite images from the Beaufort Sea in early and mid-June 2012. Image One, taken on 6 June (yearday 522), can be seen in Figure 36. Large, compact ice floes are present, separated by jagged and distinct cracks and leads. Little open water exists in the regions between floes and few deep meltponds are discernable. The only significant open water along the AOFB trajectory is located in the region at the time the image was taken (indicated by the yellow shaded box). The ice conditions seen suggest that seasonal MIZ has not fully developed in the Beaufort Sea yet, nor have the ice floes been subject to significant wind forcing. Image Two (Figure 37) was taken 16 days later on 22 June (yearday 538). Although part of the image is degraded from the cloud cover, there are enough breaks in the clouds to conduct meaningful analysis of the ice surface conditions along the AOFB trajectory. Since the time of Image One, significant ice-opening events (i.e., ice divergence events) have taken place, resulting in a more open ice cover. Large areas of open water have developed in the ice cover and the meltpond count and area has visibly increased. The pancake floes that are visible indicate that the ice has been acted upon by wind forcing which causes floe-floe interaction. This image is likely reflective of the rapid and early summer development of the MIZ in the Beaufort Sea.

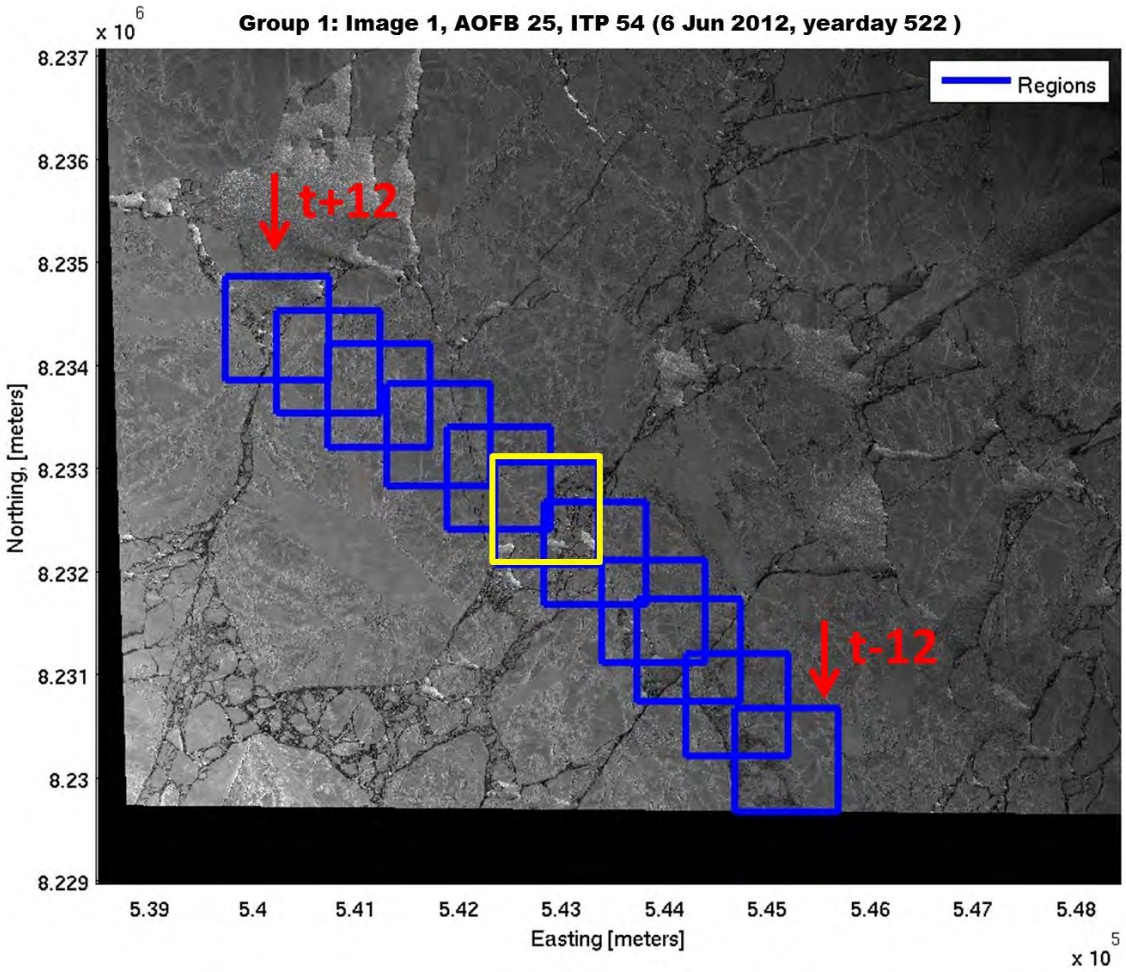

Figure 36. Zoomed in view of Image One in Group One. The sub-region the AOFB was located in at the time of image capture is shaded in yellow. Blue sub-regions show the ice pack trajectory +/-12 hours from the image capture time, as indicated by the red arrows.

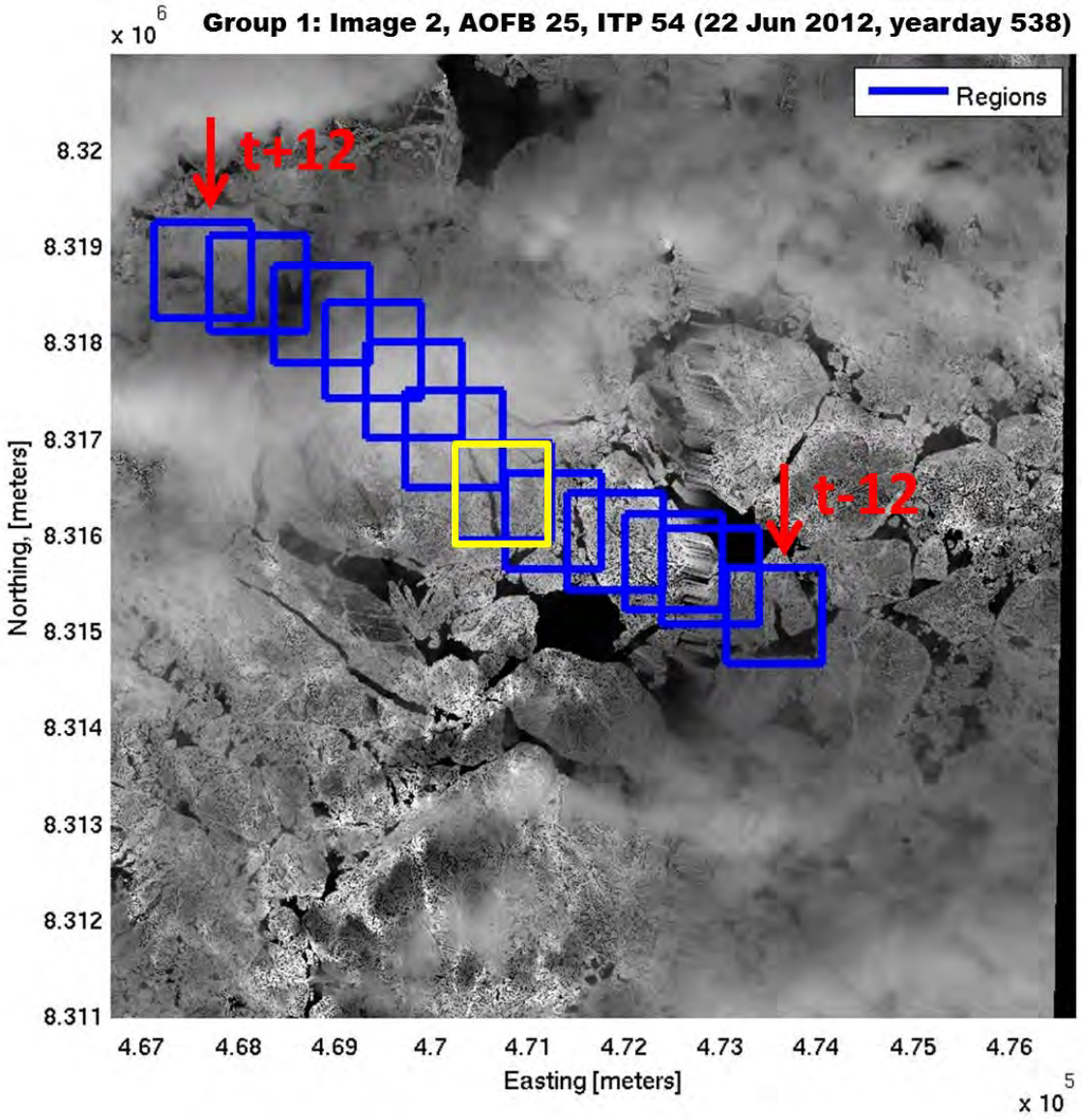

Figure 37. Zoomed in view of Image Two in Group One. The sub-region the AOFB was located in at the time of image capture is shaded in yellow. Blue sub-regions show the ice pack trajectory +/-12 hours from the image capture time, as indicated by the red arrows.

Image One statistics are presented in Figure 38. The total open water fraction 12 hours prior to the image capture time is low (maximum value 0.11) and decreases to 0.05 24 hours later. The departure from freezing and heat content increases slightly over the time series, with a broad peak between yearday 522 and 522.2; which follows closely with the open water fraction peak over the same interval. This corresponds well with the

visual ice conditions noted previously. Image Two statistics reflect the wide variety of open water features seen in the imagery (Figure 39). As expected from the observed visual increase in open water, there is a large increase in magnitude (max .39) and variation in the open water fraction, which is a reflection of the wide variety of open water features seen in the imagery. For this image, the departure from freezing is more uniform with a higher magnitude than Image One. This trend is also observed in the higher heat content values for Image Two.

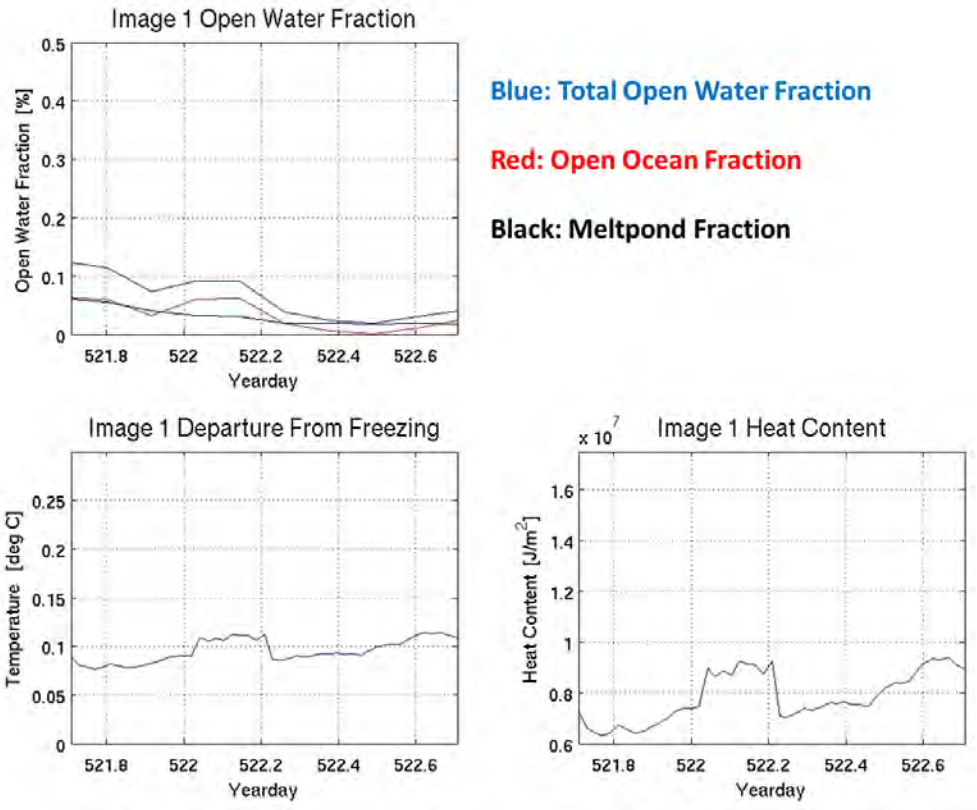

Figure 38. Image One (Group One) open water fraction, departure from freezing, and vertically integrated heat content time series.

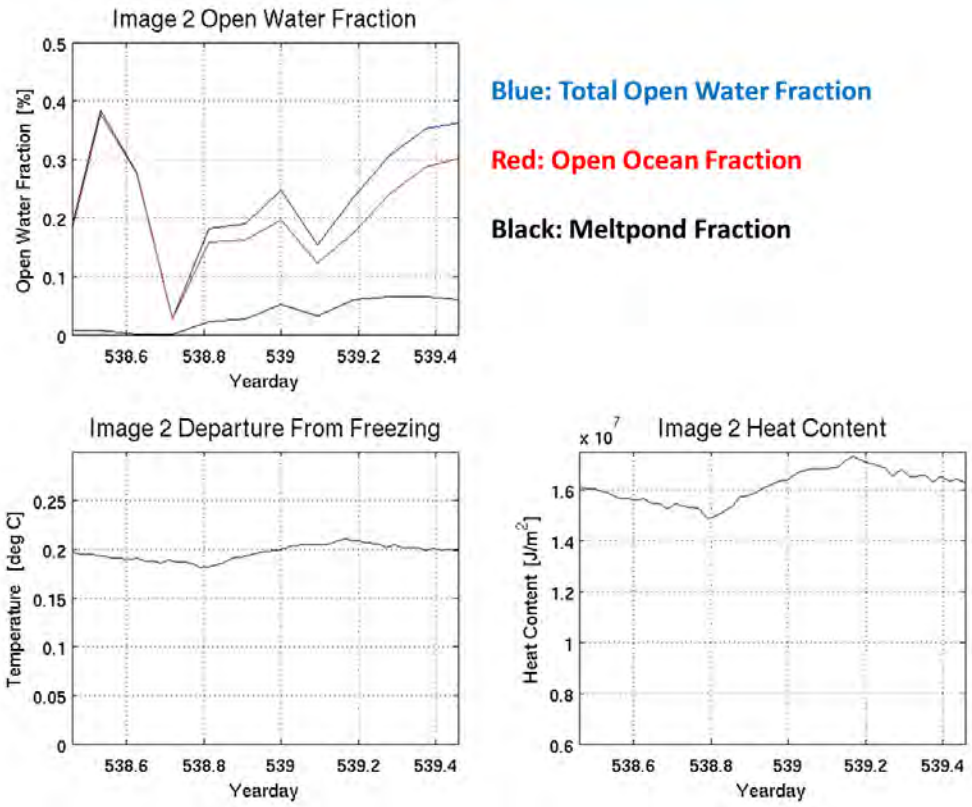

Figure 39. Image Two (Group One) open water fraction, departure from freezing, and vertically integrated heat content time series.

Temperature, salinity, density, and departure from freezing vertical profiles are presented in Figure 40. Evident in all the time series is a clear distinction between periods with little open water fraction and ice cover (Image One) and periods with significantly more open water fraction and deep meltponds (Image Two). In Image One, the cold temperatures and expected higher salinity values are representative of the high concentration of sea ice and little open water. The small amount of solar radiation input into the IOBL is reflected in the small departure from freezing values (approximately 0.1) around yearday 522. In stark contrast, Image Two shows higher upper ocean temperatures and the expected decrease in salinity. More importantly, the departure from freezing value nearly doubles around yearday 530, increasing to as high as 0.35. As expected, the heat content, driven by the departure from freezing, increases significantly from Image One to Image Two (Figure 41).

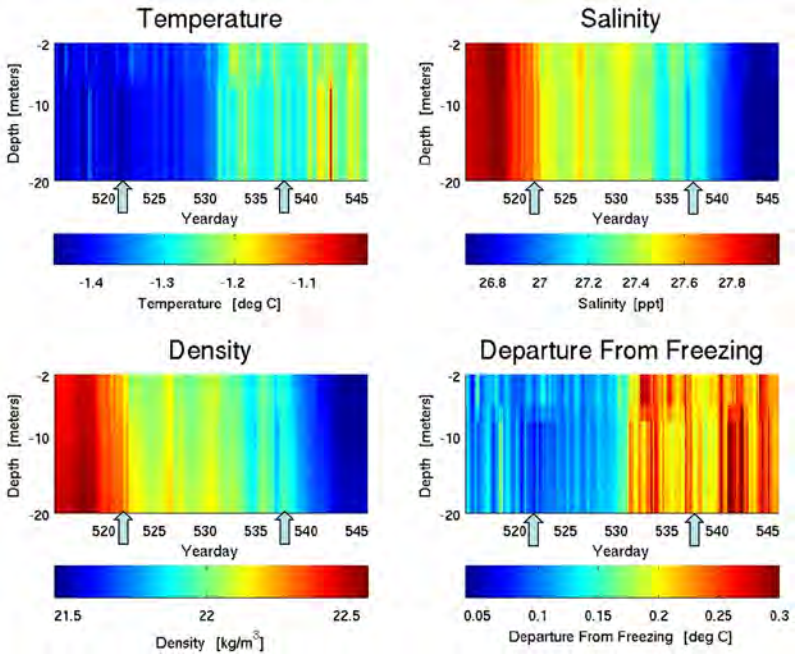

Figure 40. Vertical profiles of temperature, salinity, density and calculated departure from freezing values for Group One. Yeardays corresponding to available satellite imagery are marked by the blue arrows along the x-axis.

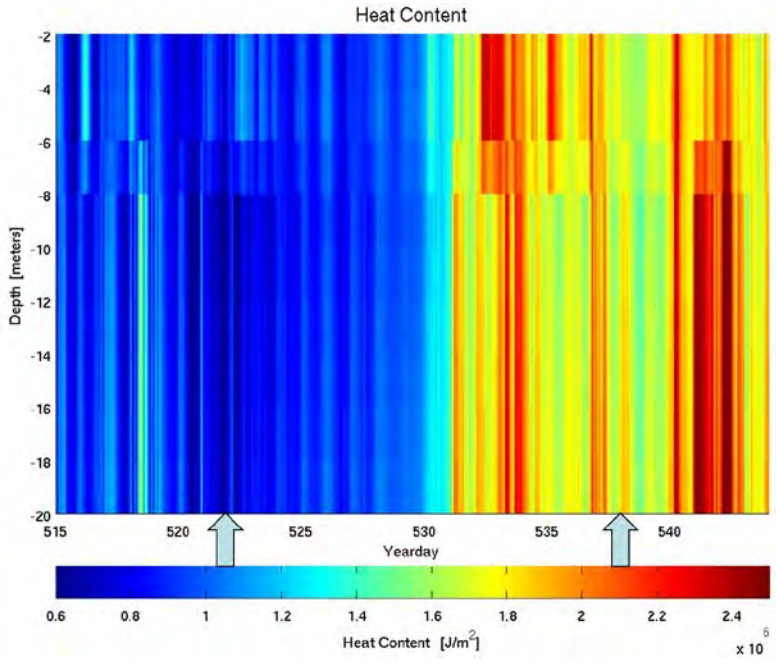

Figure 41. Vertical profile of melt heat content for Group One. Yeardays corresponding to available satellite imagery are marked by the blue arrows along the x-axis.

2. Group Two

Group Two contains one image (Image 22) from early June 2013 in the Beaufort Sea (Figure 42). This shows early summer conditions one year later from Group One imagery. As seen in early June the previous summer (Image One), Image 22 is characterized by the presence of a large, compact ice floe, the largest of any of the seven images available for this study. There is little open water in the sub-regions, but significant areas of open water just to the south of the AOFB trajectory. These features suggest that the influence of the seasonal MIZ in the Beaufort Sea as not yet taken full effect. This image is also degraded slightly by the presence of cloud cover, particularly in the upper portion of the image. To combat this, a higher threshold then would have been normally chosen was used to identify the areas of open water. The blue sub-regions indicate fairly rapid west-east linear motion of the AOFB with a mean drift speed of $0.35\ \mathrm{m\ s^{-1}}$.

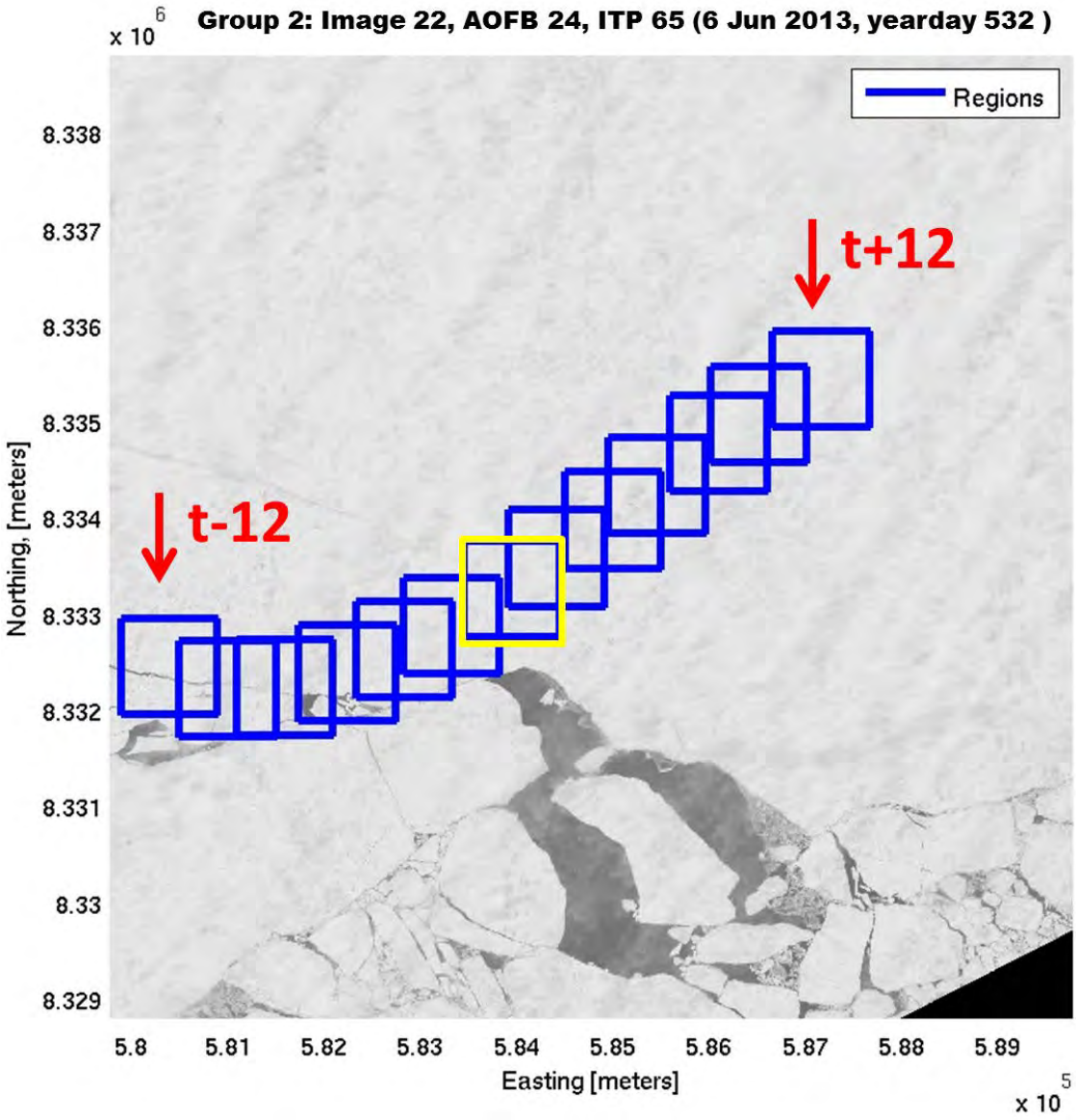

Figure 42. Zoomed in view of Image 22 in Group Two. The sub-region the AOFB was located in at the time of image capture is shaded in yellow. Blue sub-regions show the ice pack trajectory +/-12 hours from the image capture time, as indicated by the red arrows.

The corresponding statistics for Image 22 are presented in Figure 43. The total open water fraction is low, as expected, for this image, never reaching a value greater than 0.1 and dropping to nearly 0.0 over the latter portion of the time series, although the effect of cloud cover on the thresholding must be remembered. The departure from freezing has a slight positive slope over the interval, while the vertically integrated heat

content has a much more noticeable increase, peaking at yearday 533 before beginning a slight decrease for the remainder of the interval.

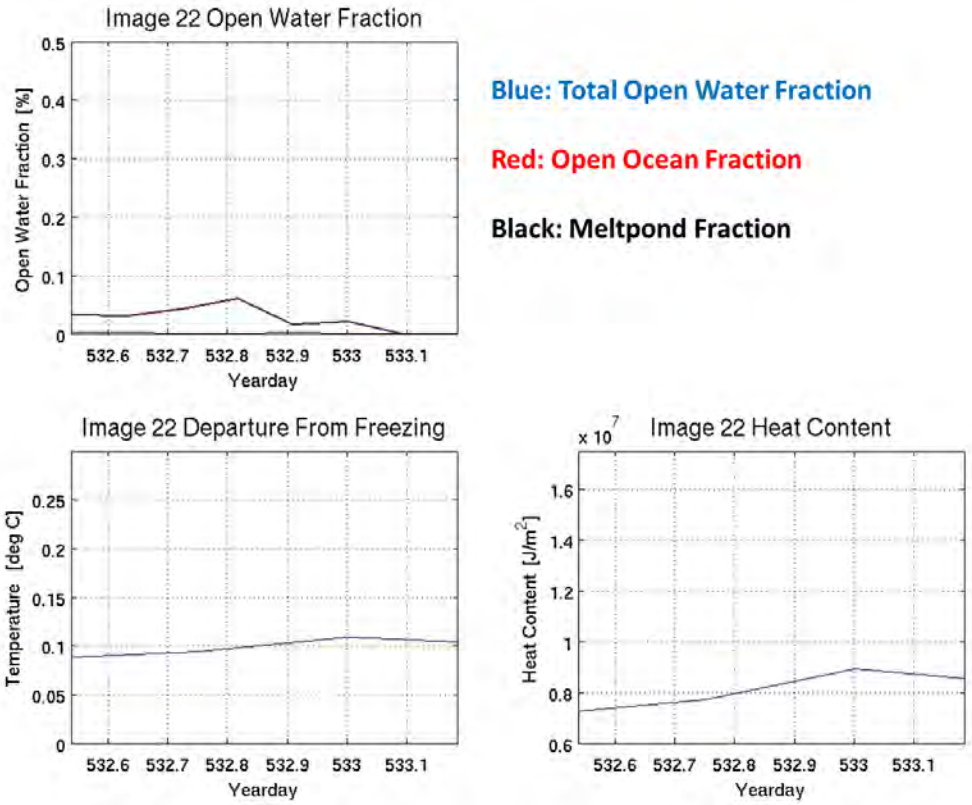

Figure 43. Image 22 (Group Two) open water fraction, departure from freezing, and vertically integrated heat content time series.

Image 22 temperature, salinity, density, and departure from freezing vertical profiles can be seen in Figure 44. Early in the time series, the temperature is cold and the water column is relatively salty. In the middle of the time series, the temperature begins to increase, however, the corresponding departure from freezing is small around yeardays 529-531. It is not until the end of the of time series that a significant increase in the departure from freezing is seen, beginning at approximately yearday 532. In this case, the departure from freezing increase at yearday 532 is a smaller and more isolated event then observed in Group One. Heat content from two meters to 20 meters is provided in Figure 45. The heat content follows closely with the departure from freezing, with a small and relatively isolated increase observable beginning at yearday 532.

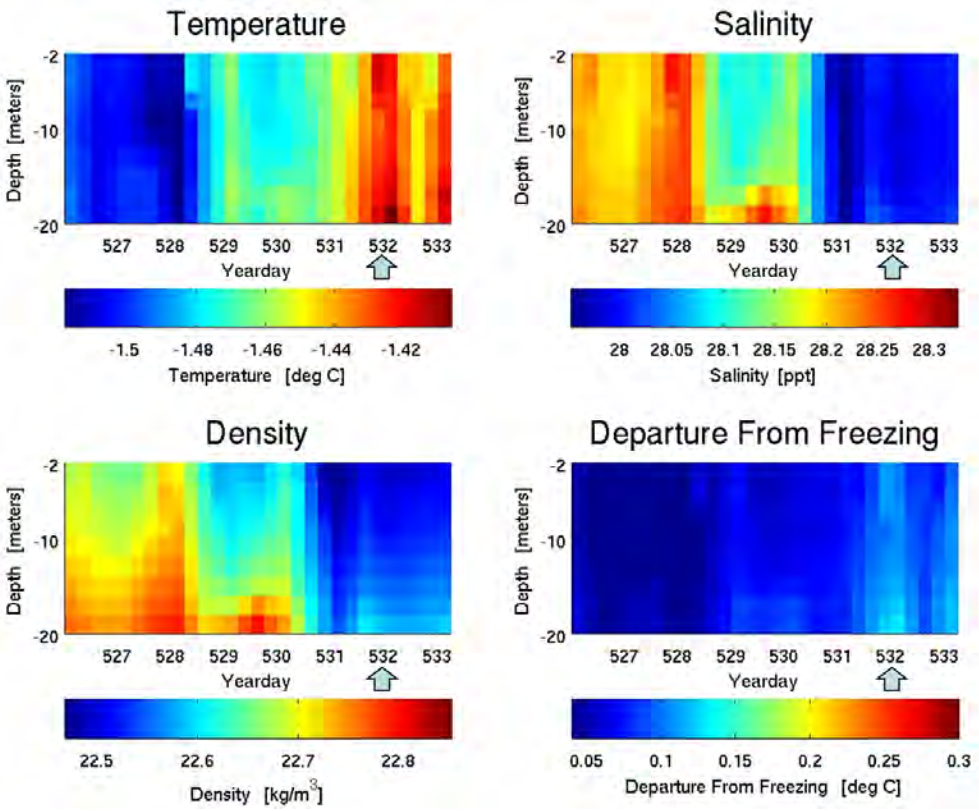

Figure 44. Vertical profiles of temperature, salinity, density and calculated departure from freezing values for Group Two. Yeardays corresponding to available satellite imagery are marked by the blue arrows along the x-axis.

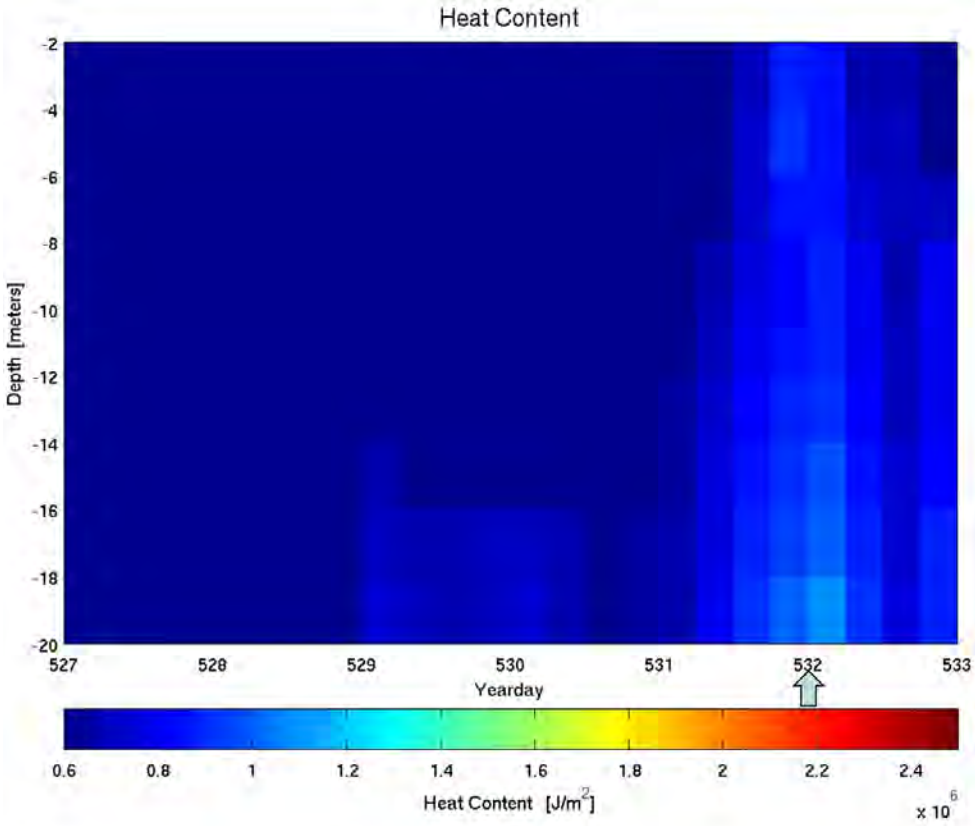

Figure 45. Vertical profile of melt heat content for Group Two. Yeardays corresponding to available satellite imagery are marked by the blue arrows along the x-axis.

3. Group Three

Group Three contains one satellite image from 07 August 2013 (yearday 584) (Figure 46). Image 26 shows the only snapshot of the late summer melt in the Beaufort Sea available in this study. Unique to this image is the clockwise trajectory of the AOFB with the ice pack, an indicator of inertial oscillation motion often seen in Arctic sea ice. This image shows the full effects of the seasonal MIZ are visible. Meltpond areal coverage is significant; many more darkened areas within the loose boundaries of ice floes indicate that the meltponds are quite deep compared to previous images. Dark gray color over the majority of the left portion of the image (when compared to the right hand side) is likely from increased snow and ice melt over the thinning ice floes. The ice floes visible are pancake floes, and no distinct cracks and leads are present, indicating the ice

floes have been interacting and colliding with each other from wind induced motion. The open water leads are greatest in this image, as well.

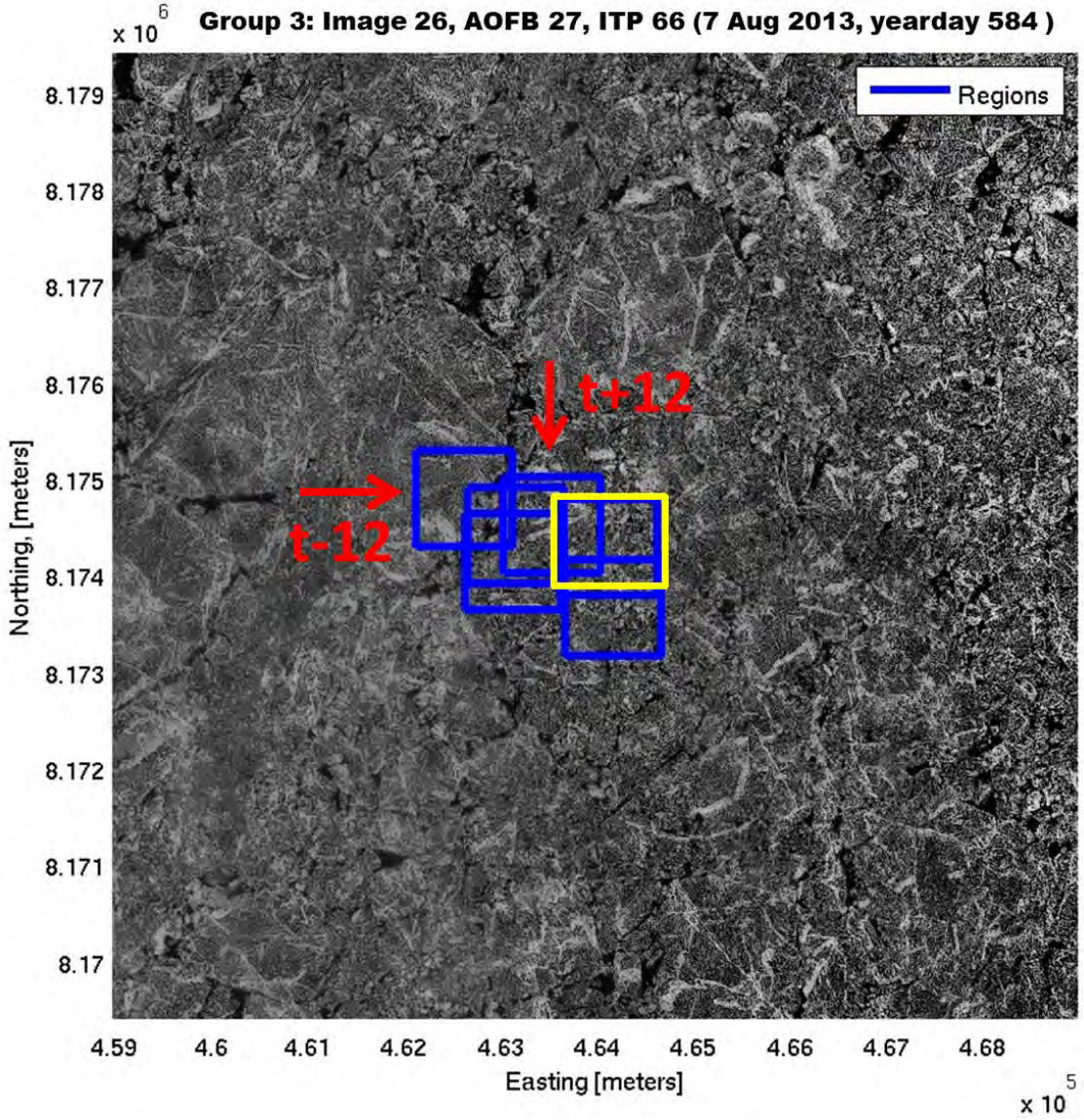

Figure 46. Zoomed in view of Image 26 in Group Three. The sub-region the AOFB was located in at the time of image capture is shaded in yellow. Blue sub-regions show the ice pack trajectory +/-12 hours from the image capture time, as indicated by the red arrows.

Image 26 statistics are representative of the visual surface ice conditions (Figure 47). The open water fraction is high. Interestingly, the meltpond fraction is low. This is

most likely the result of the thresholding technique determining the pixel values associated with the meltponds is similar to open ocean, indicating that the many of the meltponds have eroded significantly and melted through the ice floes on which they rest. This is echoed by the high departure from freezing values and high heat content values seen over the time series.

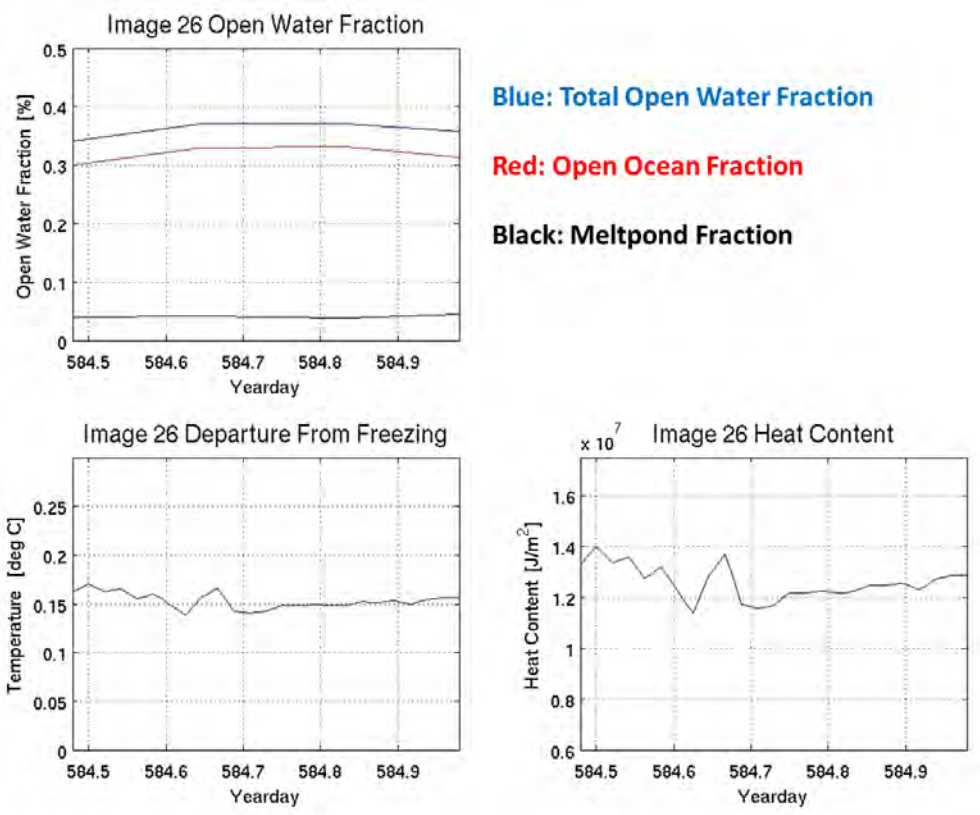

Figure 47. Image 26 (Group Three) open water fraction, departure from freezing, and heat content.

The late summer melt seen in Image 26 is also reflected in the IOBL vertical profiles seen in Figure 48. While the water column appears to be relatively cool in the early portion of the time series prior to image, there is a significant increase in the temperature beginning at the image capture time. More importantly, the departure from freezing, which is slightly elevated over the entire time series, increases as well at the onset of the image time. As indicated previously, the onset of the image interval also

brings a noticeable increase in the heat content (Figure 49), suggesting that the open water features seen in the image developed late in the season and are significant for controlling the heat input into the IOBL.

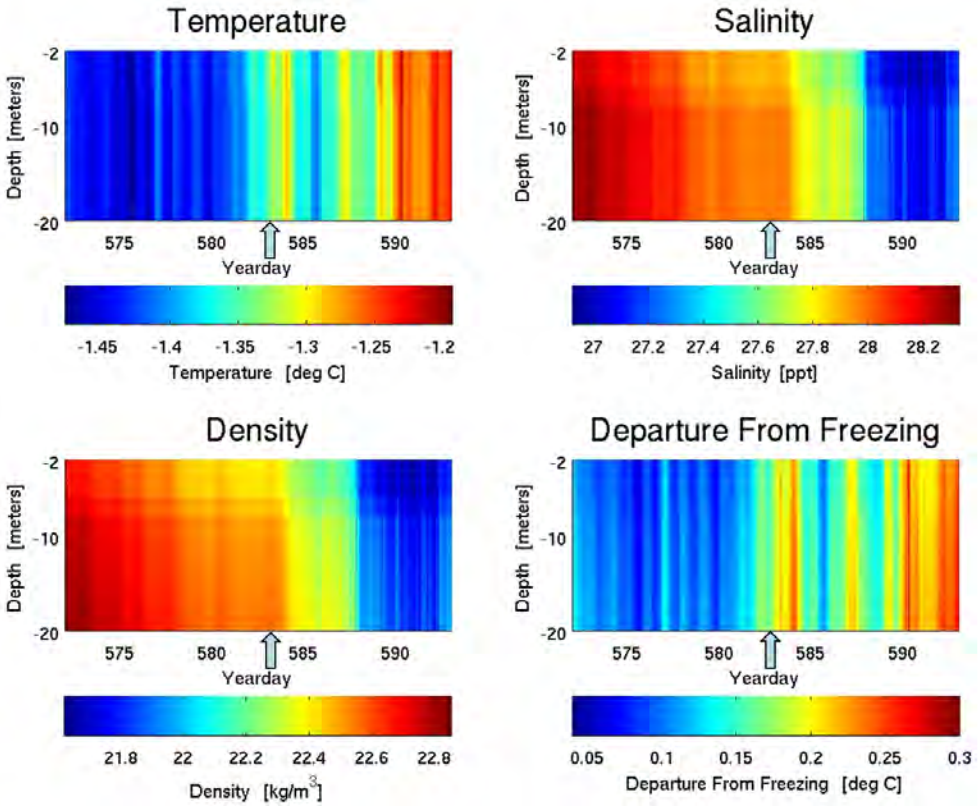

Figure 48. Vertical profiles of temperature, salinity, density and calculated departure from freezing values for Group Three. Yeardays corresponding to available satellite imagery are marked by the blue arrows along the x-axis.

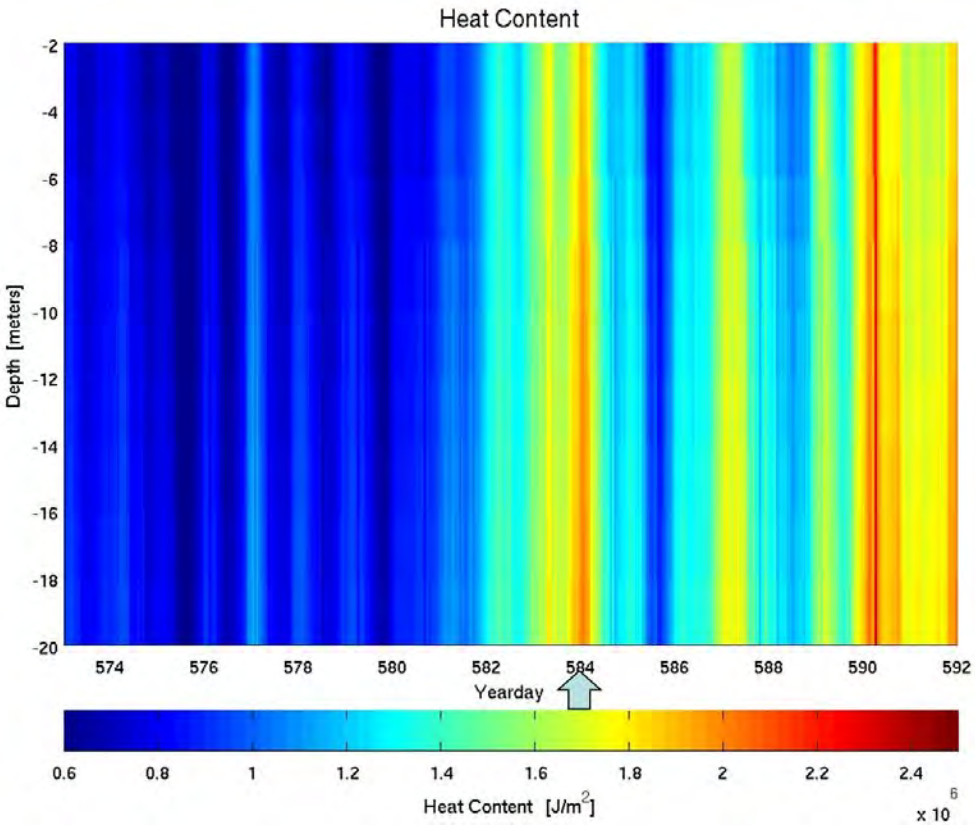

Figure 49. Vertical profile of melt heat content for Group Three. Yeardays corresponding to available satellite imagery are marked by the blue arrows along the x-axis.

4. Group Four

Group Four is the only set of data processed outside of the Beaufort Sea, and represents observations collected from the Transpolar Drift. This data set contains satellite imagery from three images (Images 13, 15, and 17) in a 30 day interval in July 2012. Image 13 (yearday 193) and its associated trajectory and sub-regions can be seen in Figure 50. In the full image, the ice has little open water between floes, especially along the trajectory path marked by the sub-regions. The only significant open water features present along the buoy track is the crack seen at the center of the region. In the vicinity of the crack is also the largest meltpond of the image, discerned by deep gray associated with cold water above frozen ice. Image 15 was taken nine days later on 20 July 2012 (yearday 202) (Figure 51). Here, the ice has undergone some transformation with more discernable open water features (black areas and open water leads) present and

an increase in meltpond area and coverage. The final image from Group Four is Image 17 from yearday 210 (Figure 52). Here, the ice has undergone further transformation, evident by the increase in the more rounded pancake like nature of the floes. Characteristics of this image include increased areas of open water as well as larger cracks, leads, and meltpond extent and count.

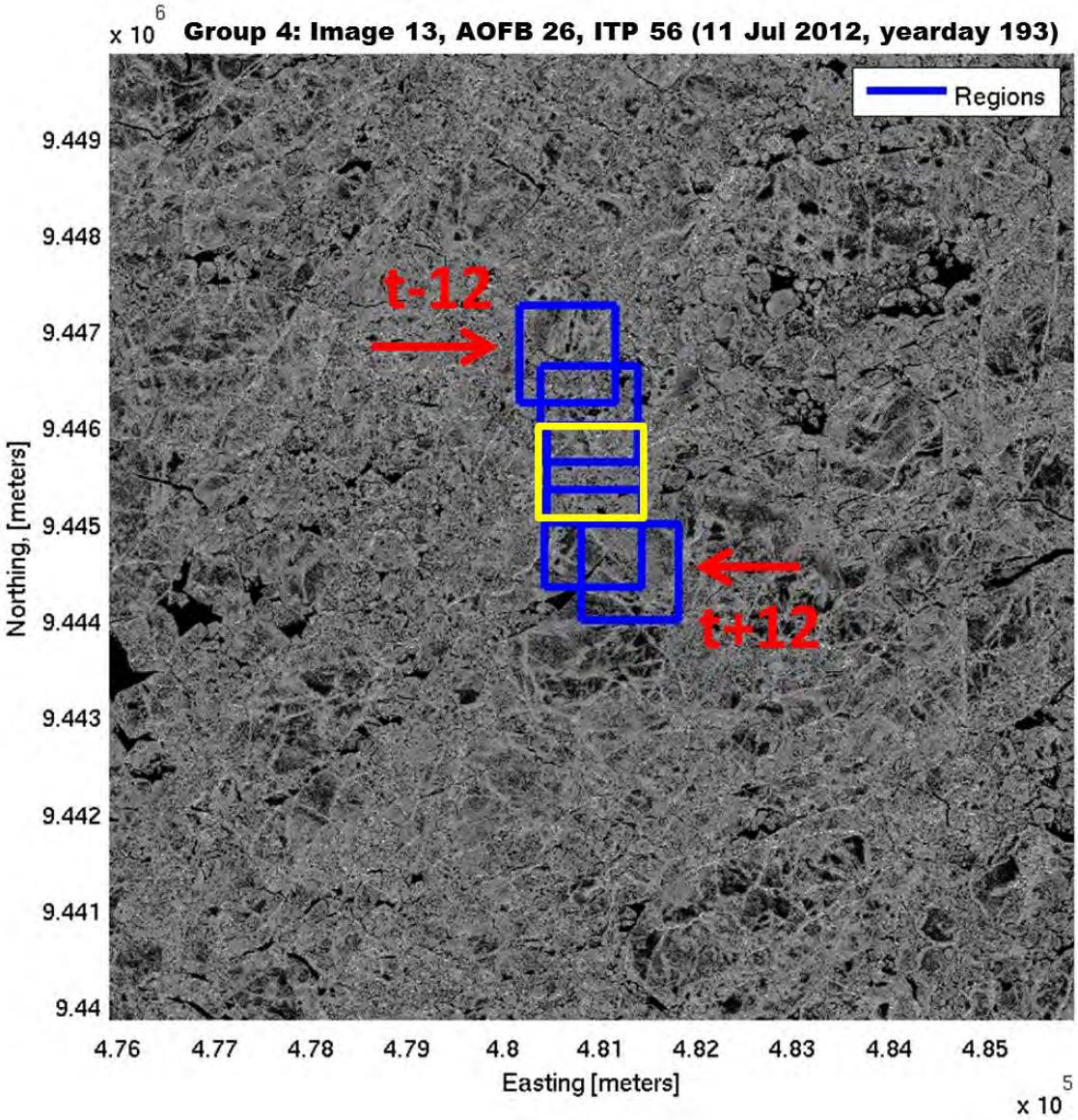

Figure 50. Zoomed in view of Image 13 in Group Four. The sub-region the AOFB was located in at the time of image capture is shaded in yellow. Blue sub-regions show the ice pack trajectory +/-12 hours from the image capture time, as indicated by the red arrows.

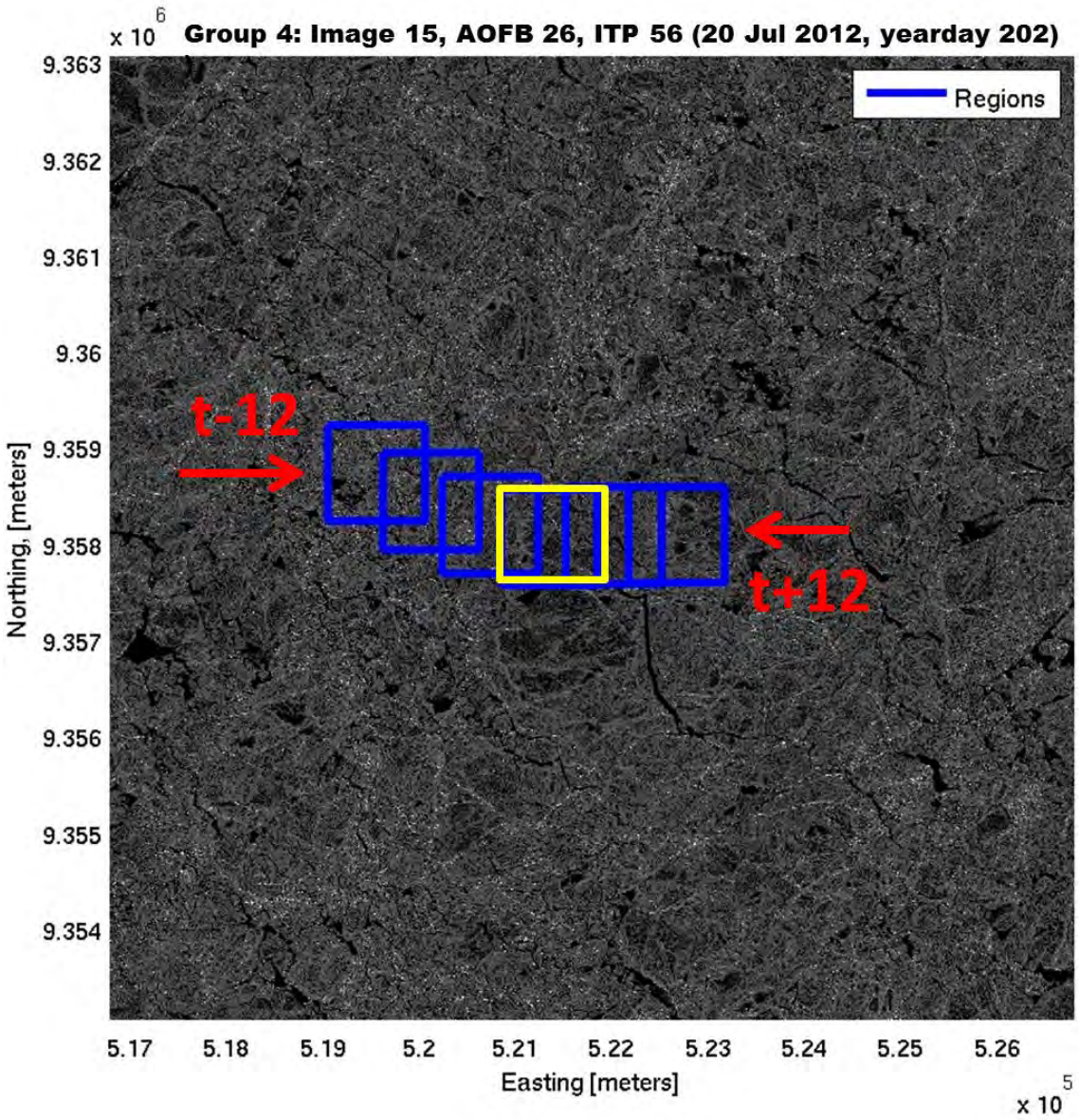

Figure 51. Zoomed in view of Image 15 in Group Four. The sub-region the AOFB was located in at the time of image capture is shaded in yellow. Blue sub-regions show the ice pack trajectory +/-12 hours from the image capture time, as indicated by the red arrows.

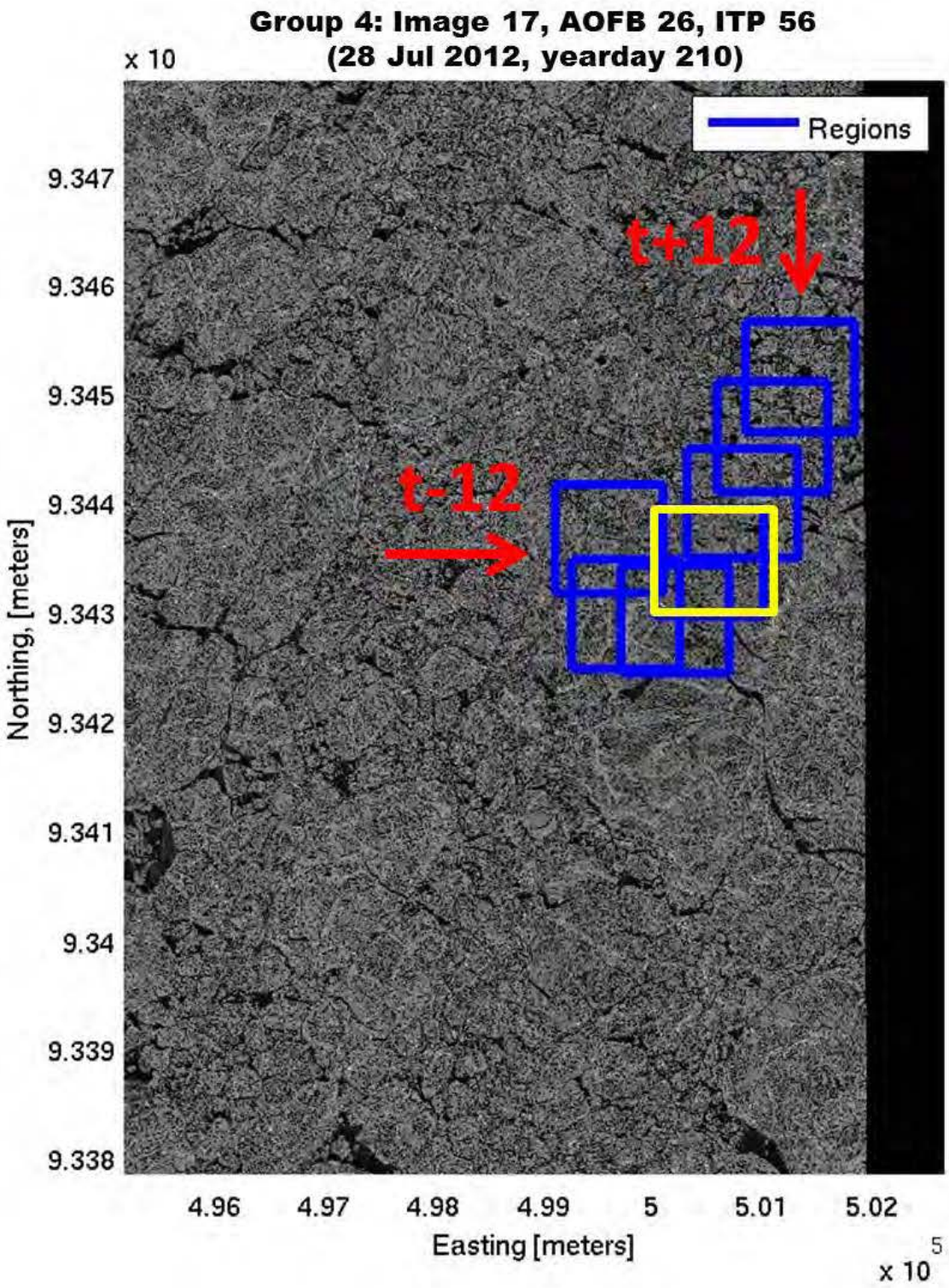

Figure 52. Zoomed in view of Image 17 in Group Four. The sub-region the AOFB was located in at the time of image capture is shaded in yellow. Blue sub-regions show the ice pack trajectory +/-12 hours from the image capture time, as indicated by the red arrows.

Image 13 specific statistics are presented in Figure 53. Overall, the total open water fraction increases from 0.20 to just less than 0.30, dominated by the trend of the open ocean fraction. Over the same interval, both the departure from freezing and vertically integrated heat content increase as well. Image 15 statistics can be seen in Figure 54. During this interval, the open water fraction has slightly increased to just over 0.30 from Image 13, and continues on an upward trend, maxing out at 0.40 before experiencing a slight decrease. The departure from freezing and heat content follow suit, as we see a slight increase with the increase of open water fraction followed by the decrease at the end of the interval. The final image of Group Four (Image 17) also shows an increase in the open water fraction of the ice trajectory interval (Figure 55). The departure from freezing and heat content, however, do not follow suit in this case, and decrease slightly over the same interval.

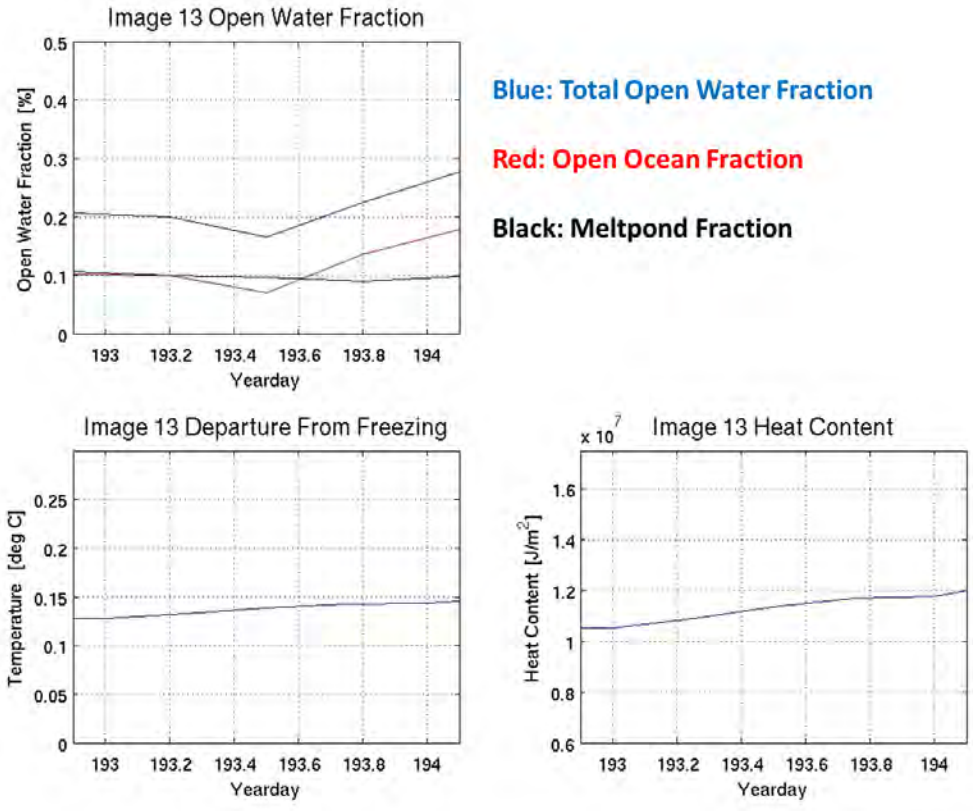

Figure 53. Image 13 (Group Four) open water fraction, departure from freezing, and heat content time series.

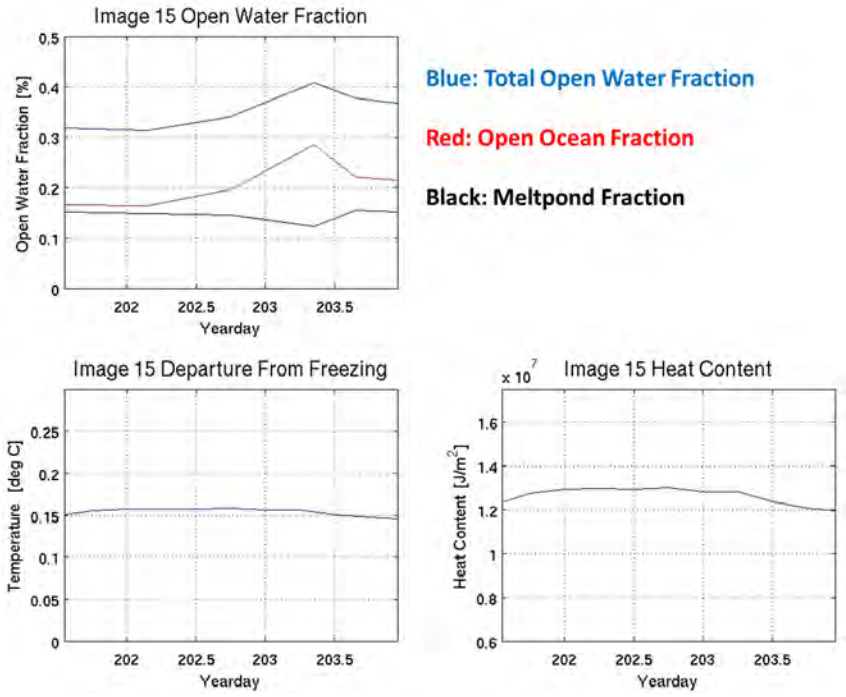

Figure 54. Image 15 (Group Four) open water fraction, departure from freezing, and heat content time series.

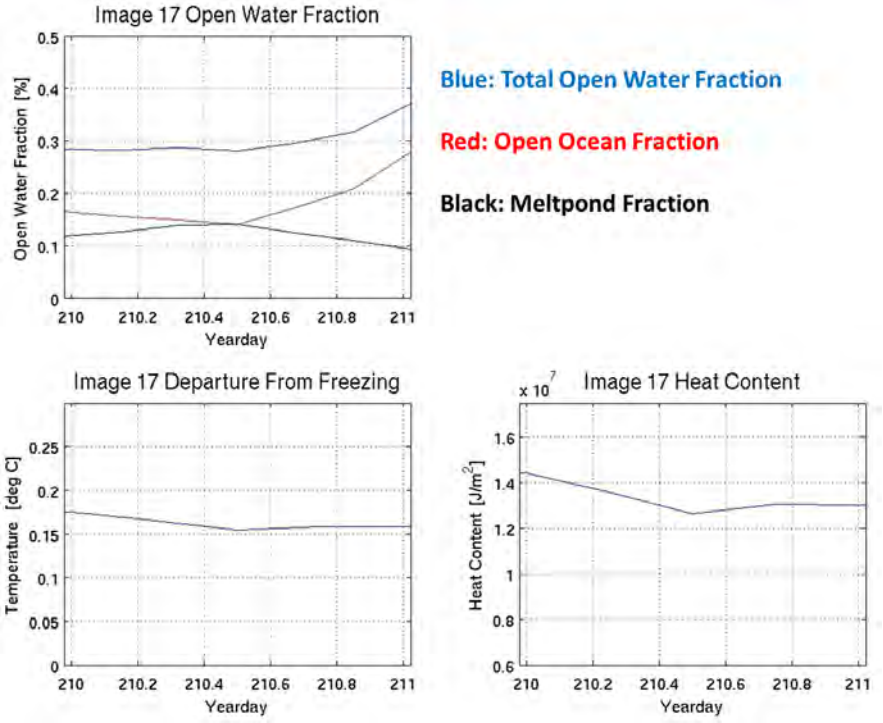

Figure 55. Image 17 (Group Four) open water fraction, departure from freezing, and vertically integrated heat content time series.

The vertical profiles of temperature, salinity, density, and departure from freezing in the IOBL, from two meters to 20 meters, for Group Four are presented in Figure 56. The vertical profiles are representative of the conditions from the Eastern Arctic basin. While the temperature remains relatively cool, the salinity values are much higher compared to those from the Beaufort Sea. The departure from freezing values is nearly uniform and consistently higher across the entire time series, in contrast to the trends seen earlier. The vertical profile of melt heat content in the IOBL can be seen in Figure 57. As expected, we see a similar positive trend across the time series as that of the departure from freezing.

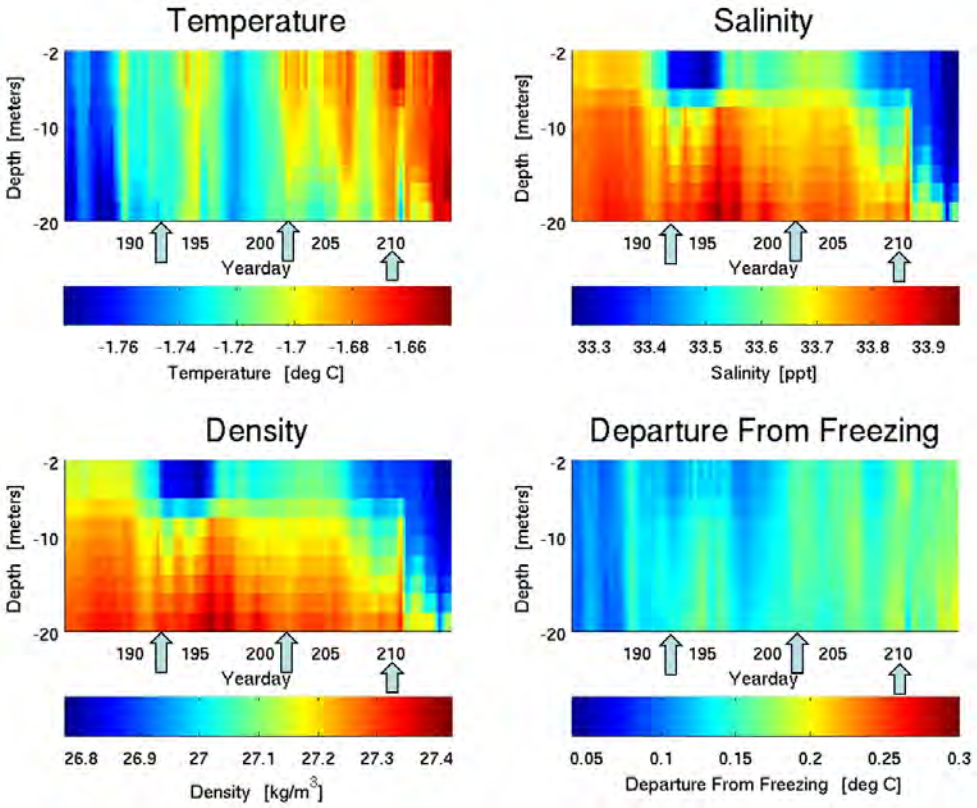

Figure 56. Vertical profiles of temperature, salinity, density and calculated departure from freezing values for Group Four. Yeardays corresponding to available satellite imagery are marked by the blue arrows along the x-axis.

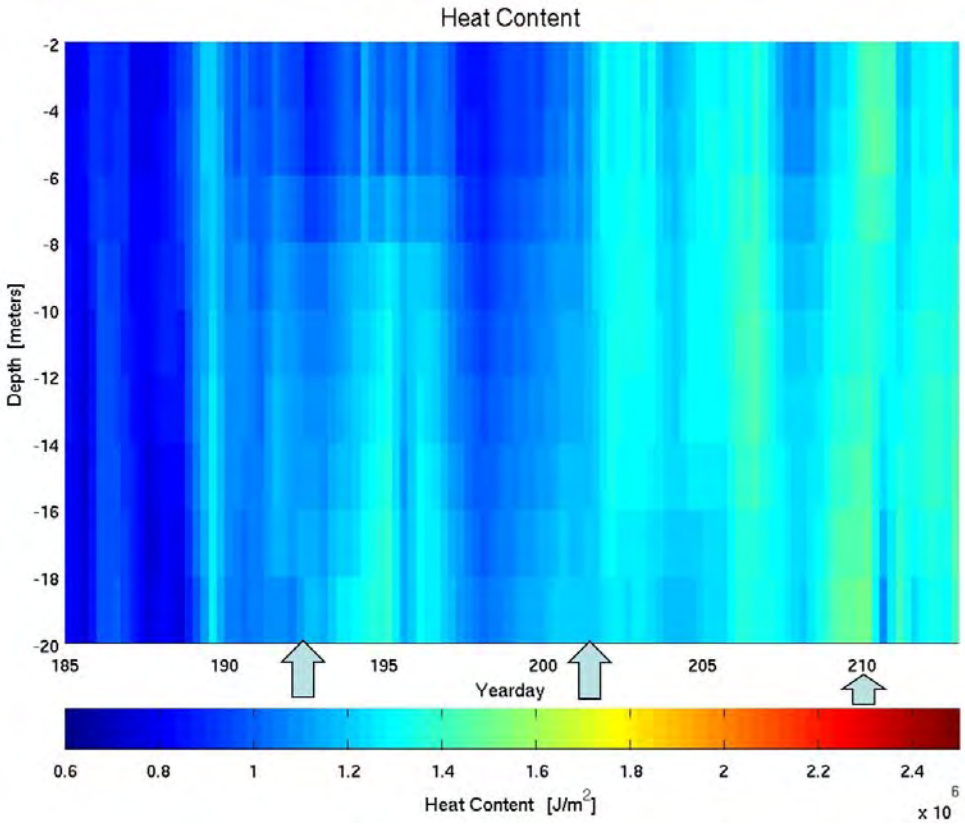

Figure 57. Vertical profile of melt heat content for Group Four. Yeardays corresponding to available satellite imagery are marked by the blue arrows along the x-axis.

IV. DISCUSSION AND CONCLUSION

A primary objective of this study is to understand the processes governing the summer solar heating of the IOBL, the subsequent transport of the stored heat under the ice, and the effect the release of the heat has on the basal melting of ice. As discussed in Chapter III, there appears to be a relationship between open water features seen in satellite imagery and noticeable fluctuations in heat content of the IOBL. Here the relationship between solar heat stored in the IOBL and the vertical heat fluxes to the ice in the Beaufort Sea will be examined. A comparison with the results from the Transpolar Drift data set (Group Four) will also be presented.

Although the model and calculations for heat content in the IOBL assume a stationary water mass, we know that the IOBL is constantly in motion, driven primarily by shearing of the water column by the wind-forced ice motion, and to a lesser extent, by larger scale geostrophic flows. The 'u' and 'v' measured velocity components of the under-ice current measured by the ice-supported instruments were used to calculate the mean current velocity relative to the ice using Equation (10).

$$Velocity_{current} = \sqrt{u^2 + v^2} \tag{10}$$

From Schmidt (2012), it is established that the wind-induced movement of the ice floes can generate enough shear-induced turbulence to induce turbulent mixing of the IOBL. If there is significant heat stored in the IOBL (as reflected in the heat content time series calculated in Chapter III), this increase in turbulent mixing levels will result in increased vertical heat fluxes from the ocean to the ice by mixing up stored heat from the IOBL to the ice base. Heat flux is calculated using Equation (2) and the eddy correlation technique described in Chapter I.

For each of the image groups, the time series of open water fraction, departure from freezing, surface mixed layer melt heat content, current velocity, and heat flux have been plotted on similar scales (Figures 58 to 61). This set of data is referred to as the 'heat transfer time series'.

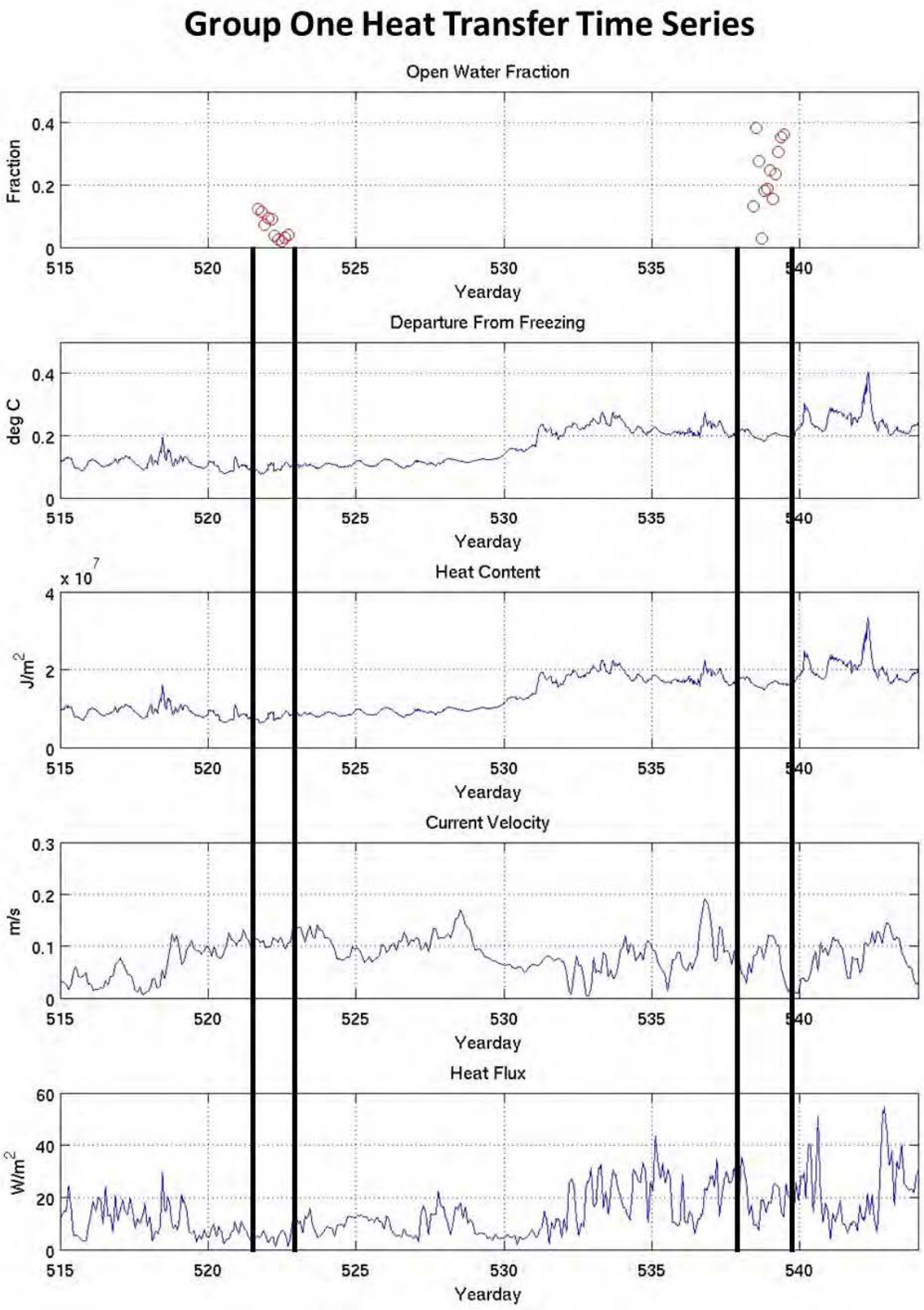

Figure 58. Heat transfer time series for Image Group One.

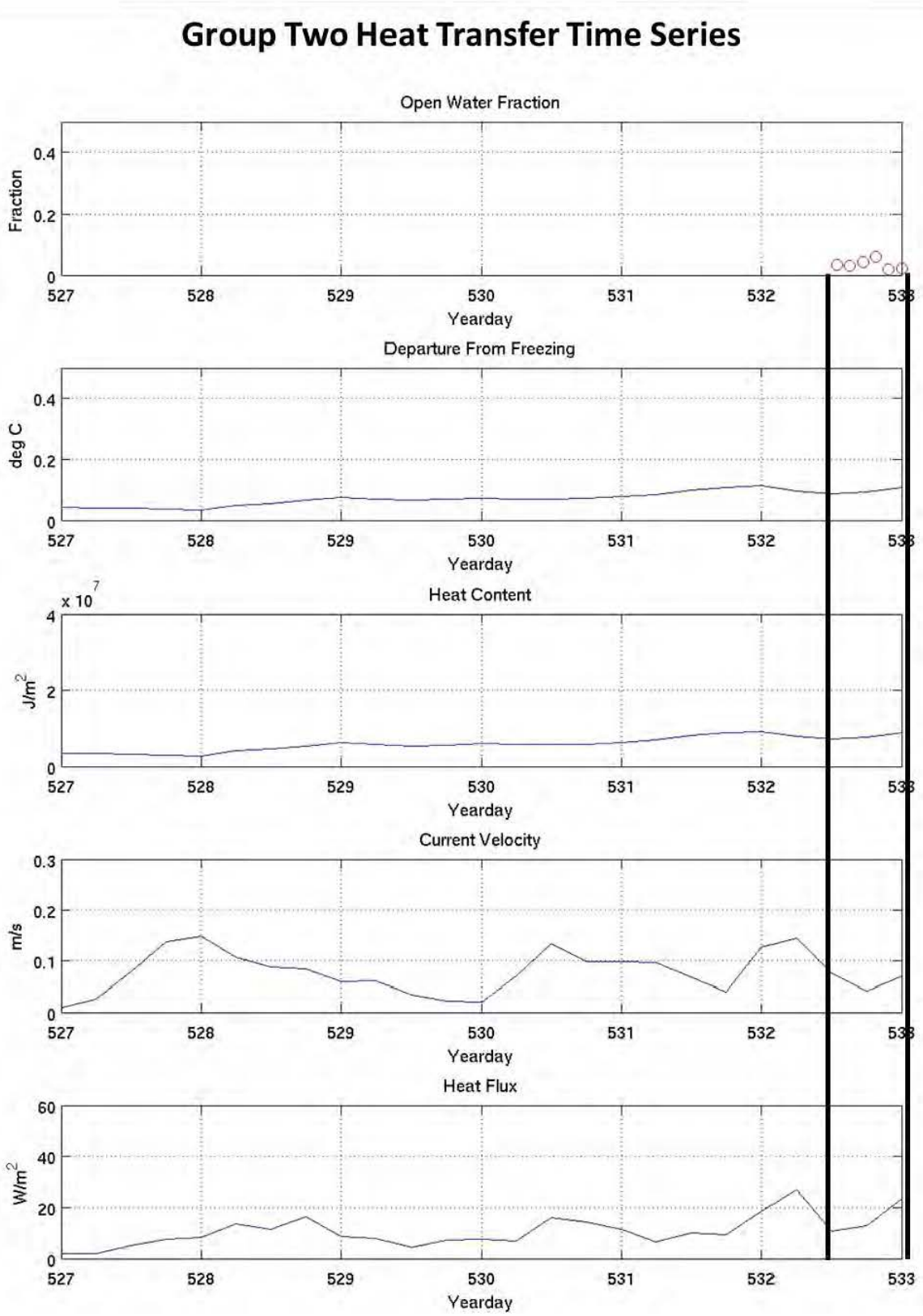

Figure 59. Heat transfer time series for Image Group Two.

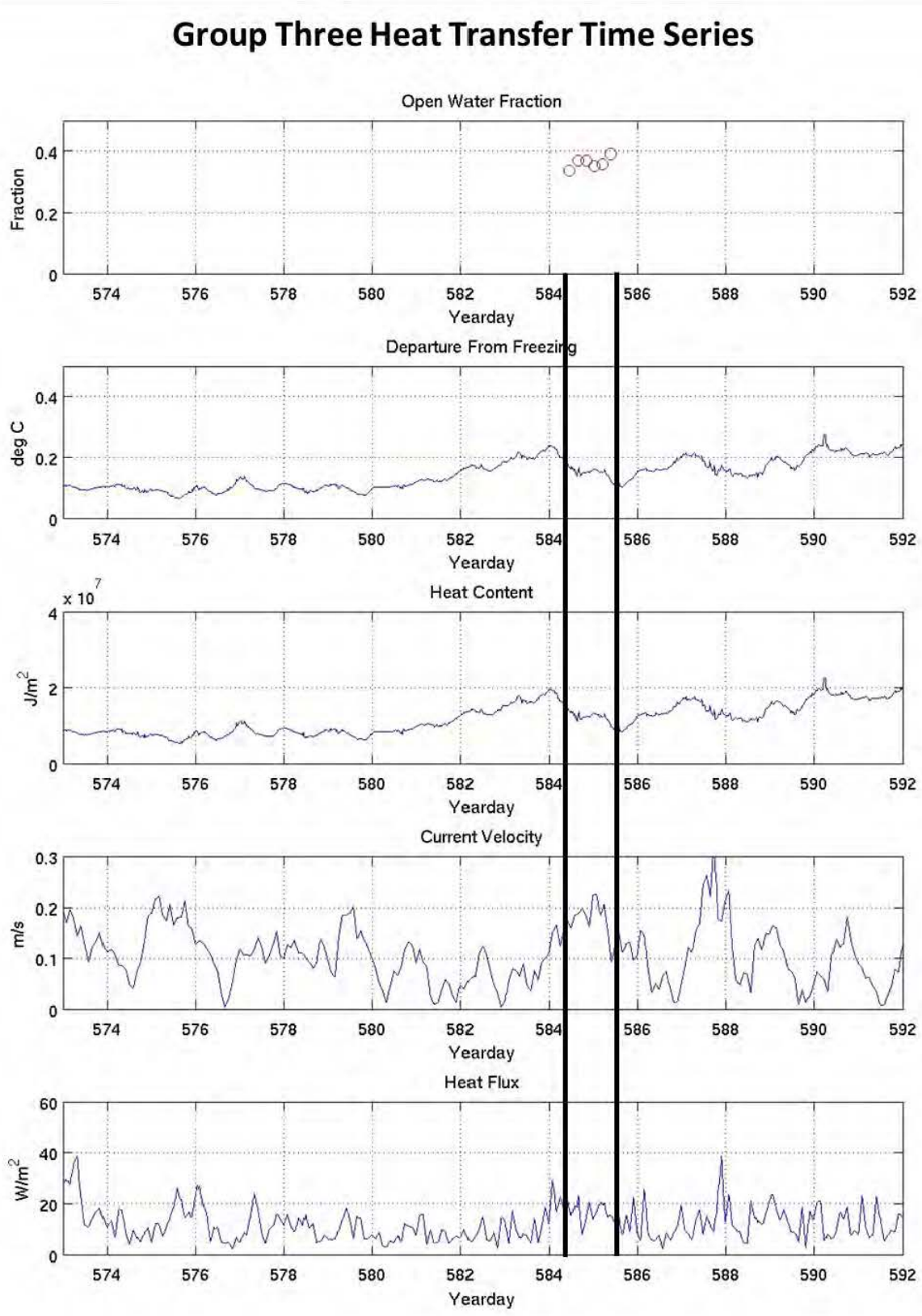

Figure 60. Heat transfer time series for Image Group Three.

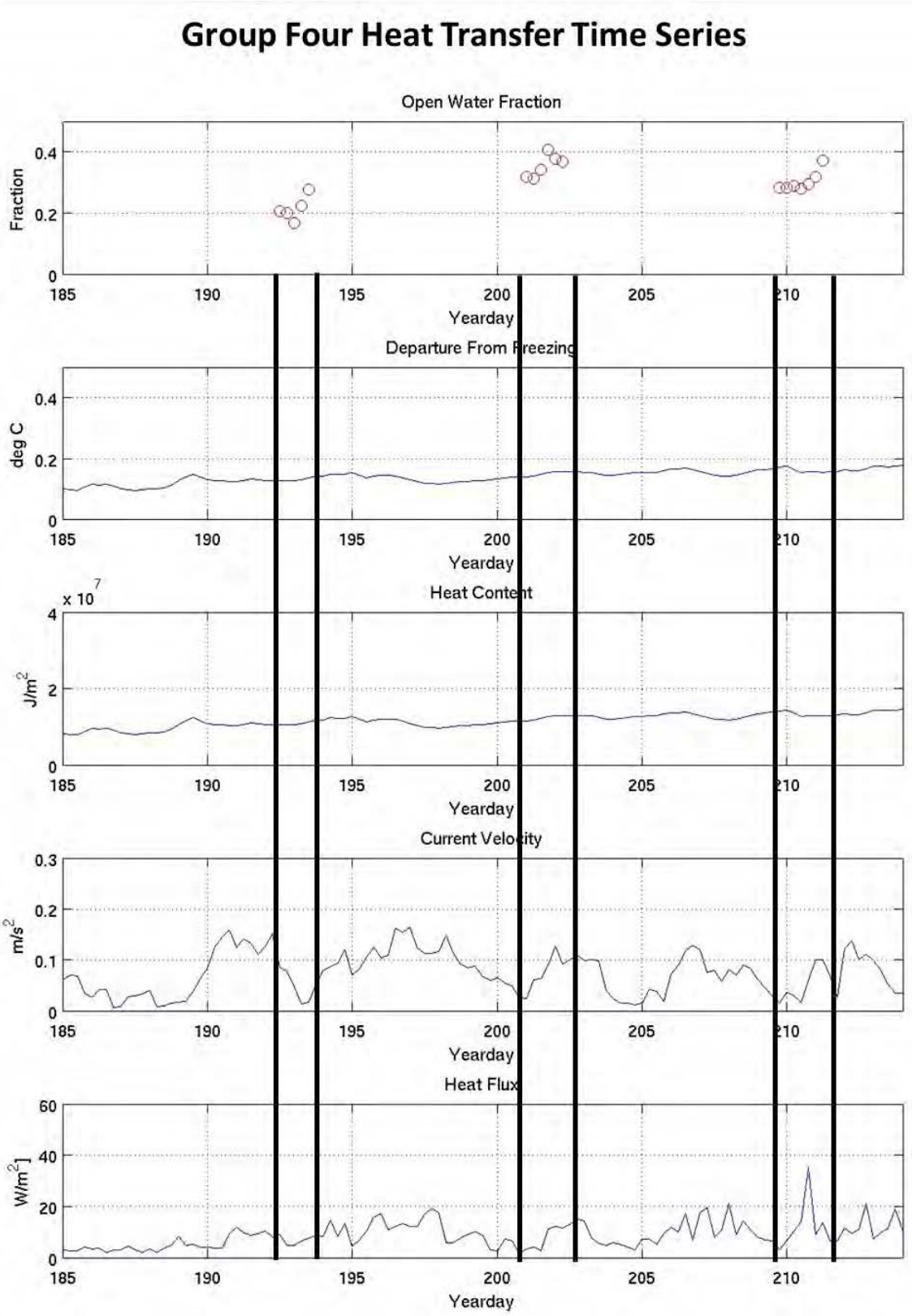

Figure 61. Heat transfer time series for Image Group Four.

A. OPEN WATER FRACTION EFFECTS

The amount of heat transmitted into the IOBL by incoming solar radiation is directly determined by the open water fraction for a given region, and the presence or absence of cloud cover which modulates the amount of shortwave insolation at the surface. The effects of the changes in open water fraction are first seen by increased departure from freezing values in the upper IOBL. In a region where the open water fraction is large, this greater surface open water area, (open ocean or deep meltponds) provides a direct path to absorb incoming solar radiation into the upper ocean. The increased amount of incoming solar radiation will heat the IOBL, increasing the in-situ temperature. This increase in in-situ temperature increases the in-situ freezing point (determined primarily by the in-situ salinity), thereby increasing the surface mixed layer melt heat content of the IOBL. The opposite holds true as well if the open water fraction is low, most of the solar radiation will be reflected and not absorbed. With no mechanism to increase the in-situ temperature the departure from freezing and melt heat content will remain small.

The effect of open water fraction is most evident in Group One (Figure 58). During the Image One time interval, the open water fraction is low, resulting in a low departure from freezing and consequently, low melt heat content. 15 days later in the same time series, we see a significant increase in the open water fraction. The departure from freezing values over the Image Two time interval increase, and consequently so the does the melt heat content. This trend is repeated in Group Two (Figure 59). This image captured a compact ice pack with little available open water. Given the image is from mid-June, we can assume that the ice pack had similar characteristics in the preceding days. Since the majority of the incoming solar radiation is reflected back into the atmosphere, the departure from freezing and heat content are low across the time series.

B. SURFACE MIXED LAYER MELT HEAT CONTENT EFFECTS

Heat stored in the IOBL as a result of increased solar radiation through open ocean and deep meltponds has direct effects on the surface ice conditions. Observations indicate that heat stored in the IOBL pre-conditions the upper water column and increases

the available heat to induce basal ice and lateral ice melt, which in turn contributes to decreased floe strength and vulnerability to breakup at the edges (i.e., increases in open water fraction). From the Group One heart transfer time series (Figure 58), the melt heat content is low during the Image One time interval as previously discussed. Between yearday 530 and yearday 535, it is likely an ice divergence event which caused an increase in the melt heat content of the IOBL. As the melt heat content of the IOBL increases, we see an increase in the open water fraction in Image Two 15 days later. In Group Three (Figure 60), we see the same relationship. The melt heat content early in the time series is low; however, at approximately yearday 581, we see the start of significantly increasing heat content. During yearday 584, when Image 26 was captured, we see a high open water fraction.

C. HEAT FLUX EFFECTS

While increases in the open water fraction result in increases in IOBL stored melt heat content, this heat is not readily available to melt the ice cover without a turbulent forcing mechanism. To aid in heat flux analysis, current velocity data is used. Additionally, measurements of vertical heat flux measured by the AOFBs below the ice are considered. Due to the noise variability in eddy-correlation estimates of $w'T'$, heat flux is estimated using Equation (11) (McPhee 2008) and is then used to calculate the heat flux from Equation (2).

$$\langle w'T' \rangle = C_H * u_* * T_{DFF} \tag{11}$$

Where the Stanton number, C_H , is approximated at .0057; the friction velocity, u_*, is measured directly by the AOFB, and the departure from freezing, T_{DFF} , is calculated using Equation (8) (McPhee 2008).

The role of heat flux in transferring heat stored in the IOBL is evident in the Group One results (Figure 58). In the early part of the time series, the melt heat content is low, as previously established. During the Image One interval, the current velocity is nearly uniform and relatively large. However, since the melt heat content is low, the corresponding heat flux is also small. In the other image (Image Two) from this group,

the current velocity is approximately the same magnitude, but we observe a larger heat flux value. This is the result of the higher heat content of the IOBL from the increased open water fraction as discussed previously.

The melt heat content of the IOBL is one component in controlling the heat made available from the IOBL to the ice. Higher current velocities result in a greater amount of shear-induced turbulence (Schmidt 2012), but the results show that higher velocities do not necessarily yield higher heat flux values; melt heat content must be sufficient to support this as well. In Group One (Figure 58), we see a high velocity at yearday 528, yet the low heat content at the same time results in a low heat flux. Consequently, later in the same group (approximately yearday 537), we see a similar value of current velocity. Here, even though the increase in melt heat content is small, it is enough to generate a much larger corresponding heat flux value. It is likely that the increase in heat flux values across the latter half of the Group One time series are the result of shear-induced turbulence in the IOBL and are bringing heat to the ice where it induces basal melt. This would further suggest the strong link between the removal of heat in the form of basal melting allowing for thinner ice and open water to create conditions favorable for the absorption and storage of heat in the IOBL.

D. CONCLUSION

Both the reduction in summer sea ice extent and the ice regime thickness changes from MYI to FYI have significant thermodynamic effects for the IOBL. In this initial approach to connect open water fraction to IOBL heat content via one-meter pixel size high-resolution declassified satellite imagery, all available imagery for the Beaufort Sea was collected from the USGS GFL website. The bounding coordinates of the image and the solar angle information was extracted to determine in which images the AOFBs were located at the image capture time. Those “hit” images were further processed by robust pixel processing methods to quantify the total open water fraction, open ocean fraction, and meltpond fraction. AOFB and ITP data providing ocean property and associated heat flux measurements were matched to the image intervals to be used in further analysis.

This study shows that high-resolution visible satellite images can be successfully exploited in the studies of ocean-ice interaction physics. Shaw et al. (2014, unpublished manuscript) notes that while large scale imagery (greater than 500km x 500km resolution) can be used to observe aggregate scale evolution of the MIZ, these images lack the resolution to observe small-scale ice-ocean interactions governing MIZ processes. Additionally, passive microwave sensing, a common tool for studying open water fraction, has a large footprint (12.5km x 12.5km), which is still too large to observe detailed boundary layer and ocean-ice interaction. They suggest that by targeting pre-determined areas within the MIZ, the evolution of the compact ice pack at the end of winter through its breakup into small floes can be traced across the spring and summer season. When coupled with in-situ measurements (such as from AOFBs), it would offer insight in the dynamic processes that are otherwise unattainable (Shaw et al. 2014, unpublished manuscript). This proposal was validated by the approach used in this study.

Results from this study indicate that there is a relationship between the open water fraction identified in high-resolution satellite imagery and the observed integrated surface mixed layer melt heat content of the IOBL. As more open water becomes available through ice divergence and the deepening of meltponds, more solar radiation is allowed to enter the IOBL. In six of seven images processed and analyzed, increases in the open water fraction of the ice were followed by increases in heat content. Observations also show a potential relationship between open water fraction increasing as a result of increased heat content. This suggests the presence of a positive feedback loop: as the open water fraction increases, more solar radiation enters the IOBL, thereby increasing the heat content; this heat is then vertically mixed and induces basal and lateral melt, weakening the ice, increasing the open water fraction and closing the (enhanced) loop.

Observations from this study show the importance of the magnitude of heat content in regulating the heat flux values. Even in instances of high current velocities where high heat flux values could be expected, if the heat content is low, the heat flux is low as well. At the same time, if the heat content is high, heat flux values follow closely with the magnitude of the current velocity, i.e. faster current velocity equals higher heat flux.

1. Recommendations for Future Work

The methodology used in this study represents the initial attempt to connect open water fraction to upper ocean heat content using high-resolution satellite imagery. To further develop this approach, there are some improvements to be made. First, the library of available satellite imagery needs to be expanded. Out of 1100 images, only 29 contained the AOFB within the image at the image capture time, not taking into account the effects of cloud cover. By incorporating the use of high-resolution synthetic aperture radar (SAR) imagery, which is not affected by cloud cover, additional AOFB and ITP observations can be used to develop the robustness of this method. For this study, we have assumed that the solar radiation is constant over the image interval, due to a lack of solar information. The use of solar sensors, which have been incorporated on the most recent AOFB deployments (as seen in Figure 62), can be used to determine the effect of variations in solar intensity into the open water fraction-heat content problem. Additionally, the use of current information measured by the AOFB should be brought in to remove the +/- 12 hour static ocean assumption at the time the image was captured. This would allow for the lateral motion of the water in the IOBL under the ice to be taken into account. Finally, the use of Inertial Measurement Units (IMUs) can be used to determine the effects of increased wave action contributing to the breakup of ice, potentially resulting in enhanced break up and increases in solar radiation input into the upper water column.

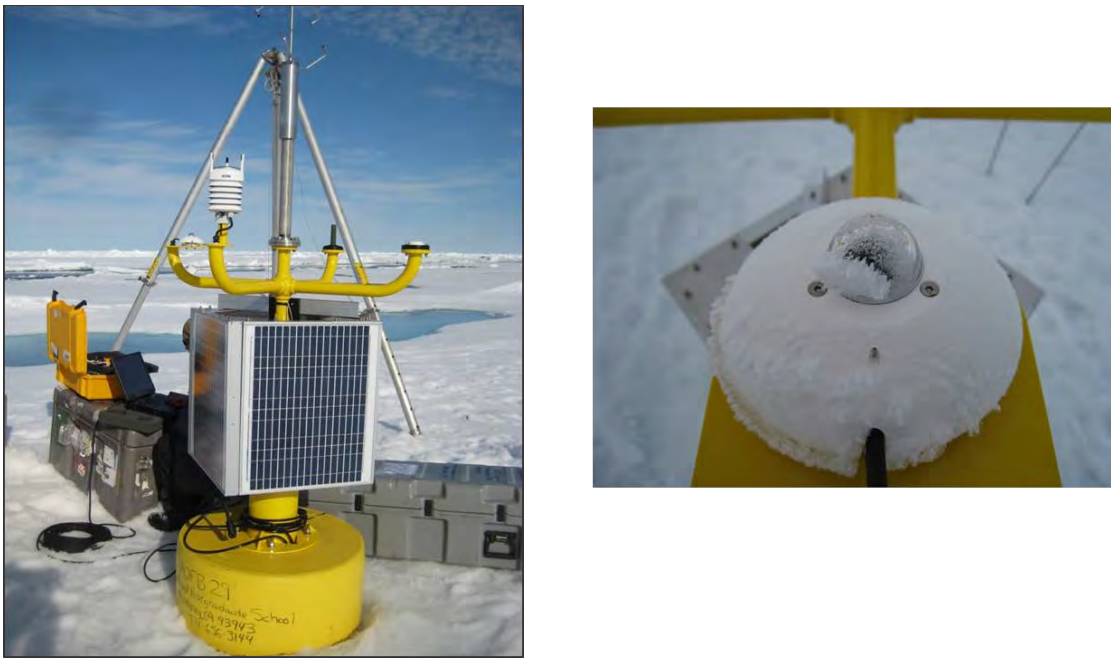

Figure 62. Photographs of AOFB 29 deployed in the Arctic in August 2014. Left Image: small domed solar sensor on the left-most arm of the meteorology tree collects shortwave (visible) surface solar intensity time series which can be used to understand the effects of varying solar intensity in the open water fraction/heat content relationship. Right Image: close up image of the solar sensor used to collect shortwave solar information (images courtesy Mr. Jim Stockel 2014).

2. Future Navy Impacts

The efforts of this study directly contribute to naval operations in the high latitudes. As stated in the U.S. Navy Arctic Roadmap (2014), collecting in-situ observations is crucial in understanding the complex dynamics of the MIZ. This study validates the initial approach of using high-resolution satellite imagery as a tool to both quantify the local open fraction of the ice pack and use it to examine the relationship to upper ocean heat content. According to the Congressional Research Report *Changes in the Arctic: Background and Issues for Congress* (2014), over $38 million is requested by the NSF for Arctic research, with the majority of the funding going towards logistic support associated with deploying and maintaining in-situ sensors. In an era where fiscal responsibility is paramount, this study represents initial efforts to identify cost-effective

methods at improving the scientific community's knowledge of the atmosphere-ice-ocean system in the poles.

Aside from collecting observations to be fed into high-resolution, regional-coupled models, the work in this thesis provides a current positive impact for the Navy as well. MIZEX 2014, part of the ONR MIZ DIR, is a current project at the time of this study. The satellite processing code developed for this study has already been incorporated into the project to provide the satellite imagery operators near real-time feedback on the accuracy of their targeting techniques. Since images capturing small ice-supported sensor clusters are an integral part of developing this approach to model heat content in the IOBL, it is imperative that the operators receive feedback on their accuracy so any adjustments can be made during the critical image capture intervals.

There are future implications of this processing approach as well. As the naval research continues to focus on the development of distributed undersea networks, such as Seaweb (Rice, 2005), this capability can be integrated in submarine and Unmanned Undersea Vehicle (UUV) operations. Satellite imagery can be received either from shore-based operators or downloaded from naval access portals directly. A fully developed image processing function integrated into the platforms computer suite would then be able to identify areas of open water or thin ice favoring breaching operations to be navigated towards.

LIST OF REFERENCES

ASL, cited 2014: ASL History. [Available online at http://www.csp.navy.mil/asl/History.htm.]

Col, S. M., 2010: Fine-scale variability in temperature, salinity, and pH in the upper-ocean and the effects on acoustic transmission loss in the Western Arctic Ocean. M.S. thesis, Dept. of Engineering Acoustics, Naval Postgraduate School, 89 pp.

Congressional Research Service, 2014: Changes in the Arctic: Background and Issues for Congress. CRS Report R41153, 4 August, 124 pp.

Davies, J., cited 2014: ICEX 2014 Images. [Available online at http://www.dvidshub.net/image/1194977/icex-2014#.U8bwgfldV8E.]

DiMaggio, D., 2014: The role and variability of ocean heat content in the Arctic Ocean: 1948–2009. Dept. of Oceanography, Naval Postgraduate School, 89 pp.

Hudson, S. R., M. A. Granskog, A. Sundfjord, A. Randelhoff, A. H. Renner, and D.V. Divine, 2013: Energy budget of first-year Arctic sea ice in advanced stages of melt. *Geophysical Research Letters*, **40**, doi: 10.1002/grl.50517.

IPCC, 2013: Summary for policy makers. Climate Change 2013: The Physical Science Basis. , Stocker, T.F., D. Qin, G.K. Plattner, M. Tignor, S.K. Allen, J. Boschung, A. Nauels, Y. Xia, V. Bex, and P.M. Midgley, Eds., Cambridge University Press, 3-29.

Krishfield, R. A., A. Proshutinsky, K. Tateyama, W. J. Williams, E. C. Carmack, F. A. McLaughlin, and M. -L. Timmermans, 2014: Deterioration of perennial sea ice in the Beaufort Gyre from 2003 to 2012 and its impact on the oceanic freshwater cycle. *Journal of Geophysical Research: Oceans*, **119** (2), 1271-1305, doi: 10.1002/2013JC008999.

Krishfield, R., K. Doherty, D. Frye, T. Hammar, J. Kemp, D. Peters, A. Proshutinsky, J. Toole, and K. von der Heydt, 2006: Design and operation of Automated Ice-Tethered Profilers for real-time seawater observations in the polar oceans. WHOI Tech. Rep. 2006-11, 75 pp. [Available online at http://www.whoi.edu/fileserver.do?id=32723&pt=2&p=38033.]

Lee, C.M., S. Cole, M. Doble, L. Freitag, P. Hwang, S. Jayne, M. Jeffries, R. Krishfield, T. Maksym, W. Maslowski, B. Owens, P. Posey, L. Rainville, A. Roberts, B. Shaw, T. Stanton, J. Thomson, M.-L. Timmermans, J. Toole, P. Wadhams, J. Wilkinson, and Z. Zhang, 2012. *Marginal Ice Zone (MIZ) Program: Science and experiment plan*, Technical Report APL-UW 1201. Applied Physics Laboratory, University of Washington, Seattle, 48 pp.

Maslanik, J., J. Stroeve, C. Fowler, and W. Emery, 2011: Distribution and trends in Arctic sea ice age through spring 2011. *Geophysical Research Letters*, **38**, doi: 10.1029/2011GL047735.

McPhee, M. G., 2008: *Air-Ice-Ocean Interaction: Turbulent Ocean Boundary Layer Exchange Processes*. Springer, 215 pp.

McPhee, M. G., 1983. Greenland Sea ice/ocean margin. *EOS*, **64**, 82-83 [Available online at http://onlinelibrary.wiley.com/doi/10.1029/EO064i009p00082/pdf.]

Metzger, J., cited 2014: ICEX 2014: Navigating the world's last frontier. [Available online at http://www.navy.mil/submit/display.asp?story_id=79929.]

NOAA Climate, cited 2014: 2012 Arctic Report Card. [Available online at https://www.climate.gov/news-features/features/2012-arctic-report-card.]

NSIDC, cited 2014: Arctic sea ice extent settles at record seasonal minimum. [Available online at http://nsidc.org/arcticseaicenews/2012/09/arctic-sea-ice-extent-settles-at-record-seasonal-minimum/.]

NPS AOFB, cited 2014: NPS Autonomous Ocean Flux Buoy Program. [Available online at http://www.oc.nps.edu/~stanton/fluxbuoy/.]

Pettersen, T., 2013: Fifty percent increase on Northern Sea Route. *Barents Observer*, 03 December. [Available online at http://barentsobserver.com/en/arctic/2013/12/fifty-percent-increase-northern-sea-route-03-12.]

Perovich, D.K., and C. Polashenski, 2012: Albedo evolution of seasonal Arctic sea ice. *Geophysical Research Letters*, **39**, L08501, doi: 10.1029/2012GL051432.

Perovich, D. K., 2005: On the aggregate-scale partitioning of solar radiation in Arctic sea ice during the Surface Heat Budget of the Arctic Ocean (SHEBA) field experiment. *Journal of Geophysical Research*, **110**, C03002, doi: 10.1029/2004JC002512.

Rice, J., 2005: Seaweb acoustic communication and navigation networks. *Proc. the International Conference "Underwater Acoustic Measurements: Technologies & Results,"* Heraklion, Crete, Greece.

Reuters, cited 2014: German ships successfully make "Arctic Passage." 12 September. [Available online at http://www.reuters.com/article/2009/09/12/us-climate-shipping-arctic-idUSTRE58B01K20090912.]

Schmidt, B. K., 2012: Observations of hydraulic roughness and form drag in the wake of a deep ice keep in the Arctic Ocean. M.S. thesis, Dept. of Physical Oceanography, Naval Postgraduate School, 81 pp.

Shaw, W.J., T.P. Stanton, M.G. McPhee, J.H. Morison, and D.G. Martinson, 2009: Role of the upper ocean in the energy budget of Arctic sea ice during SHEBA. *Journal of Geophysical Research*, **114**, C06012, doi: 10.1029/2008JC004991.

Smith, W. O., and J. M. Grebmeier, 1995: *Arctic Oceanography: Marginal Ice Zones and Continental Shelves.* Coastal and Estuarine Studies, 49, American Geophysical Union, 287.

Stockel, Jim. Images taken during MIZEX 2014.

Stanton, T., W. J. Shaw, and J. K. Hutchings, 2012: Observational study of relationships between incoming radiation, open water fraction, and ocean-to-ice heat flux in the Transpolar Drift: 2002 – 2010. *Journal of Geophysical Research*, **117**, doi: 10.1029/2011JC007871.

Stroeve, J.C., V. Kattsov, A. Barrett, M. Serreze, T. Pavlova, M. Holland, and W.N. Meier, 2012: Trends in Arctic sea ice extent from CMIP5, CMIP3 and observations. *Geophysical Research Letters*, **39 (16)** , L16502, doi: 10.1002/grl.v39.16

Stroeve, J.C., M.C. Serreze, M.M. Holland, J.E. Kay, J. Malanik, and A.P. Barrett, 2011: The Arctic's rapidly shrinking sea ice cover: a research synthesis. *Climatic Change (2012)*, **110**, 1005-1027, doi: 10.1007/s10584-011-0101-1.

Suh, G.Y., 2011: Shear and stability at the base of the mixed layer in the Arctic Ocean: The role of inertial motions. M.S. thesis, Dept. Of Meteorology and Physical Oceanography, Naval Postgraduate School, 79 pp.

University of Alaska, Fairbanks, cited 2014: Characterization of the Circulation on the Continental Shelf Areas of the Northern Chukchi and Western Beaufort Seas. [Available online at http://dm.sfos.uaf.edu/chukchi-beaufort/background.php.]

USGS, cited 2014: Visible Satellite Images. [Available online at http://gfl.usgs.gov/gallery_main.shtml?current=4.]

USGS (FAQ), cited 2014. [Available online at http://gfl.usgs.gov/#earthSys.]

U.S. Naval Observatory, 2005: *Multiyear Interactive Computer Almanac*. Richmond: Willmann-Bell, 118 pp.

U.S. Navy, cited 2014: U.S. Navy Arctic Roadmap 2014 – 2030, 42. [Available online at http://www.navy.mil/docs/USN_arctic_roadmap.pdf.]

WHOI ITP, cited 2014: Ice-Tethered Profiler. [Available online at http://www.whoi.edu/page.do?pid=20756.]

THIS PAGE INTENTIONALLY LEFT BLANK

INITIAL DISTRIBUTION LIST

1. Defense Technical Information Center
   Ft. Belvoir, Virginia

2. Dudley Knox Library
   Naval Postgraduate School
   Monterey, California